UCSF

UC San Francisco Electronic Theses and Dissertations

Title

Kinetics of Single-Strand RNA Virus Entry and Transmission

Permalink

https://escholarship.org/uc/item/763583b7

Author

Catching, Benjamin Adam

Publication Date

2022

Peer reviewed|Thesis/dissertation

Kinetics of Single-Strand RNA Virus Entry and Transmission

by
Benjamin Adam Catching

DISSERTATION
Submitted in partial satisfaction of the requirements for degree of
DOCTOR OF PHILOSOPHY

in

Biophysics

in the

GRADUATE DIVISION
of the
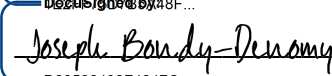UNIVERSITY OF CALIFORNIA, SAN FRANCISCO

Approved:

_____ Raul Andino
B96EC8E0C8FA430...   Chair

_____ John Gross

_____ ADAM FROST

_____ Joseph Bondy-Denomy
D23522498F4247C...

_____
                                                                          Committee Members

Dedication and Acknowledgments

No man is an island, and this work would not be possible without the many individuals that have supported and guided me along this process. First, I would acknowledge my advisor Raul Andino, who took in a biophysics student and made him a virologist. I would not be where I am today without Raul, who pushed me, guided me, brainstormed with me, and presented me with opportunities and collaborations that allowed me to diversify and broaden my skill sets. Raul's knowledge of enteroviruses, along with his endless curiosity, have opened the eyes of this former physicist to the world of virology.

Raul's lab is gave numerous opportunities to learn from several mentors who each imparted both skill sets and mindsets on how to be a scientist. Ming Te Yeh, taught me everything I needed to know when it came to creating a virus from plasmid to cell culture to animal experiments. If it were not for his detailed protocols, personal plasmids, and years of expertise, I would have never made my first viral mutant or titered the numerous culture experiments in this thesis. He is truly an exemplary virologist who I am glad to share a number of publications with. I would also acknowledge Patrick Dolan, who encouraged me to grow my computational and data analysis side, to really think about the question I was pursuing instead of trying to just get an impressive data set. The long coffee-break conversations we had guided how I think about setting up a project and how to use my time wisely. And here is to Orly Laufman, who saved me with a pointed refinement to my cell culture skills in the face of persistent contamination and who taught me the how to be a microscopist when necessary. As well, thank you Ranen Aviner, whose mentoring on Western Blots and

Biophysics program, helped me through picking a research lab to conduct my Ph.D in, and gave me unbiased console during my degree progression.

The research I did at UCSF would not be possible if I had never built the skills and experience the be accepted at such a great university, and there were numerous teachers along the way. First and foremost is Rob Phillips of Caltech, who gave me a 'journey to Mars' through a job as a Course Assistant at the Physiology course at the Marine Biological Laboratory and as a Laboratory Technician in his lab at Caltech. While I worked as hard as I was able in these positions, they were both still a learning experience, where I truly went from zero experience in biology and learned as much as I could under Rob's teachings. I would like to thank also my mentors and professors at my alma mater, California State University, Chico. To Chris Gaffney, thank you for the first research opportunity to publish my work and with it the chance to demonstrate my abilities as a scientist. To Eric Ayars, who taught me how to be a thorough experimentalist and how to work with groups of scientists (no trivial task!). To Louis Buchholtz, who taught me how to be a thorough theorist and to appreciate the classics. To David Kagan, whose Quantum Mechanics course not only was the best taught class I ever had and taught me how to teach, but is the one who introduced my parents to each other and without whom I may not be here. And to Anna Petrova-Mayer, whose teachings of lasers and optics began my adventure in university-level science.

I would like to also thank my family, truly the ones who got me here. To Sarah, thank you for hanging on my shoulders and teaching me how to have boundless energy. To Katie, thank you for showing me how to question authority and to stick up for myself. To Mom, thank you teaching me that being organized, put together, and on top of things is no small task but has infinite rewards. To Dad, thank you for being a model family-man and scientist who can balance it all.

To my wife, Leah, this thesis is dedicated to you. I would not have gotten through these past five years and more without you. You are my rock and I am yours, I have enjoyed every moment of our adventure in San Francisco. This thesis is dedicated to you and your

unwavering support through my time as a graduate student.

Kinetics of Single-Strand RNA Virus Entry and Transmission

Benjamin Adam Catching

Abstract

Pandemic Potential Pathogens remain an ever-present scourge upon the human species. Epidemics and pandemics have ranged from nuances to having the power to shut the entire world down. Molecular biology and epidemiology have the synergistic power to understand, prepare for, and combat this horseman of the apocalypse. In this thesis, I share my humble part in this perpetual struggle, examining the potential mutations of note and their phenotypic properties of enteroviruses as well as modeling the spread and transmission of coronavirus. Using the powers invested through the mathematical lens of physical biology, I endeavored to add to both basic virology and epidemiology against these dangerous pathogens.

Contents

List of Figures

List of Tables

Chapter 1

Introduction

1.1   background

Positive sense, single-strand RNA (+ssRNA) viruses are some of the fastest evolving (RNA virus evolution rates) and have caused a significant number of outbreaks in the past couple of decades[63, 55, 197, 107, 167, 64, 82]. Different Genus of +ssRNA viruses are both endemic (enteroviruses) and zoonotic (coronaviruses). While reservoirs of either enteroviruses or coronaviruses viral pathogens may differ, both types of viruses share their novelty, so to say that outbreaks and pandemics are caused by previously unidentified strains or mutants of an already identified species[53, 206]. Growing isolates of these pathogens in a controlled laboratory setting allows for perturbations to the viral life cycle, including elevating temperature, enhancing innate immune response, or the competition induced by defective interfering particles, to name a few[204, 174, 11, 188]. The viral response to these perturbations, whether it distribution and composition of possible mutations or sub-phenotypes of viral replication, gives insight to methods to predict and combat future viral outbreaks.
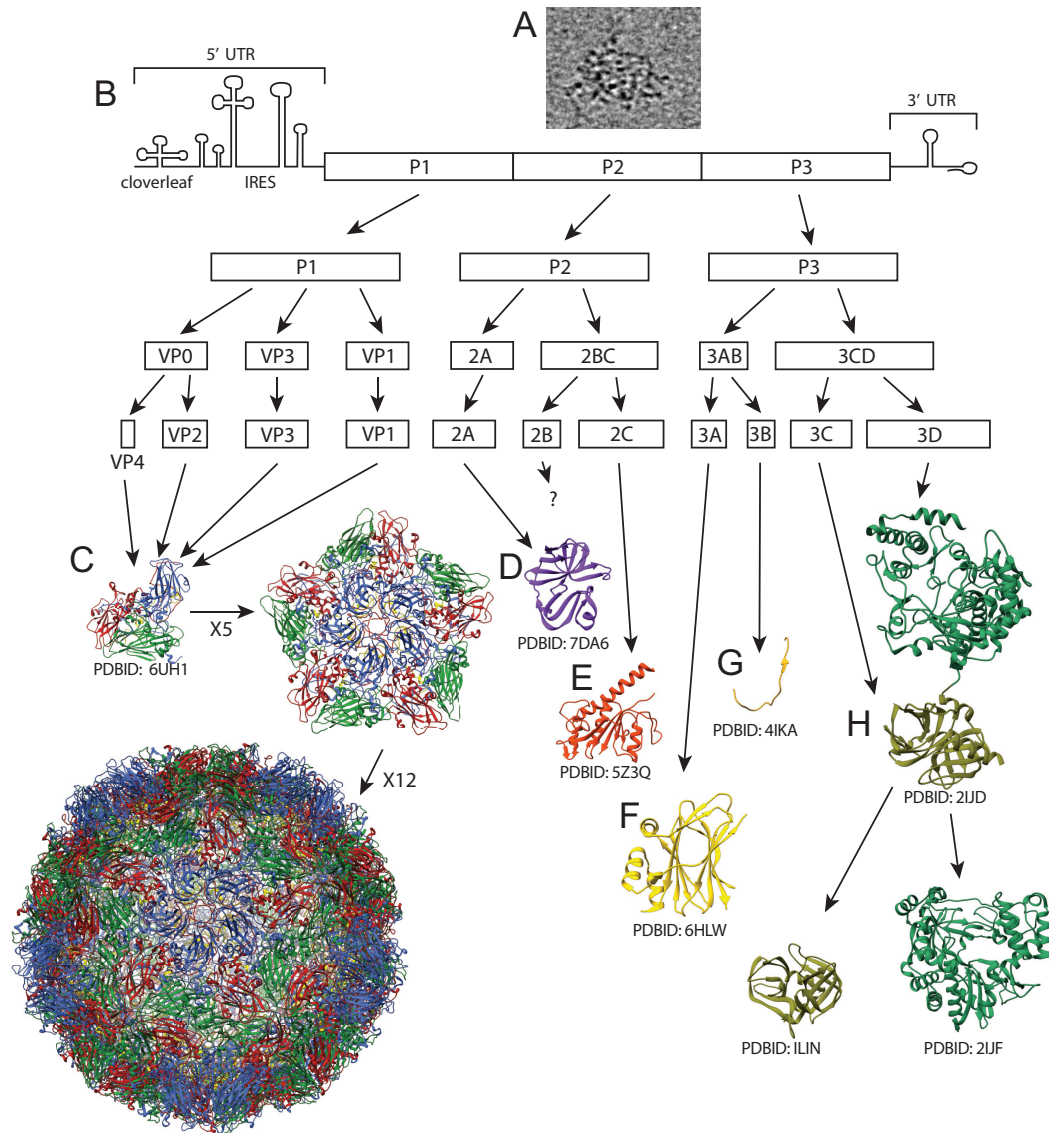
Figure 1.1: Genome and Proteins of Enteroviruses

1.2 Enteroviruses

1.2.1 Genome and Replicaton

Enteroviruses are 7.5 kb +ssRNA viruses whose genome (**Figure 1.1.A**) is encoded by a 740 nucleotide 5' untranslated region (UTR), a region encoding four structural proteins called P1, followed by 7 protein-encoding regions called P2 and P3 and terminated by a short 3' UTR with a poly-adenylated tail[117, 94] (**Figure 1.1.B**). The P1 protein folds with the

assistance of the cellular molecular chaperone heat-shock protein 90[181]. This folded protein is then cleaved by the 2A protease, encoded in the P2 region, into 3 subsequent proteins; VP0, VP3, and VP1[187] (**Figure 1.1.C**). Each of these cleaved proteins shares a similar β-barrel tertiary structure with several exposed loops[142, 118, 79]. These three proteins remain in an oligomerized state, binding with other trimers around the condensed+ssRNA genome to form the immature capsid[75]. Through unknown mechanisms, VP0 is cleaved into proteins VP2 and VP4 after the formation of the immature capsid to form the mature capsid, a viral particle with infectious ability[214]. Viral protein P2 encodes three proteins, 2A, 2B, and 2C, which are responsible for viral replication. The viral poly-protein is self-cleaved by 2A, cleaving at the P1-P2 and P2-P3 interface (**Figure 1.1.D**). 2A has also been been implicated in the inhibition of cellular factors, including eIF4G, causing the shut-off of cap-dependent translation[110, 99]. The cleaved P2 protein produces both 2A and 2BC, which is further processed into 2B and 2C. The structure of enterovirus 2B is not known, but it is a small, hydrophobic protein that binds to the endoplasmic reticulum and Golgi, remodeling the cell to facilitate the assembly of viral capsid[12, 126]. Viral protein 2C binds to cell membranes and remodels the cell for viral replication, while also playing a role in genome replication by binding to the 3ÚTR[56] (**Figure 1.1.E**). The viral protein P3 encodes 4 sub-proteins that also aid in viral replication. 3AB is first cleaved from 3CD, where 3AB is used anchoring the viral genome to viral replication vesicles[182, 196]. 3A also mediates the cellular innate immune response by inhibiting the major-histocompatibility complex (MHC), which presents viral epitopes for immune cells[48] (**Figure 1.1.F**). The protein 3B is a small, viral protein that covalently links to the 5ÚTR, possible to aid with packaging the +ssRNA genome into viral capsids (**Figure 1.1.G**). 3CD is thought to process all events after P1/P2/P3 cleavage (**Figure 1.1.H**), as well as 3C has been shown to shutdown host-cell translation[125, 200, 23]. The genome is replicated during each replication cycle by the 3D RNA-depdendent RNA-polymerase (RdRp), where the genome serves as a template for the error-prone replication[189, 66] (**Figure 1.1.H**).

1.2.2 Enterovirus capsid and entry

The entire genome is encapsulated by a non-enveloped capsid, an 30 nanometer (nm) diameter icosahedral protein shell that performs multiple functions, chief of which include protecting the genome from the harsh extra-cellular environment and to bind and release the genome into susceptible mammalian cells[146, 209, 210, 104]. Susceptibility is defined as a cell's ability to bind and traffic the capsid, allowing for the internalization of the capsid and genome that allow for subsequent rounds of viral replication. Species of enterovirus have different cell-surface attachment factors and receptors that allow for cell entry via different mechanisms[18] (**Figure 1.2.A**). Entry is primarily mediated by clatherin mediated endocytosis[87, 89] (**Figure 1.2.B**). Due to pathogenesis of enteroviruses mainly occurs along the oral-fecal route, most enteroviruses are low pH tolerant[219]. However, this excludes Rhinoviruses and EV-D68, both of which transmit along the respiratory route and do not encounter low-pH environments[119]. The presence or absence of this environment-dependent capsid stability indicates that pathogenesis may be linked to what environments the virus traverses. During trafficking of the viral capsid, cell factors, modifications to the endosome, and state transition of the viral capsid, releases the +ssRNA genome into the cellular cytoplasm (**Figure 1.2.C**). The viral genome is first used as a template for translating the 11 viral proteins (VP1, VP2, VP3, VP4, 2A, 2B, 2C, 3A, 3B, 3C, 3D) (**Figure 1.2.D**). Of these proteins the RdRp 3D (**Figure 1.2.E**) is used for transcribing the negative-sense, single-strand RNA (-ssRNA) genome (**Figure 1.2.F**). This -ssRNA genome is then used as a template for replicating the +ssRNA genome (**Figure1.2.G**). This process exponentially increases the number of viral copies, which both are subsequently used for viral protein replication and virus capsid production (**Figure 1.2.H**).

1.2.3 Enterovirus Pathogensis

Understanding the composition and distributions of these mutations due to specific environmental perturbations yields both mechanistic understanding of how viral proteins interact
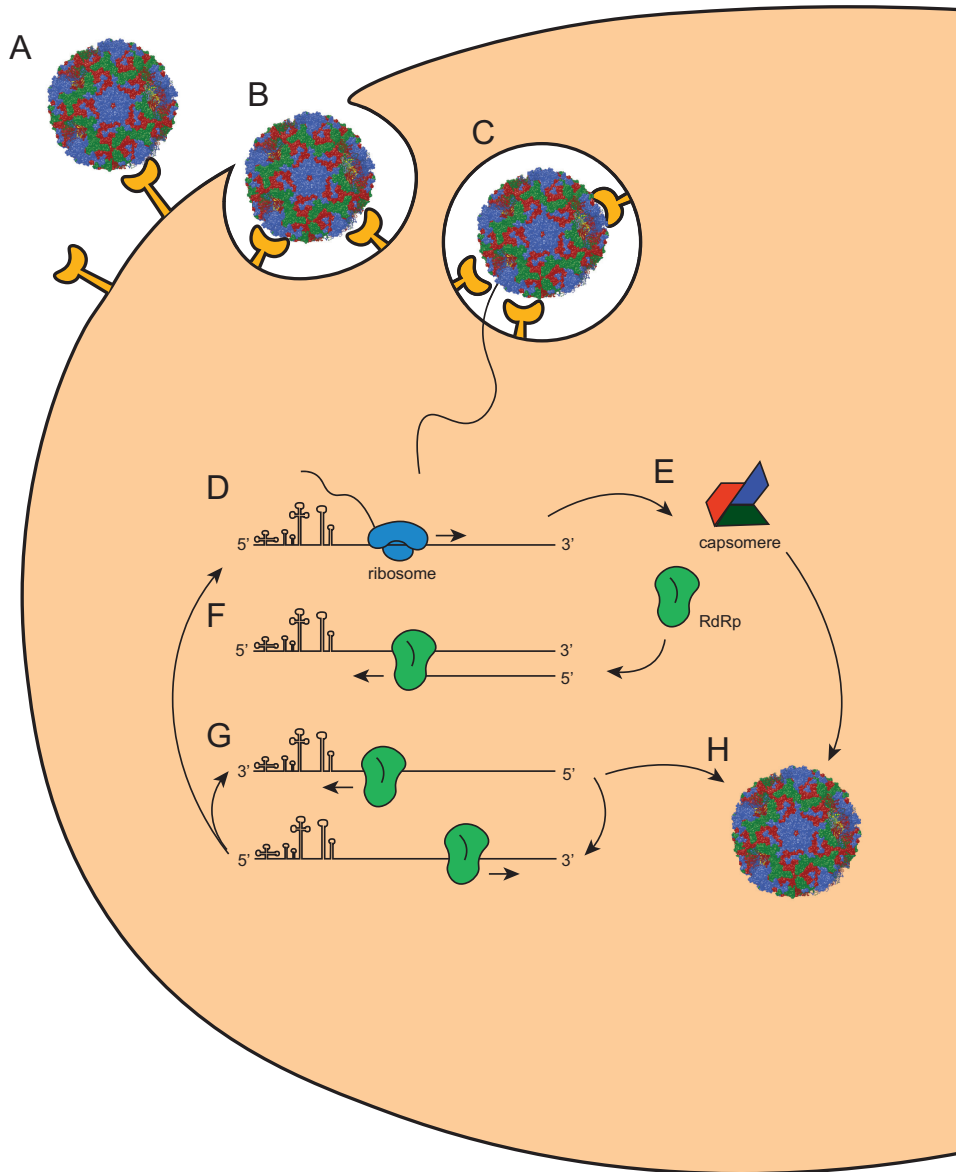
Figure 1.2: Cell Entry and Replication of Enteroviruses

with cellular processes but also on functional sites of viral proteins. Even more, the function of a specific viral protein is often found to be context specific, whether that is dependent on surrounding protein expression or which phase of pathogenesis a viral infection is at[95, 96]. These microscopic levels of interaction can manifest at macroscopic levels, such as the number of infectious particles produced[108] which results in the transmissibility of viral infection. Despite not having a zoonotic carrier to reside in between outbreaks, enteroviruses are still pervasive in the modern world[205, 133]. The prototypical enterovirus, Poliovirus (PV), has continued to reside in the human population despite an international, vigorous, eradication campaign[130]. There remains no cure for Poliomyelitis and the most effective tool for eradication has been the PV vaccine. Indeed, one of the most recognizable stories in science is the development, disbursement, and efficacy of the inactivated PV vaccine (IPV)[154, 185] and the oral attenuated PV vaccine (OPV)[151, 44]. Recently, a new OPV has been developed, in part by the lab of Raul Andino[212, 106] and shown to be more effective than the original OPV[30, 194] by the introduction of the safety elements that reduce the ability to recombine with other enteroviruses, increased fidelity in replication, and a stabilized 5' UTR. This work motivates experiments on cell-culture based evolution of enteroviruses that are encapsulated in this thesis. By perturbing controlled replication of EV-A71, PV, and CVB3 by physical, innate immune system, or genomic methods, the rapid mutation rate of the RNA-dependent RNA-polymerase samples possible mutations that not only confer adaptations to these phenotypically relevant conditions but are allowed in the context of maximizing replication fitness.

1.2.4   Coronavirus Transmission

The 2019 coronavirus pandemic surprised the world by revealing the inadequacy of our pandemic preparedness[177, 49]. Thankfully, both the rapid development of an effective vaccine and waning severity of disease has lessened the still incredible impact of the pandemic. The epidemiological study of the SARS-CoV-2's spread is still ongoing, but many aspects have

already been gleaned[72]. Transmission of COVID-19 is respiratory, with infectious particles being shed from nasal and oral cavities[192]. While studies have attempted to measure transmission between animals in controlled settings, intricacies of intra-human disease transmission is difficult to capture[35, 162, 52]. Using encapsulating measurements, such as the reproductive number of how many people are infected by a single infected individual, R_o, the spread of disease can be modeled[218, 76, 34]. Modeling disease spread always comes with a level of abstraction and the usefulness of a model depends on which parameters are wished to be predicted and what aspects of a model can be ignored. With a highly transmissible virus like SARS-CoV-2, especially evolving variants, the rate at which a susceptible population is infected is of concern[201, 26, 78, 141].

1.2.5 Section and Chapter Description

This thesis encompasses both enterovirus molecular biology and coronavirus transmission. Section I examines the mechanisms enterovirus capsids use to enter susceptible cells. This is done by looking at prototypical enterovirus species A, B, and C; Enterovirus A71, Coxsackievirus B3, and Poliovirus type 1. In chapter two I go over the central aspect of my thesis, adaptation to elevated temperatures in EV-A71 and the trade-offs in host cell entry caused by increases in thermostability. This chapter also demonstrates a previously unknown genome uncoating intermediate and the implications the order of uncoating state intermediates. Chapter three deals with an unexpected mutation in Coxsackie B3 protein VP4 as a response to the innate immune response. Ties from this mutation to capsid stability and cell entry are also examined. Chapter four looks at how Poliovirus type 1 thermostability mutants that have been previously published cause decreases in cell entry efficiency, as well as how the length of the packaged +ssRNA genome impacts thermo- and osmo-stability. Section II tackles both mitigating the spread of SARS-CoV-2 and viral shedding kinetics in human hosts. Opposed to the almost-atomic level mechanisms of section I, this section deals with the macroscopic transmission of viral disease. Chapter five represents the first-author

paper I published which deals with using simulations to model how preventative measures, such as face masks, slow the spread of disease. This paper is far from the original scope of this thesis, but represent answering the call to communicate critical science for general public understanding during a global pandemic. Finally, chapter six comprises my work alongside a multi-lab effort to quantify the shedding of SARS-CoV-2, and do vaccines reduce how much viral load is diminished?

Part I

Enterovirus Evolution

Chapter 2

Metastable Tradeoff of Thermostability and Cell Entry in Enterovirus A71

2.1 Abstract

This work was done in collaboration with Ming Te Yeh of the Andino lab, Sara Capponi at IBM, and Simone Bianco, now at Altos labs. The majority of this work was performed by myself, including the cell culture, thermodynamics, molecular biology, structural determination, and data analysis. Animal experiments were performed by Ming Te Yeh after discussion with myself and extracted tissues were titered by myself. Molecular dynamics simulations were performed by Sara Capponi after discussions of proper setups and variables to test, analysis was performed by both myself and Sara. Raul and Simone assisted with guiding the direction of the central questions and which experiments best probed the system in question. This work will be submitted to a journal at the time of writing.

2.2 Introduction

All proteins must form either one or a continuum of native, folded, states to perform their required functions [50]. The low-energy 'ground-state' of a protein is required to go through numerous semi-folded states. Molecular chaperones and specific cellular conditions aid in the proper folding pathway [159] [65] while chemical, physical, and cellular environments can also catalyze the reversion to partially-unfolded or even fully denatured states. Proteins also have dynamic ranges of where they are natively folded and/or functional, which may include large temperature ranges [57]. This is amplified for viral proteins, whose infectious particles must exist in potentially harsh extra-cellular conditions or in host cells which have tuned many systems for detection and degradation of foreign viral proteins [83]. The viral capsid traverses a potentially large space of environments, from assembly within the cell [111] [25] to the highly variable extracellular environment to the cell entry pathway [166] [219]. The viral capsid must protect the genome from these environments while releasing the genome only under precise conditions that can yield a viral infection.

Viruses are hypothesized to have existed since the origin of cellular life and have evolved multiple mechanisms to enter cells [51], [22], [202]. This tuned ability to enter susceptible cells balances the phenotype of selectively releasing the genome under specific conditions while maintaining particle integrity in sometimes harsh extra-cellular environments. This trade-off of phenotypes are two of the many roles the viral particles must perform, including cell attachment, antigenic evasion, and particle assembly. Genome loss/ejection is effectively an irreversible process, therefore viable viral particles must have a large energetic barriers that must be catalyzed by specific environmental conditions or combinations of conditions including pH change, receptor, membrane proximity, or heat [180], [199], [160]. Passaging of Poliovirus under elevated extracellular temperatures has resulted in accumulation of mutations, although several mutations were required to induce thermostability [10] These specific conditions also require specific moieties on the outer protein surface.

Understanding the biophysical properties of the balance between these phenotypes has

numerous potential benefits. Many bioengineering attempts have been made to imitate the various viral endocytosis processes to deliver pharmaceuticals such as small-molecule compounds [81] or mRNA vaccines [42]. However, these approaches tend to have non-ideal limitations with regards to not being tuned to release their cargo easily [186] from overstabilization or are too thermo- or acid- labile to be intact through physiological environments like the GI tract. As well, empty capsid (EC) systems are an active area of research, where the viral capsid minus the genome can be used as a type of vaccine [10]. Barriers to development of these systems are again due to stabilizing the viral capsid to survive outside the cell.

Enteroviruses are a genus of Picornaviruses comprised of single-strand RNA (ssRNA) genomes encapsulated by a icosahedral capsid 30 nm in diameters [94]. While the 20th century was marked by the near-eradication of Poliovirus, the prototypical Enterovirus, outbreaks of non-poliovirus enteroviruses (NPEV) have become a major concern. Even more concerning has been species of Enteroviruses that have gone from benign to pathogenic, such Enterovirus A71 (EV-A71) in the late 1990s [128], [215]. The error-prone replication of Enteroviruses, including EV-A71, allow for a large space of possible mutations to be sampled after each replication cycle [65]. As a viral population replicates a multitude of adaptive paths are explored that end up maximizing the swarm's fitness relative to the experimental conditions. This quasi-species differentiates over time from the original population and results in mutations that are local maximums of the fitness landscape [159]. Strong selection pressures result in steeper fitness landscapes and can influence which mutations become fixed in the population.

In this study we look at the adaptation of EV-A71 to increased extra-cellular temperature, the biophysical and structural mechanism of the thermostable mutant, and the attenuation of the cell entry phenotype by increased thermostability.
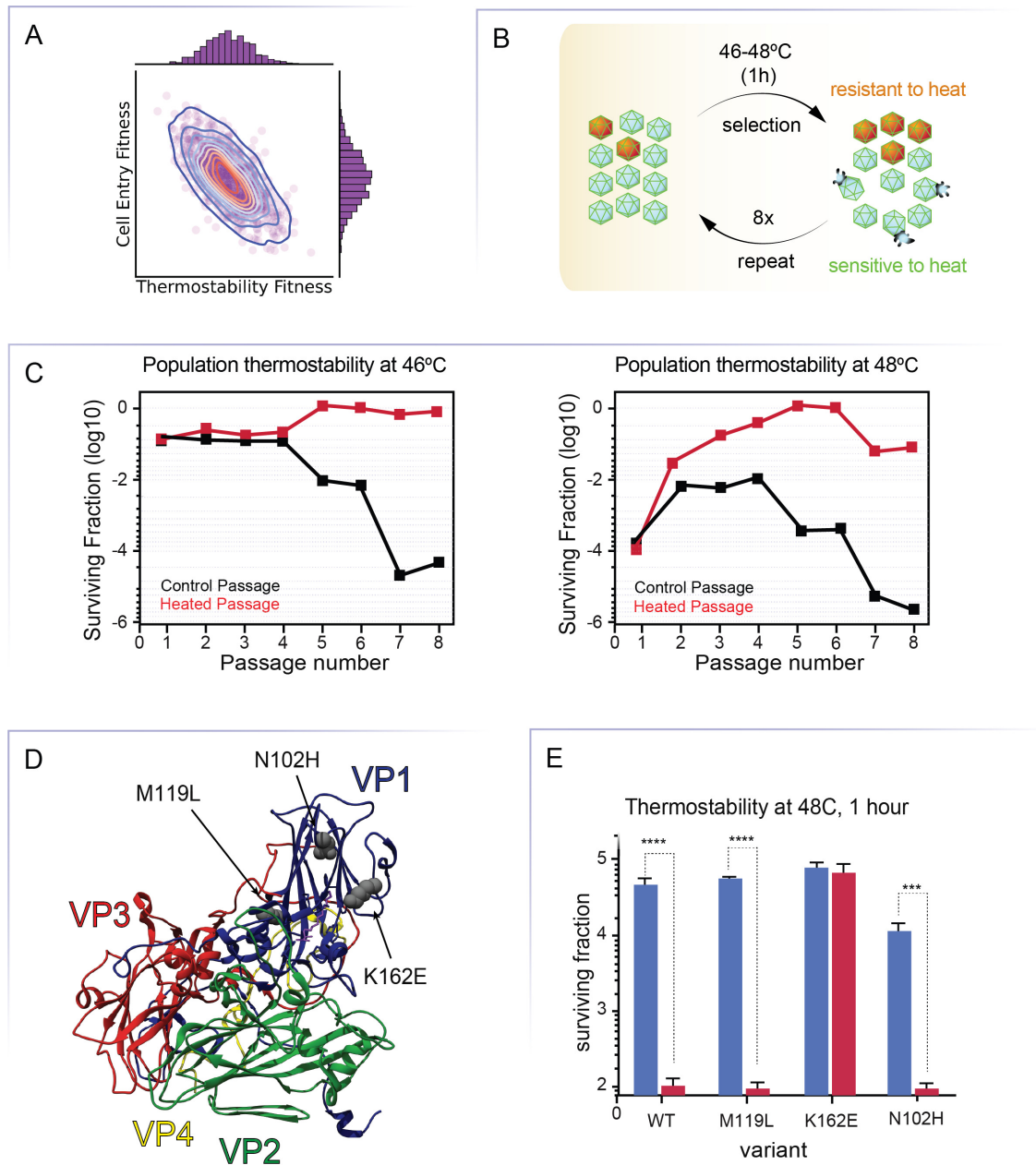
Figure 2.1: Selecting for a Thermostable Capsid Mutation
A)Simulated distribution of fitness values between thermostability and cell entry for capsid mutations **B)** Genetic screen experimental conditions for adaptation to elevated temperature **C)** Reduction in passaged viral population relative to input population, testing at 46°C for 1 hour **D)** Reduction in passaged viral population relative to input population, testing at 48°C for 1 hour **E)** Locations of possible thermostability mutations on EV-A71 capsomere, subunits VP1 (blue), VP2 (green), VP3 (red), and VP4 (yellow) are shown **F)** Validation of K162E providing thermostability under elevated temperature

2.3 Results

2.3.1 Selecting for thermostable variants

Enteroviruses have been studied in the past under specific conditions in cell culture [9], [65] and found that the distribution of fitness values for a given selection pressure to follow a quasi-Gaussian distribution centered at a relative fitness value of 0.6 and sizeable fraction of deleterious mutations at 0. It is then hypothesized that for the distribution of possible mutations relating to thermostability also follow a Gaussian distribution. We simulated this distribution of mutational fitness values by drawing a Gaussian distribution of 3000 fitness values centered at 0.6 for the thermostability phenotype then calculated the inverse relationship with cell entry (**Figure 2.1.A**). Additional random white noise was added to the cell entry fitness values, to replicate a non-perfect one-to-one correlation, was also added. We posit that mutations that increase thermostability correlate with a decrease in fitness of cell entry. This trade-off of capsid stability and speed at which the capsid can release the genome into the cell puts these two main functions of the same protein at odds.

We then optimized selection conditions for extra-cellular heating between passages, 46^oC for 1 hour for the first 4 passages and then by $48°C$ for 1 hours for passages 5-8 (**Figure 2.1.B**). Using this selection condition 10^6 $TCID_{50}$ units of WT EV-A71 were either heated or kept on ice before being titered and used to infect Human rhabdomyosarcoma (RD) cells at a multiplicity of infection (MOI) of 0.01. MOI was kept low to reduce the effects of mutational hitchhiking and genome recombination. Viral supernatant was titered before and after heating at 46^oC and 48^oC. Only the aliquots of the heated passages were exposed to 46^oC for 1 hour before another replication cycle while the control passages were passaged using un-heated aliquots.

Titering samples of both the control (black) and heated (red) passages before and after heating at 46^oC for 1 hour revealed a gradual adaptation to elevated temperatures (**Figure 2.1.C**). Both control and heated passages maintained similar levels of thermostability for

the first 4 passages, both populations being inactivated to similar fractions of the initial population. Only at passage 5, the same passage where adaptation to cell culture briefly decreased (SM Figure **1A**), does the heated passages appear to become more thermostable. Samples of passages were also heated at 48°C for 1 hour to measure adaptation to higher temperatures (**Figure 2.1.D**). Of note, while the heated passages were not exposed to the temperature of 48°C, adaptation to this elevated temperature does appear beginning as early as the second passage. Surprisingly, while adaptation to 46°C does not appear during the first 4 passages, adaptation to heating at 48°C does appear in the same time frame. This could be due to low-frequency mutations in initial passages increasing in frequency and becoming more pronounced when the elevated temperature reduces the population to an even smaller fraction.

Sequencing was performed on ssRNA genomes extracted from passages via RT-PCR and Sanger Sequencing. The capsid region was examined for sequence similarity to the WT strain. At passage 6 of the heated samples three mutations were isolated, methionine to leucine at position 119 in VP1 (M119L), lysine to glutamic acid at position 162 in VP1 (K162E), and asparagine to histadine at position 102 in VP1 (N102H) (**Figure 2.1.D**). Mutations were cloned back into the original plasmid encoding the WT genome, transcribed into RNA, and transfected into cells to produce viable virus. Each mutant virus was titered, exposed to 48°C heating for 1 hour, and titered again (**Figure 2.1.E**). Only K162E was found to increase thermostability. The other two mutations were also discovered in the control passages without the presence of K162E, also indicating similar trajectories of cell culture adaptation.

2.3.2 Inactivation is caused by a slowed transition to A-particle

The loss of infectivity by heating is caused by the conversion of the mature capsid to the so-called 'altered particle' or A-particle [219] [160] [198]. This state change is accompanied by the loss of the N-termini of capsid proteins VP1 and VP4. As well, it has been observed that

16
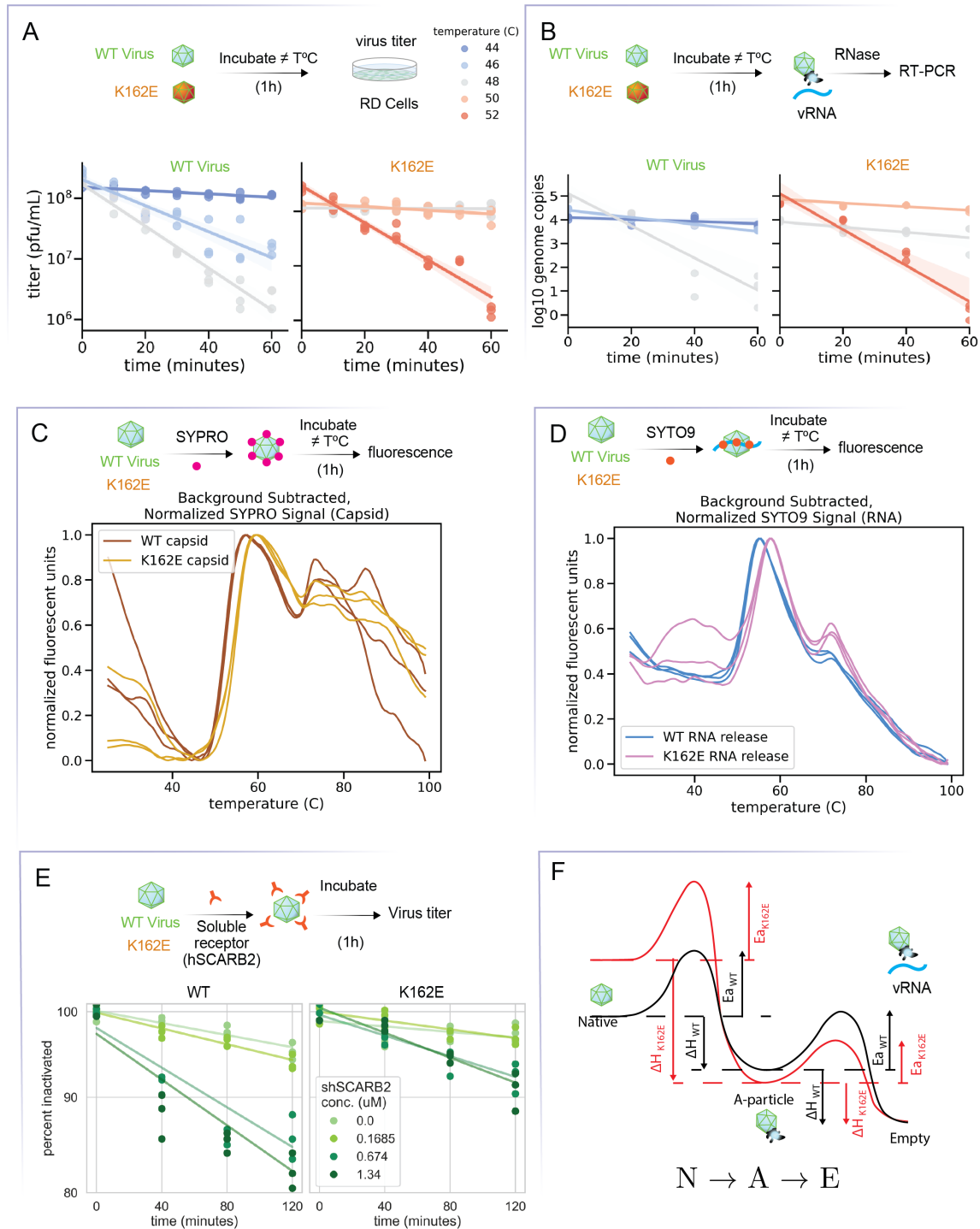
Figure 2.2: Thermostability is a Two-Step Process

A) Inactivation of infectivity in WT and K162E kinetics, measured by $TCID_{50}$ **B)** Kinetics of genome release in WT and K162E, measured by RT-qPCR **C)** Thermostability assay measuring for transition to the A-particle state **D)** Thermostability assay detecting the release of the ssRNA genome over a wide range of temperatures **E)** Inactivation of infectivity by lowered by pH and titration of shSCARB2 protein **F)** Energy landscape of inactivation and genome release

the capsid proteins (purple) expand outward and the ssRNA genome (green) becomes reorganized. This conversion is also produced by incubation with receptor SCARB2, indicating that the A-particle is formed during SCARB2-mediated endocytosis, the main mechanism of cell entry [211].

Table 2.1: Rate of Inactivation, k_f $(10^{-5}s^{-1})$

Strain	44°C	46°C	48°C	50°C	52°C
WT	10.7±0.145	82.3±2.62	132±2.14		
K1162E			0.87±0.13	12.6±0.45	129±2.49

Table 2.2: Rate of Genome Release, k_r $(10^{-5}s^{-1})$

Strain	44°C	46°C	48°C	50°C	52°C
WT	7.13±3.29	24.7±1.42	113±17.8		
K1162E			18.4±6.41	12.9±2.12	126±10.6

The mutant K162E and WT viral capsids were purified to examine the biophysical properties of thermostability. By heating purified samples over 1 hour and taking samples every 10 minutes, the rates of inactivation for WT and K162E were determined for different temperatures (**Figure 2.2.A**). Rates of inactivation were shifted 4°C greater for K162E than WT. The same method of elevated temperature exposure to purified WT and K162E particles was used to determine if genome uncoating occurred at similar rates to inactivation by heating (**Figure 2.2.B**). As with inactivation rates, K162E's rate of genome uncoating remained low at 48°C and 50°C, with a sudden increase in rate of genome uncoating at 52°C. This is in contrast to the how the WT particle loss of genomes remained low at 44°C and 46°C but increased suddenly at 48°C. The low rates of inactivation and genome uncoating from heating at 52°C suggests that inactivation is immediately followed by genome loss for K162E; stability caused by the mutation mainly affects the native to A-particle transition but not the process of the genome transversing the capsid. This was confirmed by western blot where samples taken every 10 minutes during heating at the same temperatures as in the inactivation rates (**Supplemental Material Figure 2.2**). Samples were digested with

proteinase K prior to loading samples on the gel, which selectively cleaves only exposed VP4 proteins, another indicator of A-particle formation. Signal loss correlated with virus inactivation curves.

To confirm the increase in inactivation temperature observed in K162E an fluorescent-based assay, Particle Stability Thermal Release Assay (PaSTRy) [195], was performed. Fluorescent signals that report the presence of hydrophobic residues was used to indicate the externalization of the N-termini of VP4 and VP1, reporters of the conversion to the A-particle. K162E was found to have a 2.4°C increase at which the state transition occurred (**Figure 2.2.C**). A second peak in signal was observed around 75°, indicating the temperature where capsids begin to unfold. The release of genomic RNA from the capsid were measured over an increasing range of temperatures (**Figure 2.2.D**). The temperature where half of the genome-associated signal increased from 51.8^{o}C for WT to 54°C for K162E. Both transitions were observed to increase at least 2°C, which confirms the shifts in thermostability caused by K162E measured by inactivation and RT-qPCR.

2.3.3 Receptor-Mediated Conversion

The transition to A-particle has been observed to be catalyzed by the primary receptor for EV-A71, Scavenger Receptor B2 member 2 (SCARB2) [211], [46], [219], [41]. The attachment to the mature capsid followed by the low pH-mediated conversion to the A-particle state, occurring during the cell entry process, can be replicated by a soluble form of the receptor. Purified capsids were incubate with shSCARB2 at 37°C for up to two hours, with measurements of infectivity taken every twenty minutes (**Figure 1.2.E**). The inactivation by the presence of soluble, human SCARB2 (shSCARB2), lowered pH and relatively low temperature of 37°C, was still reduced in K162E. In the absence of shSCARB2, K162E also displayed the reduced inactivation by lowered pH to 5 and 37°C compared to WT. The addition of shSCARB2 at increasing molarity did increase the inactivation rates of both WT and K162E, but rates of inactivation were lower in K162E than WT for the same concentration

of shSCARB2. The lowered inactivation rates in the presence of the primary receptor for EV-A71 point to the reduced ability to enter cells by the increased free energy required to proceed from native to A-particle to empty states.

2.3.4   Thermodynamics of Particle Stability

The rates of inactivation and genome ejection we were able to calculate the enthalpy, entopy, and free energy of the state transitions of both WT and K162E. This was done using the Eyring equation: $k_f = \frac{\kappa k_B T}{h} e^{\Delta S/R} e^{-\Delta H/k_B T}$ Where k_B is Boltzmann's constant, h is Planck's constant, and R is the ideal gas constant. κ is the transmission coefficient, set as 1, as the loss of VP4 for inactivation and genome uncoating are irreversible processes. As expected, the enthalpy of transition from N $\rightarrow$ A for the thermostable mutant was more than twice that of the WT, which can be distributed between the 60 capsomere copies at around a 2 kcal/mol stabilization per capsomere (**Table 2**). As well, the free energy for the N $\rightarrow$ A transition also nearly doubles, resulting in a $\Delta\Delta G^{N \rightarrow A}$ of 235 kcal/mol. This increase in energy for the N $\rightarrow$ A are a significant but expected barrier for state transition due to the genetic screen selected for mutants that resisted heat-accelerated inactivation. Surprisingly, the enthalpy of A $\rightarrow$ E transition for K162E was 39.9 kcal/mol less than WT. Despite the thermostabilizing mutation protecting viral particles from inactivation, the same mutant reduced the barrier for genome release. This was mirrored in the decrease in free energy for genome ejection, with a 38.8 kcal/mol reduction in barrier free energy. This indicates that the mutation that was selected reduced the barrier for genome ejection to compensate for the increased barrier for priming by entering the A-particle state. There still was a net increase in the $\Delta\Delta H$ for the complete N $\rightarrow$ E process, where both empty complete state transitions end with the empty particle. As this ground state is structurally, phenotypically, and energetically identical between WT and K162E, we set the this state as the anchor point on the energy landscape (Figure 2.2.F). This means that the net increase in enthalpy between N→A and A→E state transitions sets the native, N, state at a higher starting point. The amplitude of

both WT and K162E free energy barriers and net enthalpy provide context for the K162E mutation inhibiting inactivation but a slight compensatory mechanism of increased genome release.

Table 2.3: Thermodynamics of Uncoating

Reaction	ΔH	ΔS	ΔE
WT N $\rightarrow$ A	126.4 $\frac{kcal}{mol}$	-48.5 $\frac{cal}{mol \cdot K}$	141.4 $\frac{kcal}{mol}$
WT A $\rightarrow$ E	139.0 $\frac{kcal}{mol}$	-48.9 $\frac{cal}{mol \cdot K}$	154.2 $\frac{kcal}{mol}$
K162E N $\rightarrow$ A	259.1 $\frac{kcal}{mol}$	-58.2 $\frac{cal}{mol \cdot K}$	276.4 $\frac{kcal}{mol}$
K162E A $\rightarrow$ E	99.1 $\frac{kcal}{mol}$	-52.6 $\frac{cal}{mol \cdot K}$	115.4 $\frac{kcal}{mol}$

2.3.5 Near-atomic resolution differences between WT and K162E capsomers

To understand what structural changes occur at the two main states of the uncoating process by the mutation of K162E were examined by cryogenic electron microscopy (CryoEM). Particles were purified from cell culture and were screened by negative stain electron microscopy prior to vitrification on thin-carbon quantifoil grids. Using the software package Relion [155] reconstructions of each particle were performed using icosahedral symmetry. One imaging set each was performed for the native WT, native K162E, heated WT, and heated K162E samples. A-particles and empty particles were differentiated from the heated datasets by class averaging and picking averages that either did (A-particle) or did not (empty) have coulomb density at the center of the particle. Atomic models were built through Phenix for the native and A-particle states of WT and K162E using the asymmetric unit of the entire capsid. Statistics for data collection are disclosed in the Supplementary Material Figure 3.

The native state of the WT particle was refined to a resolution of 3.3 angstroms using the gold-standard fourier shell correlation cutoff of 0.143 (**Figure 2.3.A**). The reconstruction of the WT particle was found to have a highly similar cross-correlation score of .883 when compared to another EV-A71 native structure (EMDB ID: 2076). The well-establish canyon
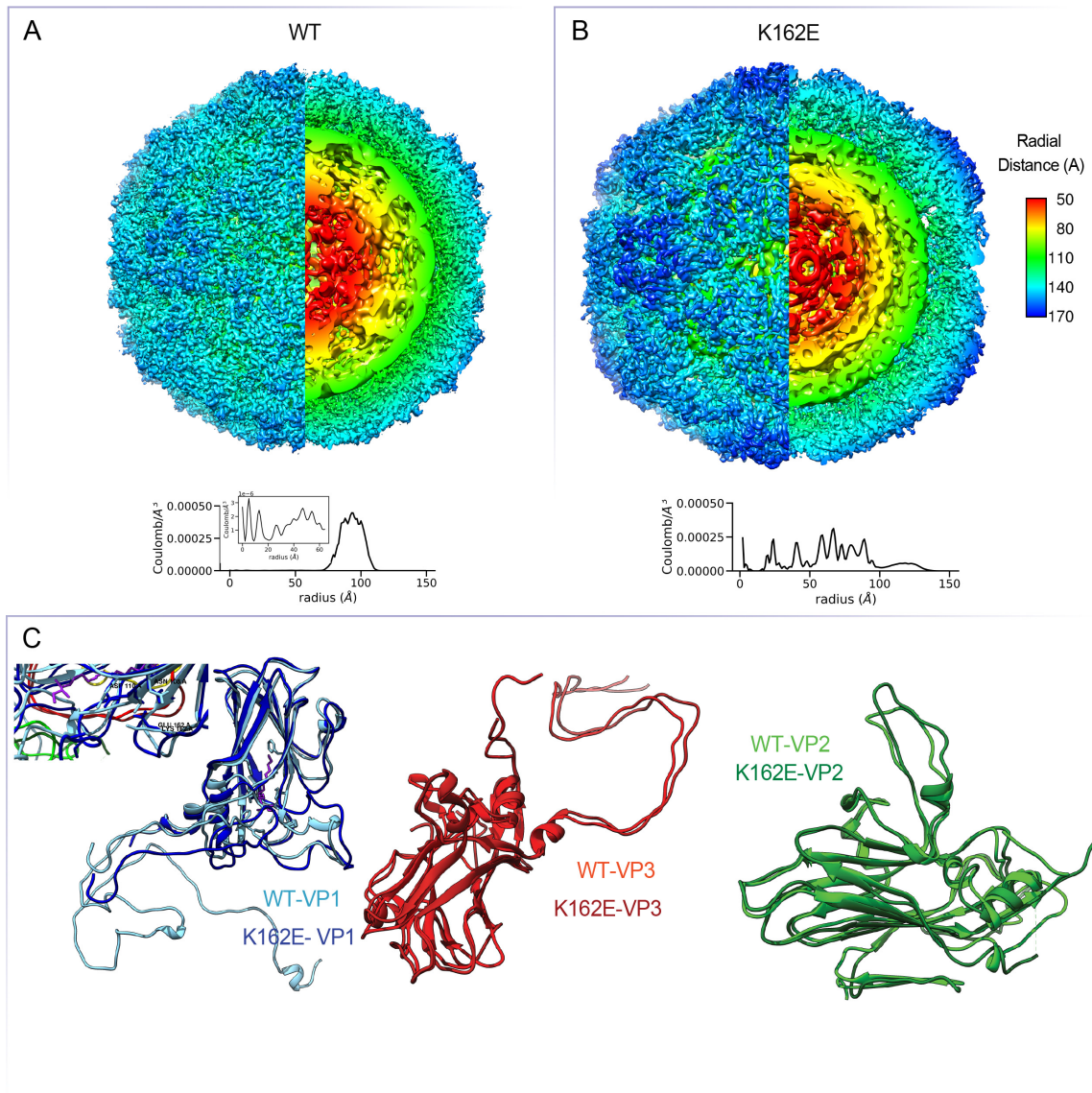
Figure 2.3: Structural determination of WT and K162E
A) WT structures and progression of inactivation and genome uncoating B) K162E structures and progression of inactivation and genome uncoating C) Comparison of mature-state WT and K162E capsomeres D) Comparison of capsomere subunits

around the 5-fold axis was resolved and the lysine in question at position 162 in VP1 was found to not form bonds with nearby residues.

Surprisingly, the single mutation of lysine to glutamic acid in VP1 drastically altered the structure of the native capsid (**Figure 2.3.B**). The capsid was reconstructed to a reconstruction of 4.2 angstroms, with a structure more closely resembling the A-particle of the WT particle. This was reflected by cross-correlation scores of .841 for a previously deposited A-particle EM map (EMDB ID: 5466) while a lower cross-correlation score of .649 against the native state (EMDB ID: 20766). Most dramatically, large pores were observed at the 2-fold axis, similar to those found in the empty particle. However, particles in micrographs were observed to retain their genomes at a similar frequency of the WT native particles, indicating that this A-particle-like state was not ejecting its genome.

Packaged ssRNA structures were determined independently of the outer capsid protein by masking the outer shell of the capsid during 3D reconstruction. In both native states of WT (Figure 3A) and K162E (**Figure 2.3.B** multiple concentric spheres of RNA were resolved. However, the outer layer of the K162E packaged RNA was observed to be expanded from ~70 $\mathring{A}$ of the WT to ~90 $\mathring{A}$ in K162E. As well, a noticeable discontinuity between the RNA-capsid interface in K162E was observed. This may be due to the tightly packed RNA expanding to fill the larger volume of the K162E capsid and releasing tension in the 'entropic spring' of condensed RNA. This is interesting as RNA packing may also play a energetic role during the uncoating process, where the positively-charged ssRNA genome must be compressed to assume the next state.

The reconstructed WT and K162E native capsomere atomic models were overlaid for comparison (**Figure 2.3.C**). The WT capsomere was observed to match already observed structures of the EV-A71 capsomere [198]. The 'swiss-roll' β-barrels found in VP1, VP2, and VP3 were tightly packed with the pocket factor sphingosine. The lysine at position 162 in subunit VP1 was resolved in the Coulomb-density map to not be interacting with nearby residues, instead the positively charged side-chain is observed to be surface-exposed and near

the exit site of the pocket factor. This lysine may be have surface epitope functions, as surface exposed lysines have been observed to play a key role in pathogenesis and cell attachment factor binding [217], [173]. As well, the pocket factor was observed in the Coulomb-density map to still be contained in the VP1 β-barrel. This gives evidence to the lysine having stereochemistry potential to affect pocket factor release and to have an electrostatic affect on cell attachment factor binding.

The K162E structure maintained key structural elements found in the WT structure, with the β-barrel central core appearing to be nearly identical. Overlaying the two structures on top of each other (WT in lighter colors and K162E in darker colors) found key shifts in the exposed loops. Loop GH (residues 204-224) of the VP1 protein (blue) (**Figure 2.3.D**) and the EF loop (residues 132-146) of VP2 (green, Figure 3D) were shifted in confirmation, with GH shifted towards the β-barrel of VP1 and EF becoming more exposed. Both GH and EF have been shown to bind to the primary receptor for EV-A71, SCARB2 [219]. By altering how the GH is folded by stabilizing the nearby region of the mutation both the GH and EF loops' confirmations are altered, as well as changing which binding epitopes are displayed. As well, the new conformation of the VP1 GH appears to block the exit site of the pocket factor, which is required for progressing to the A-particle state. This, coupled with a new hydrogen bond created by the mutated lysine to glutamic acid results in an explanation for the enthalpic stabilization of the capsid. These structures provide the mechanistic evidence that bond-mediated stabilization at the site of pocket-factor release and alteration to exposed loops add additional barriers for state transition.

2.3.6   The WT and K162E Capsid During the Uncoating Process

Mature particles of the WT and K162E were heated at 52°C for 1 hour to convert all particles to either the A-particle or empty state. The A-particle and empty states of the WT particle was resolved to an adequate resolution of 8.0 and 14 angstroms, respectively (**Figure 2.4.A**). The A-particle matches previously described structures (EMDB ID: 5465),
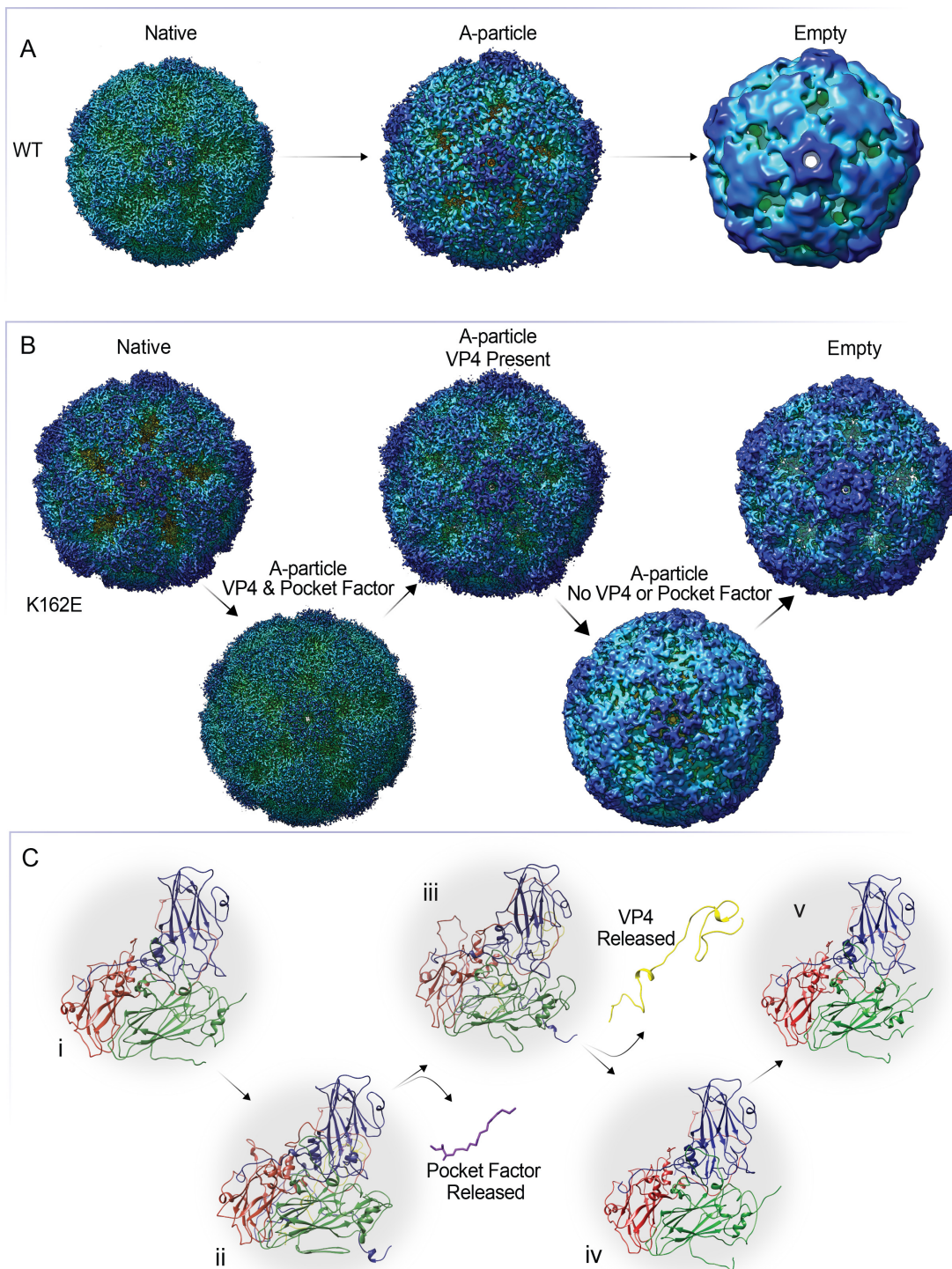
Figure 2.4: Comparison of WT and K162E
A) Progression of uncoating states for WT **B)** Progression of uncoating states for K162E
C) Atomic model of genome uncoating for K162E

with a cross-correlation score of .918. The empty state WT map also matched a previously deposited structure (EMDB ID: 5466) with a cross-correlation score of .954; however, due to the low resolution of the particle reconstruction an atomic model was not created. This may be due to the lower number of particles used in the reconstruction of this Coulomb-density map or from a more intrinsically disordered particle after expansion.

The heated cryoEM data set for K162E was used to reconstruct both A-particles and empty states. Unexpectedly, the heated particles of K162E that contained Coulomb density at the center of the particle, indicative of the A-particle, appeared to shrink in radius to a particle more reminiscent of the native particle observed in WT. As well, the large pores radiating along the 2-fold axis in the K162E native particle were no longer present, despite their reappearance in the K162E empty particle. Furthermore, additional states of the A-particle were resolved during the structural 3D classification and refinement steps. The structural disimilarity between the particles indicate conformationally distinct states that occur during the inactivation and genome ejection pathway. Structures were resolved at 3.1, 7.4, and 5.9 $\overset{\circ}{A}$ resolution using 65.9%, 20.9%, and 13.6% of A-particle-like data. Coulomb density maps were used to determine the presence of both VP4 and pocket factor, finding that each molecule's presence varied by state. A trajectory of irreversible molecule loss was resolved from the presence of these molecules, where the most abundant state contained both VP4 and pocket factor, the second most abundant state losing the pocket factor but retaining VP4, and the least plentiful state containing neither VP4 or pocket factor. This indicates that the pocket factor must be dislodged prior to VP4 loss, and both molecules must both be released prior to complete genome uncoating.

The additional uncoating states represent normally unresolved intermediaries between A-particle and empty particle, which are difficult to resolve due to their phenotypical similarities (non-infectious and still containing the viral genome. The key distinguishing features of VP4 and pocket factor are difficult to resolve fractional presence due to their multiplicity, 60 copies per particle, and small size. Detection by Western blot is possible for VP4 but difficult to be

made quantitative. The 3D classification of these states from a heterogeneous dataset allows for the trajectory of states to be resolved. Additionally, the similarity between the K162E A-particle and the WT native particle gives evidence that the K162E native state may be a structural precursor to the WT native particle. The reason for infectivity of the K162E native state and non-infectivity of the K162E A-particle is not clear, possible that the K162E native state may still need to undergo conformational changes during the uncoating process.

2.3.7 Delayed transition kinetics contrast to increased dynamics in K162E

To gain insights into the kinetic of EV-A71 and K162E EV-A71 at 30 °C and 52 °C we made use of full-atom molecular dynamics (MD) simulations, which provide the appropriate tool to investigate protein dynamics at atomistic resolution. We began our study with the 62.5 ns simulation in an NPT ensemble (constant number of particles N, pressure P, and temperature T) (see Methods) of the EV-A71 WT pentamer solvated in a water box at 30 °C. In **Figure 2.5.A** we represent a top and side view of the pentamer. We built the pentamer consisting of five capsomeres formed by VP1, VP2, VP3, and VP4 capsid proteins using the WT native structure. The pocket factor was also resolved and was included in the simulations (see Methods) (See **Figure 2.5.A**, top view). Overall, the system is very stable and the capsomeres show values of the $C_\alpha \, RMSDs \leq 2 \, \mathring{A}$ with the exception of VP1 of the capsomere a and c and VP4 of capsomere showing RMSDs varying between ≈ 2 to $5 \, \mathring{A}$ (see **Supplemental Figure 2.5**). In contrast to the EV-A71 wild type structure, in the K162E EV-A71 mutant, VP4 and the pocket factor are not resolved and so are not included in the simulations. We built the K162E simulated system following the same procedure used for the wild type system and extended the NPT simulations for 68.1 ns (see Methods). In **Figure 2.5.B**, we represented the top and side view snapshot of the K162E system initial structure and highlighted in licorice yellow format the K162E mutation localized on VP1 capsid protein. The VP1 and VP2 $C_\alpha \, RMSDs$ of K1162E exhibit larger values than those
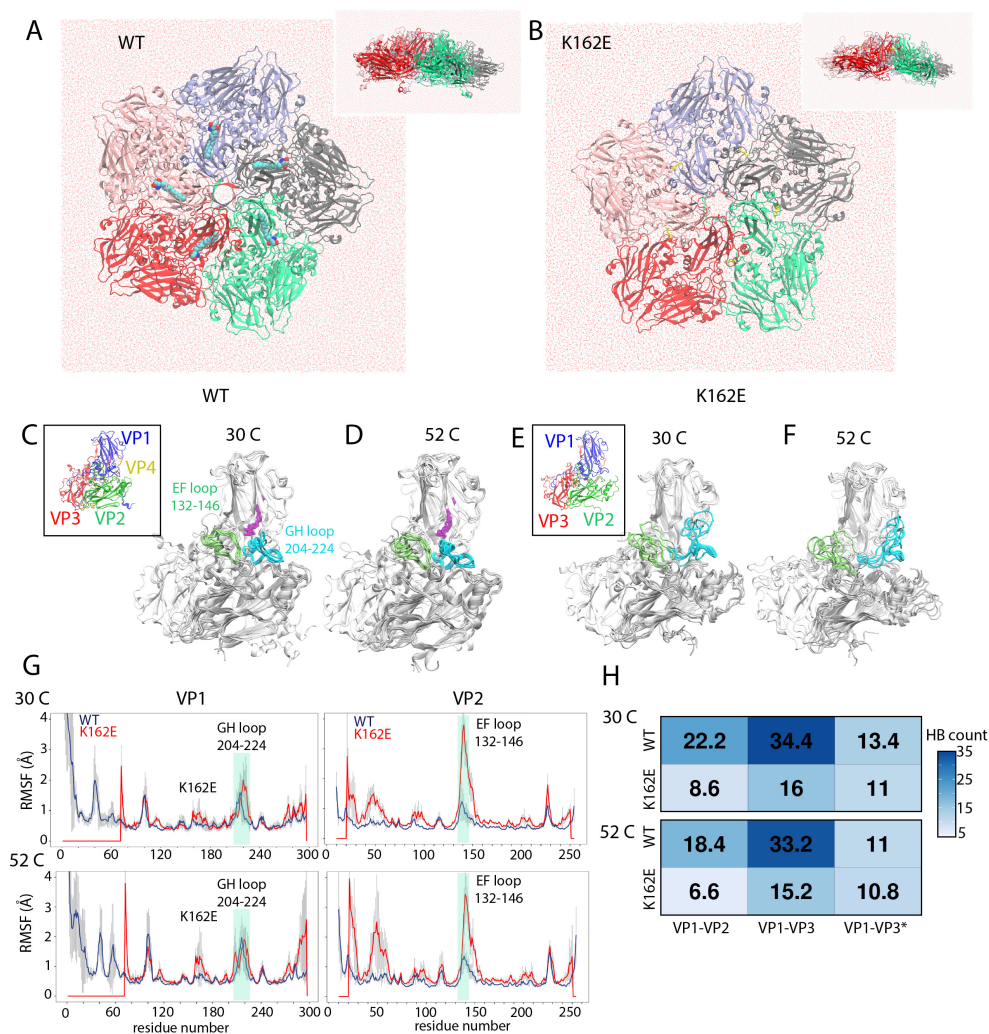
Figure 2.5: Dynamics of the EV-A71 and K162E EV-A71 Pentamers at different temperatures

A) Front and side view of EV-A71 pentamer. B) Snapshot of the K162E EV-A71 system initial structure. Each capsomere is formed by VP1, VP2, and VP3 capsid protein. C-F). Five representative snapshots of the EV-A71 WT and K162E equally spaced in time over the NPT simulations at 30 (**C, E**) and 52° C **(D, F) G)** The VP1 and VP2 RMSFs of the WT (blue) and of the mutant (red) calculated from the simulations. H) Mean number of the hydrogen bond counts between VP1-VP2 and VP1-VP3 belonging to the same capsomere and between VP1-VP3 belonging to adjacent capsomeres

28

of the wild type, whereas VP3 shows $C_\alpha\,RMSDs \approx 2\,\text{Å}$. In **Supplemental Figure 6** we show the snapshots of the initial configuration of the EV-A71 and K162E EV-A71 systems at $52\,°C$ (see Methods). In the wild type, the values of the $C_\alpha\,RMSDs$ of VP2, VP3, and the sphingosines are $\leq\,2\,\text{Å}$, whereas those of VP1 and VP4 fluctuates between ≈ 2 and $5\,\text{Å}$. The high values of the VP1 RMSDs are mostly related to the enhanced dynamics of the N-terminus due to the increased temperature, which is consistent also to the RMSFs calculated over the last 10 ns of the simulations (see **Figure 2.5.G**, left panels). Interestingly, the temperature increase does not affect the region of VP1 and VP2 in proximity of the pocket factor. In the $52\,°C$ K162E system, the VP1 and VP2 $C_\alpha\,RMSDs$ exhibit high values varying between $\approx\,2$ and $5\,\text{Å}$ with the VP1 of capsomere d showing $C_\alpha\,RMSDs \geq\,6\,\text{Å}$, whereas VP3 is very stable ($C_\alpha\,RMSDs \approx 2\,\text{Å}$).

Next, we look at the dynamics occurring in proximity of the pocket factor region. In both WT and K162E systems, the capsomeres exhibit a wedge-shaped, eight-eight-stranded, anti-parallel, beta-barrel topology (**Figure 2.5.C-F** and insets of **Figure 2.5.C,E**) where the connecting loops are structurally different, depending on the specific capsid protein to which they belong [123] [79] [118] [16] and refer to previous paragraphs). **Figure 5C** shows five representative configurations of the capsomere extracted from different frames of the $30\,°C$ simulation spaced equally in time, including the first and the last frame. In both the VP1 GH and VP2 EF loops, the five configuration corresponding to different time point along the simulation nearly overlap meaning that the dynamics is very localized. Such dynamics is not affected by increasing the temperature **Figure 2.5.D**. In addition, the sphingosine appears to be very stable in its pocket in both conditions of room and high temperature. At both temperatures (**Figure 2.5.E-F**), the five configurations of the VP1 GH and VP2 EF loops do not overlap, implying that these loops explore a larger region in space compared to that explored from the WT loops. In order to gain quantitative analysis of the fluctuation range of these loops in the different systems, we calculated the RMSFs (see Methods) at the two investigated temperatures and represented them in (**Figure 2.5.G**). At $30\,°C$ (**Figure**

2.5.G top panels) the VP1 RMSFs of the K162E and the wild type overlap within the errors with the exception of the GH loop, whereas the K162E RMSFs of VP2 consistently exhibit higher values than those of the wild type. Major differences are observed not only in the important region of the EF loop but also in the N-terminus amino acids and in those between residues 30 and 70. At high temperatures (**Figure 5G** bottom panels), K162E VP1 shows an increment in the RMSF values in the region around the K162E mutation in the residues located right upstream from the GH loop. The wild type shows an increment in the RMSF amplitude reaching the value exhibited by the K162E system in the region of the GH loop. The amino acids located around the residue number 100 exhibit an average increment of the RMSF amplitude. In VP2 the K162E RMSF average value exhibits an important increase in the N-terminus region and in the amino acids located between residue 30 and 70 and in the EF loop. On the contrary, the wild type RMSF values remain nearly unaltered upon increasing the temperature.

Finally, we investigated the affect that increased temperature had on hydrogen bonds (HBs) (see Methods) formed between the subunit protein pairs. We looked subunit intractions between VP1-VP2 and VP1-VP3 belonging to the same capsomeres and between VP1 of one capsomere and VP3 of the adjacent capsomere, which we call VP3* (**Figure 2.5.H**). We examined the HBs between these last pairs of capsid proteins because the VP1 K162E mutation is located at the interface between two capsomeres (see Figure 2.5.B). At room temperature the number of HBs exhibited by the WT in the thre investigated subunit pairs is higher than that of the K162E mutant. This is particularly evident when the considered protein pairs belong to the same capsomere. In the wild type, the HB count between VP1-VP2 protein pair exceeds approximately three times that found in the K162E mutant and wheres the HB count between VP1-VP3 protein pair two times. Upon increasing the temperature, the HB count between the VP1-VP2 protein pair drops of approximately the 15% in the wild type and 20% in the K162E mutant. The decrease in the number of the HBs is less noticeable in the VP1-VP3 protein pair. In the interactions between VP1 and VP3*

capsid protein belonging to adjacent capsomeres the HB count drops of approximately the 15% in the wild type and the 1% in the mutant. This indicates that the lower number of HBs in K162E are maintained when the capsid is subjected to increases in temperature.

2.3.8   Increased capsid stability reduces the time for cell entry

Enterovirus capsids are thought to undergo the same conformational changes caused by heating in order to release their genome and infect susceptible cells. Stabilizing the capsid inhibits the N→A transition which precedes genome release. To investigate the differences in cell entry, a one-step growth curve was first carried out in RD cells to compare the replication ability of both WT and thermostabile mutant. Viral RNA replication was assayed by RT-qPCR every 2 hours (**Figure 2.6.A**). While WT was observed to have an exponential phase between 4-6 hours post infection (hpi), the exponential phase was observed to be more gradual between the hours or 4-8 hpi. Similar amounts of viral RNA were detected between 8-10 hpi and the final amount of RNA at the end of the replication cycle, 12 hpi, was about 1 log greater in WT than K162E. The exponential phase was also shifted by 2 hours in the thermostable mutant, same as in the number of genome copies. This was accompanied by a 4 hour shift in the minimum value of the latent phase for infectious units, occuring at 2 hpi for WT and 6 hpi for K162E. However, the number of infectious units were similar at the end of the replication cycle when measured by $TCID_{50}$. These data suggest that cell entry was slowed by the increased thermostability of the capsid.

2.3.9   Measuring rate of entry

To probe the increased amount of physical particles required to initiate an infection, the cell entry process was examined by entry kinetics (**Figure 2.5.B**). The compound neutral red, when incorporated in the viral capsid, has been shown to fix non-enveloped viruses when exposed to white light and has been used to determine the rate of genome release in Enteroviruses [67]. Neutral-red incorporated virus is then inactivated by white light exposure

31
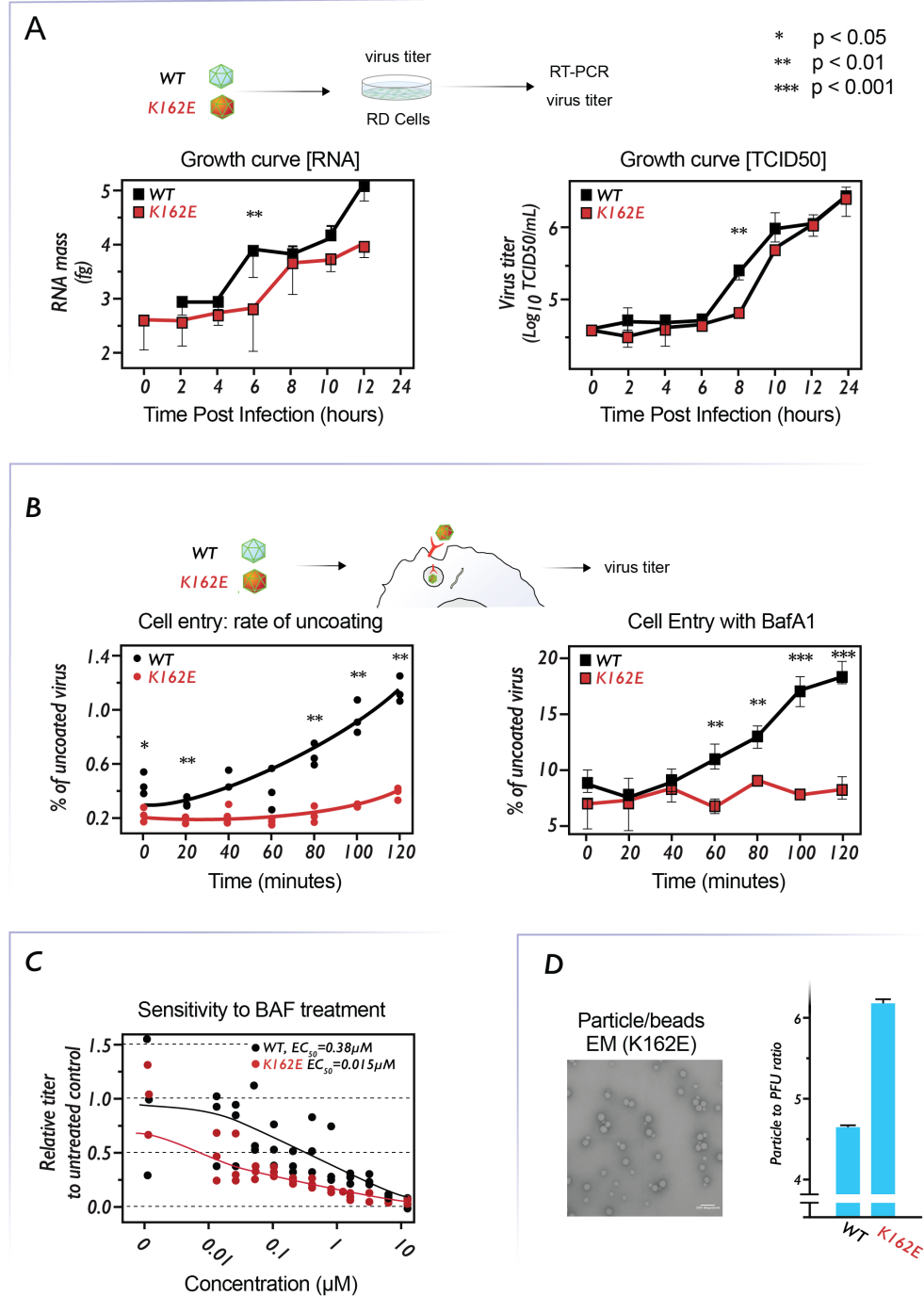
Figure 2.6: Cell entry is inhibited by stabilization of the capsid
A) One-step growth curve of WT and K162E measured by either total viral genomic RNA or infectious units **B)** Rate of cellular entry in RD cells measured by neutral red assay and perturbed with Bafilomycin A1 (BafA1) **C)** IC_{50} of BafA1 on WT or K162E cell entry **D)** Ratio of physical particle measured by electron microscopy compared to infectious units

while capsids which have uncoated their genome are no longer affected. WT and K162E were both allowed to replicate in RD cells in the presence of 20 μM neutral red for 12 hours to incorporate neutral red particles into the capsid, producing neutral red virus (NR-virus). NR-virus was allowed to bind and begin the infection process, with time points taken every 20 minutes to measure still-encapsidated RNA genomes. Successfully uncoated NR-virus was allowed to replicate and were titered. It was found that the thermostable mutant released it's genome at a slower rate, only releasing 40% of its genomes after 2 hours while WT had released 100% of its genomes. This confirms the main hypothesis of this article, that stabilizing the capsid results in decrease in the ability to enter the cell.

To determine if SCARB2-mediated uncoating during endocytosis, which acts by lowering the activation energy of A-particle formation as shown in **figure 2.2.F**, a chemical perturbation was made to the endosome acidification process by the addition of Bafilomycin A1 (**Figure 2.5.B**). BafA1 is known to inhibit the acidification of the endosome by the inhibition of the V-ATPase's proton pump [87]. 1 μM BafA1 was added to cells at least 1 hour prior to the addition of NR-virus and the percent of uncoated RNA genomes was measured as previously described. WT was found to be 18% uncoated after 2 hours and there was no change in uncoating was found for K162E. For the same level of endosome de-acidification it is shown that genome uncoating is completely inhibited for K162E while moderate uncoating is found for WT.

To determine what the effective concentration of BafA1 required to inhibit viral entry the compound was titrated in RD cells prior to WT and K162E inoculation (**Figure 2.6.C**). BafA1 was added at least 1 hour prior at varied concentrations and cells washed prior to the addition of virus to remove the confounding effect of capsid inactivation. Infected cells were allowed to replicate virus until 8 hours post infection where the number of successful replications was titered by $TCID_{50}$. The EC_{50} of inactivation was found to be 0.38 μM for WT and 0.015 μM for K162E, representing approximately a 20-fold increase in inhibition.

To determine if the number of physical particles required for a successful infection were

also affected, the specific infectivity viral particles were calculated (**Figure 2.6.D**). Specific infectivity was calculated by the ratio of physical particles to infectious units. The concentration of physical particles was measured against a 50 nm latex bead standard with known concentration and the concentration of infectious particles was measured by plaque assay. The number of physical units required to initiate a successful infection, in cell culture, was found to be increased about 20-fold by the introduction of K162E. As the number of infectious units produced by a successful infection at the end of a replication cycle was found to be comparable in both WT and K162E, this suggests that K162E produces more physical particles after one replication cycle. An increase in physical particles produced may be due to the higher stability of the overall capsid, such that the hypothesized reversible capsid assembly process becomes forward-driven.

2.3.10 Attenuation in cell culture is not replicated in animal models

While cell culture comparisons of WT to K162E found the thermostabilizing mutation to have a detrimental effect on viral replication, the same mutation was observed to increase mortality in animal models. MP4, a mouse adapted strain of EV-A71 4643, was reverse-mutagenized with the same mutation (MP4-K162E) and inoculated into hSCARB2-expressing mice [95] via the I.P. route. A survival curve was constructed by observing the percent of surviving mice with either WT vs. K162E inoculation (**Figure 2.7.A**). Surprisingly, MP4-K162E killed all but one mouse while the majority of MP4-infected mice survived. This contradicts the cell culture data where K162E replicated at a slower rate due to delayed genome uncoating.

To investigate if the structural change to the K162E capsid resulted in lowered immune detection, a neutralization assay was performed using blood-serum collected from mice previously inoculated to MP4 (**Figure 2.7.B**). Unexpectedly, no significant difference was found between the neutralization levels of WT or K162E. Serum from two different mice was used
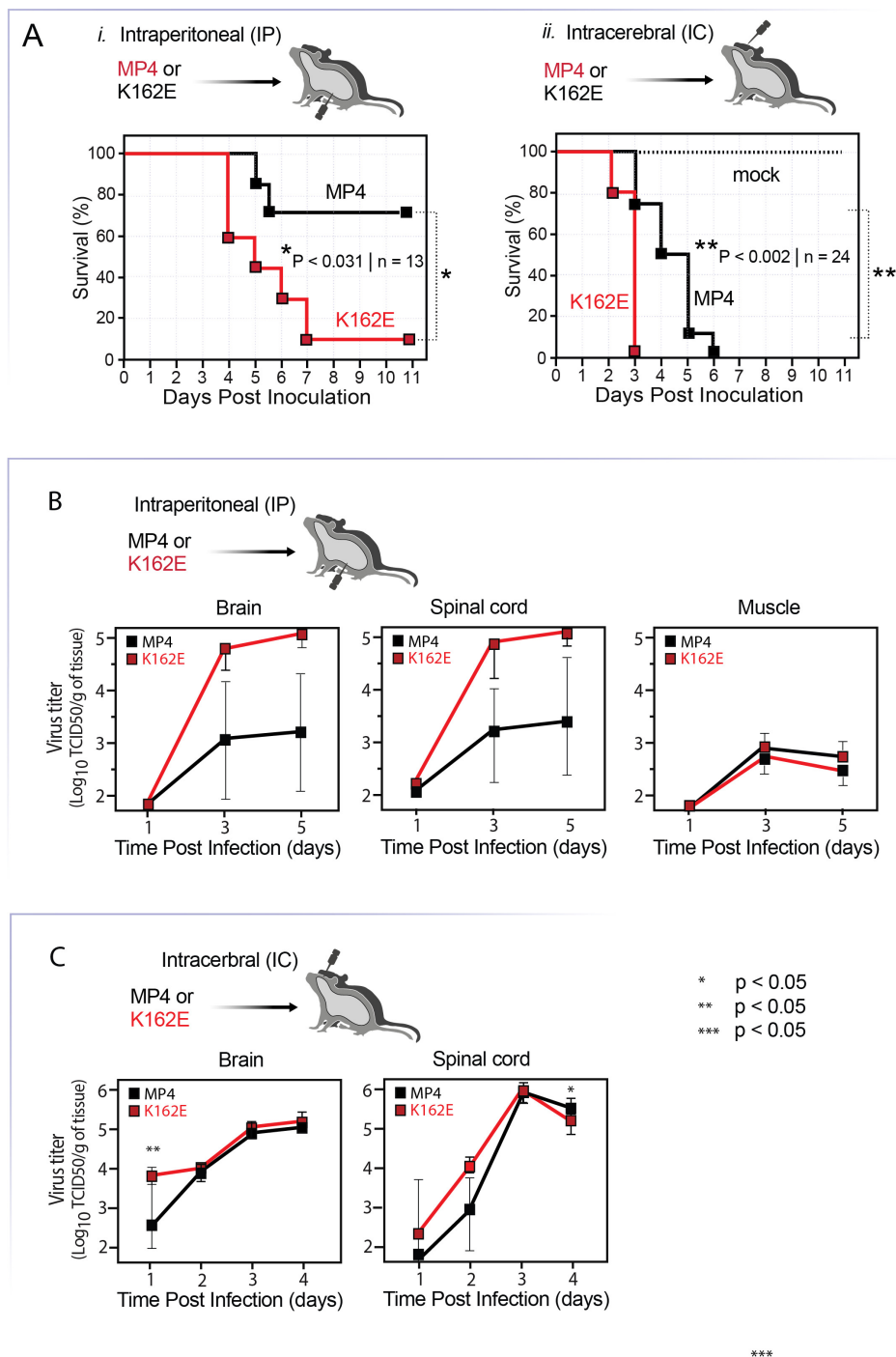
Figure 2.7: Virulence is increased in animal model
A) Survival curve in hSCARB2 mice infected either by I.P. (i) or I.C. (ii) **B)** Tissue distribution of WT or K162E in brain, spinal cord, or muscle following I.P. inoculation **C)** Tissue distribution of WT or K162E in brain and spinal cord after I.C. inoculation

for neutralization without any noticeable change. This suggests that the immune response in the form of neutralization antibodies should not differ by the introduction of the mutation K162E. To assay whether the increased neuro-prevalence of K162E is due to neuro-invasion, the confounding factor of the blood-brain barrier (BBB) was removed by inoculating both MP4 and MP4-K162E directly into the brain. A survival curve was obtained for intra-cranial (I.C.) inoculation. All mice were dead by day 4 in the MP4-K162E group and day 7 for the MP4 group. The survival curve indicates that neuro-invasion is not the cause of increased neuropathogenesis and that enhanced replication within the immuno-privileged CNS is the cause of accelerated mortality.

To further investigate altered pathogenesis by K162E, viral tissue distribution within mice was assayed by collecting titers within individual organs 1, 3, and 5 days post infection via I.P. (**Figure 2.7.B**). The most striking difference was found in replication in the brain, where similar levels of MP4 and MP4-K162E virus were detected at day 1 followed by greater than 2-log increase in viral titer of MP4-K162E at day 5. This accelerated replication was found again in the spinal cord, where similar levels of virus on day 1 were compared with about a 2-log difference in viral titer by day 5. The increased replication in neuronal tissues were contrasted with no noticeable difference in replication in muscle tissue and the lack of replication in blood samples (data not shown). This suggests that K162E gains an increased ability to replicate in the CNS.

To view the replication kinetics in the central nervous system, the tissue distribution of both viruses were found after I.C. inoculation. Tissues were collected from I.C. inoculated mice on days 1-4 post inoculation (**Figure 2.7.C**). MP4-K162E appears to have already replicated to higher levels on day 1 in brain tissue. For brain samples the measured titers are almost identical for the following days 2-4, of which mortality is observed in both MP4 and MP4-K162E mice. As the MP4-K162E group, compared to the MP4 group, has a considerably higher level of mortality on day 4, similar levels of virus titer in brain, virus-induced mortality is implied to be due to replication in the spinal cord. Indeed, MP4-K162E

is detected at higher levels except for day 4, where a decrease in titer observed. This enhanced replication in the spinal cord may be due to earlier spill-over from the brain due to higher titers early on in the pathogenesis. While the mechanism of K162E-induced neurovirulence is unclear, it can be said that the mutation accelerates the neuro-replication. Further animal model studies are required to better understand how viral mutations can accelerate the replication in specific tissues despite an observed lag in cell-entry.

2.3.11 Discussion

In this study we have provided evidence that adaptation to the selection factor of thermostability comes with the evolutionary trade-off of lowered ability of cell entry. We have shown an adaptation to a the selection of increased extracellular temperature has an expected decrease in the ability to enter the cell. By examining the biophysical process and structural context of heat-mediated genome uncoating and its parallel biological process of genome uncoating during cell entry, the many roles and phenotypic tradeoffs of the Enterovirus capsid can be brought to light. This tradeoff appears to be due to both large structural rearrangements in the capsid subunits which lead to a greater energetic barrier for uncoating and enhanced flexibility in specific, exposed, peptide loops.

The observed entry process of SCARB2 binding, cell internalization by clatherin-mediated endocytosis and finally genome uncoating is mirrored by heat-catalyzed uncoating. The transition along an energy landscape from native particle to A-particle replicates the SCARB2-catalyzed transition. The transition then to genome release from the primed A-particle in the absence of a lipid bilayer and numerous cell factors is compensated by elevated temperature and brownian motion, concluding that increasing the activation energy between these states results in delayed cell entry. We have shown that the K162E mutation adds additional states to these estabilished states to reduce the observed kinetic transition from native to A-particle.

The multifunction protein, the virus capsid, then is said to have multiple, often conflicting

roles. We establish that thermostability and cell entry are at odds with one another, yet we were not able to anticipate the enhanced neurovirulence this mutation carries. Stronger binding to SCARB2 and reduced binding to PSGL1 or heparin offer a conjecture of altered cell tropism backed up by changes in tissue replication. Our reported mutation appears to have global effects on the structure of the capsid, with rearrangements of exposed loops which alter the protein's function.

This study also only offers an in-depth look in one mutation's phenotypic trade-offs. While the genetic screen of artificial selection passaging of viral quasi-species reveals one of the stronger thermostabilizing mutations observed to date, it is unclear why this mutation of all possible mutations was fixed in the population. To truly conclude there is an evolutionary trade-off between thermostability and cell entry, genome-wide deep-sequencing studies would need to be conducted on passaged populations of EV-A71 or other enteroviruses. Determining the control, thermostability, and cell entry fitness values for each possible mutation might reveal hotspots of shared phenotype function, residues that function for only one phenotype, or inert locations with little effect on either function.

2.3.12   Acknowledgments

2.4 Author Contributions

A.C. conceived of this study. A.C., M.T.Y., and S.C. designed the experiments. A.C. prepared, collected, and analyzed CryoEM data. M.T.Y. performed the animal experiments. S.C. designed and carried out the MD simulations. R.A. and S. B. provided guidance and support. All authors wrote the manuscript.

2.5 Method Details

2.5.1 Cells and Viruses

RD cells were obtained from ATCC© (CCL-136) and maintained in Dulbecco's Modified Eagle Medium (DMEM) supplemented with 10% Fetal Bovine Serum and 1X Penicillin-Streptomycin-Glutamine at 37° at 5% CO_2. The EV-A71 strain used in this study was the 4643 strain isolated from the 1998 epidemic in Taiwan [213], which had been ligated onto the pUC plasmid.

2.5.2 Animals

C57BL/6 mice with the hSCARB2 transgene (doi:10.1073/pnas.1217563110) were obtained from Dr. Satoshi Koike (Tokyo Metropolitan Institute of Medical Science, Tokyo, Japan). Mice were bred in-house and maintained in a 12/12 light cycle with standard chow diet under specific-pathogen free condition in the AAALAC-certified animal facility at UCSF. Both male and female, four to five-week-old mice were used in this study.

2.5.3 Propagation and titering of virus

Using infectious cDNA clones of EV-A71 strain 4643, the carrying plasmids were linearized then used as a template for in vitro transcription of single strand genomic RNA (ssRNA). 20 μg of RNA was transfected into 4.0×10^6RD cells. Resulting virus was propagated in RD

cells from a passage 0 (P0) stock to form the initial passage 1 (P1) population. All viral populations were titered by either $TCID_{50}$ or plaque as described previously[?].

2.5.4 Passaging virus under temperature selection

The initial virus passage (P1) was either kept on ice for 1 hour (control passage) or heated at $46^{o}C$ for 1 hour (heated passage) before being added to a flask of 10^7 RD cells. Virus was titered before and after heating to ensure each passage was started with 10^5 TCID50 of virus for a consistent multiplicity of infection (MOI). After 24 hours the flasks were checked for cytopathic effect (CPE) and frozen at $-80^{o}C$, three cycles of freezing and thawing at room temperature were performed to lyse viruses from cells. Supernatant from each flask was centrifuged at 2500xg for 5 minutes to pellet cellular debris, resulting supernatant was stored at $-80^{o}C$ and used for subsequent passages. Viral supernatant from each passage was further amplified at an MOI of 5 in 10^7 RD cells, allowed the viruses to replicate for 8 hours, then lysed by Trizol [citation needed] and RNA was extracted by phenol-chloroform. RNA was reverse transcribed using Superscript III [citation needed] and primers specific to the P1 region of viral genome. Amplified cDNA was then used for Sanger sequencing and mutations were probed for in each passage.

Generation of mutant virus from cDNA   Using the previously mentioned infectious clone of EV-A71 4643, the plasmid was linearized and used as a template for *in vitro* transcription of single strand RNA (ssRNA). 20 μg of ssRNA was then transfected into $4x10^6$ RD cells. Transfected ssRNA was allowed to replicate to produce viral particles.

2.5.5 Virus purification

EV-A71 was propagated in 20 100 mm dishes of confluent RD cells. Upon total CPE, virus particles were lysed with 0.5% IGEPAL CA-630 and followed by three cycles of freeze-thaw. Resulting supernatant was then centrifuged for 5 minutes at 3000xg to pellet cell debris and

resulting supernatant was then precipitated with 8% final concentration PEG 8000 at 4ºC for 72 hours. Virus was pelleted at 3000xg for 1 hour, re-suspended in purification buffer and remaining debris pelleted at 3000xg for 15 minutes. Supernatant was then purified through a 30% sucrose cushion centrifuged at 100,000xg for 3 hours followed by fractionation by 15-45% sucrose gradient at 100,000xg for 3 hours. Fractions were then dialyzed by Zeba desalting column and concentrated using a Amicon 100,000 MWCO filter.

Thermostability assay   Purified virus samples were heated using calibrated water heat bathes set for indicated temperatures. Samples were added to the heat bath simultaneously and removed at indicated timepoints and placed on ice for at least 5 minutes. Samples used for genome quantification were treated with RNase If for 30 minutes at 37ºC followed by RNA purification by phenol-chloroform extraction and precipitation by isopropanyl-sodium acetate.

2.5.6   Particle Stability Thermo Release Assay

Particle Stability Thermo Release assay (PaSTRy) was performed as previously described [citation needed]. Briefly, purified particles were aliquoted in qPCR tubes with either SYPRO orange, to measure the level of protein unfolding as a proxy for A-particle formation, and SYTO9, a RNA-sensitive dye that reports the release of viral RNA. Samples were gradually heated in a BioRad CFX Connect thermocycler between 4°C and 95°C, relative fluorescent units (RFUs) were taken every 0.5°C.

2.5.7   Viral genome quantification

Genome quantification was performed by RT-qPCR using NEB's Luna One-Step kit. Primers [ATTTCAGCGGCTTGGAGTGC] and [GCAGCCCAGAAGAACTTCAC] were used with viral samples or IVT genomic RNA for standard curves. Samples were run on a BioRad CFX Connect thermocycler. Cq values were used to determine viral genome copy numbers.

2.5.8 Viral particle quantification

Known titers of purified mature viral particles were mixed with known concentrations of 50 nm latex beads. Samples were then imaged by negative-stain electron microscopy. Electron micrographs were then used to determine the ratio of viral particles to latex beads and calculate the concentration of viral particles. Ratios of viral particle concentrations and titer were used to determine viral particle to infectious unit ratios.

2.5.9 Neutral red assay

Neutral Red virus were produced by inoculating RD cells with viral stock and allowing virus to attach and enter cells over 1 hour at 37°C. Inoculum was then removed and replaced with viral media containing 20 μM neutral red. Flasks of infected cells were wrapped in foil then returned to a 37°C incubator for 24 hours. Viral supernatant was obtained as previously described and kept in darkness. During assaying Neutral Red virus was serially diluted and added to 6-well plates of 5x10^5 RD cells/well in 500 μL aliquots.

2.5.10 Chemical perturbation assay

RD cells were incubated with the indicated amount of compound for at least 1 hour prior to inoculation with virus. Viral inoculum also contained the indicated concentration of compound prior to inoculation and was added to 5x10^4 cells in a 24-well plate. Virus was allowed to attach and enter cells for 1 hour at 37°C before inoculum was removed and replaced with cell culture media containing the same concentration of indicated compound. The virus was allowed to replicate at 35°C for 8 hours before the plates were moved to a -80°C freezer to halt replication. Samples were freeze-thawed 3X before being centrifuged to remove cell debris. Resulting supernatant was then titered.

2.5.11   Western Blot

Purified viral capsids were pre-treated with 10 ng of sequencing grade Trypsin (Promega) prior to denaturing sample with 2X Laemeli buffer (BioRad). Samples were then heated at 94^oC for 10 minutes followed by cooling on ice for at least 2 minutes. Samples were loaded onto a 4-20% SDS-PAGE gel (BioRad) and electroporated for 1 hour before being equilibrated in transfer buffer for 5 minutes and transferred to an activated PVDF membrane at 40V for 40 minutes then 100V for 1 hour. Membranes were blocked with 3% BSA in TBST buffer overnight at 4^oC with gentle rocking followed by washing 5X with TBST and incubation at RT with primary antibodies against VP2, mAb979 (Millipore Sigma), or VP4, CF594 (Biorbyt), for 2 hours. Membranes were washed 5X with TBST buffer and incubated with secondary antibody anti-rabbit IgG-HRP or anti-rabbit IgG-HRP in TBST buffer at RT for 2 hours. Membranes were washed 5X in TBST buffer and developed using an ECL system (Thermo Fisher). Images were taken using a BioRad ChemiDoc.

2.5.12   Electron microscopy

Negative stain electron microscopy was performed after fixation of purified particle with 0.01% final concentration EM-grade paraformaldehyde. Quantifoil 400 mesh formar copper grids were glow discharged prior to the addition of sample to the gird. Samples were allowed to adhere to grids for 5 minutes followed by wicking away of excess liquid by applying a whatman paper to the edge of the grid. Grids were then washed with deionized distilled H_2O and excess liquid wicked before applying 2% neutral phosphotungstic acid for 30 seconds. Excess liquid was wicked away and grids were imaged with a FEI Tecnai T12 120 kV microscope with a Gatan UltraSacen 895 4k CCD camera.

CryoEM was performed by first preparing grids using a ThermoFisher Mark IV vitrobot. $3 \, \mu L$ of sample was applied to a Quantifoil R 2/1 ultrathin carbon grids for 5 minutes to allow sample to adhere to carbon before excess liquid being wicked away with Whatman paper. Grids were then placed in the vitrobot at 100% humidity and $3 \, \mu L$ of sample applied again

for 1 minute. Excess liquid was then blotted using blot-force 3 for 17 seconds and rapidly plunge-frozen in liquid ethane. Grids were then loaded into either a Talos Arctica or Glacios 200 kV microscope with Gatan K3 detectors. Images were collected on the Arctica at a nominal magnification of 28,000X with a dose rate of 21 e$^-$/pixel/second for 6 seconds for a total of 0.53 e$^-$/$\mathring{A}^2$/$frame$. Images were collected on the Glacios at a nominal magnification of 34,000X at 16.5 e$^-$/pixel/second for 6 seconds for a total of 0.56 e$^-$/$\mathring{A}^2$/$frame$.

2.5.13   Image Processing

Micrograph image stacks were dose-weighted and corrected for beam-induced local motion using MotionCorr2. Images were then CTF corrected using CTFFIND4 within the Relion2 package. From corrected images particles were manually picked and class-averaged within Relion2. High-contrast class averages were used for *ab initio* structure refinement. Particles were used to produce 4 classes of initial maps, from which the best resolved class was used for structural refinement. One round of polishing was used to produce the final Coulomb potential density map. Maps were checked for handedness and masked using a low-resolution map.

2.5.14   Atomic Model Building

UCSF Chimera was used to fit the initial atomic models into the Coulomb potential density maps, PDB:3VBS for WT and PDB:4N53 for K162E. Asymmetric maps were boxed using a 5 $\mathring{A}$ mask created from the inital model and multiple rounds of real space refinement were performed until cross-correlation between model and map was not improved by additional rounds of refinement.

2.5.15   Animal experiments

Four-week-old mice were inoculated with the wild-type MP4 or the MP4-K162E mutant virus via intra-peritoneal (i.p.) route. Infection was performed by injecting 100 μL of inoculum delivering $1x10^5$-$1x10^6$ TCID$_{50}$ of virus per mouse. Survival of inoculated mice were monitored 14 days. Mice with appearance of paralysis on both posterior limbs, the humane endpoint, were euthanized.

2.5.16   Tissue Distribution of Virus in Mice

hSCARB2 mice were intraperitoneally (I.P.) or intracranially (I.C.) inoculated with either wild-type or mutant EV-A71 or viral media as a mock control group. 4 week old mice were I.P.. inoculated with 100 μL of inoculum carrying $1x10^5$ TCID50 of wild-type or mutant EV-A71 virus. For I.C. inoculation, 10 μL of inoculum was injected to deliver $5x10^4$ TCID50 of wild-type or mutant EV-A71 virus. For I.P. innoculated mice, days 1, 3, and 5 post-inoculation mice were used for tissue collection. For I.C. innoculated mice, days 1, 2, 3, and 4 post-innoculated were used for tissue collection. 3 mice from each virus group were euthanized, perfused with 1X PBS, and selected tissues were collected aseptically, weighed, and stored at -80°C. Tissue samples were homogenized in viral medium, disrupted by 3 freeze-thaw cycles and cleared at 1500xg for 10 min at 4°C. Muscle, brain and spinal cord were harvested from i.p. and i.c. infected mice, while blood, spleen, heart, kidney, small intestine and liver were harvested only from i.p. inoculated mice. Virus titer in cleared supernatant was determined by a standard TCID50 assay.

2.5.17   EV-A71 and K162E EV-A71 Simulation setup

The initial coordinates of the EV-A71 pentamer and of the K162E EV-A71 mutant pentamer were extracted from PDB ID 3VBS for WT and PDB ID 4N53 for K162E respectively. The EV-A71 capsomere structure resulted indistiguishable from PDB:6UH1 [16]. We used the

same procedure to minimize, equilibrate, and simulate the two systems at two different temperatures and we described it in the following. The EV-A71 pentamer is composed of 5 capsomeres, each of them including VP1, VP2, VP3, and VP3 proteins, and the sphingosine pocket factor. The K162E EV-A71 pentamer is composed of 5 capsomeres, each of them including VP1, VP3, and VP3 proteins. We used SWISS-MODEL [7] for modeling the missing residues of VP2 and VP3 of the K162E EV-A71 capsomere crystal structure. In all systems, the N- and C-terminus of all proteins forming the pentamers were capped. We modeled all the His amino acids in the Nδ1 tautomeric state and maintained positive charge for Arg/Lys and negative charge for Asp/Glu. The sphingosine was model as neutral. To build the initial cell box, we placed the pentamer in the center of the Cartesian coordinates and overlapped with a water box. Water molecules overlapping with the protein atoms were removed and potassium ions were added to maintain charge neutrality. The EV-A71 simulation system contains $\approx 420\,000$ atoms and the K162E $\approx 515\,000$ respectively.

2.5.18 Full-atom molecular dynamics simulations

All simulations were performed using NAMD 2.14 [92, 93] with the CHARMM36m force field for the protein and ions [90] and the TIP3P model for water [193]. The sphingosine parameter and topology files were courtesy of S. Wheeler (see Acknoledgments). We minimized the system energy using the conjugate gradient algorithm for 8,000 steps and gradually heated the simulated cell from 25 K to 303 K (30 °C) in steps of 25 K. To equilibrate the system, we applied harmonic restraints to the protein and sphingosine backbone, water, and ions, and we released them during consecutive NPT simulations (constant number of particles N, pressure P, and temperature T) of 1 ns length. After this equilibration procedure, we started the production runs. To carry out simulations at the temperature of 52 °C (325 K), we increased the temperature of 22 K and run a 1ns simulation before starting the production runs. For all simulations, we used a Langevin dynamics scheme to keep the temperature constant and an anisotropic coupling in conjunction with Nosé-Hoover-Langevin piston al-

gorithm to keep the pressure constant at 1 atm [150, 62]. Periodic boundary conditions were applied in three dimensions. We employ the smooth particle-mesh Ewald (PME) summation method to calculate the electrostatic interactions [172, 183] and the short-range real-space interactions were cutoff at 12 Åusing a switching function between 10 and 12 Å. To integrate the equations of motion during the production runs, we used a time step of 4 fs for the long-range electrostatic forces, 2 fs for the short-range non-bonded forces, and 2 fs for the bonded forces by means of a reversible, multiple time-step algorithm [70]. The SHAKE algorithm [91] was used. Coordinates were saved every 20 ps.

The EV-A71 pentamer simulation at 303 K (30 °C) was extended for 62.5 ns and that at 325 K (52 °C) for 68.1 ns respectively. The K162E EV-A71 pentamer simulation at 303 K (30 °C) was extended for 62.5 ns and that at 325 K (52 °C) for 56.5 ns respectively. Simulations were carried out partially on the IBM Artificial Intelligence Multiprocessing Optimized System (AiMOS) supercomputer and partially on a cloud bare metal machine.

The simulations were visualized using VMD software [85]. The trajectory analysis were carried out using MDAnalysis [145, 134] and our own codes. The root-mean-squared-fluctuations (RMSFs) were calculating by averaging over the last 10 ns of the simulations. The hydrogen bond (HB) analysis were carried out by using the HBonds VMD plugin [85]. We define a hydrogen when the distance between the donor (D) and the acceptor (A) is $\leq$ 3.5 $\mathring{A}$ and the D-H-A angle is $\leq$ 30°. We calculated the number of hydrogen bonds formed throughout the last 10 ns of the simulations. The data represented in the table in Figure 5H are the mean calculated over the 5 capsomeres and the standard deviation is represented in the SM.

2.6 Supplementary Materials

Table 2.4: Summary Statistics of CryoEM and Atomic Model Building

	WT-native	WT-A-particle	WT-empty	K162E-native	K162E-A$_1$-particle	K162E-A$_2$-particle	K162E-A$_3$-particle	K162E-empty
# particles	20699	1316	848	12966	2094	604	246	162
Map resolution (A)	3.3	8	14	4.1	3.1	7.4	5.9	7.1
Detector pixel size (A)	0.72	0.72	0.72	0.603	0.72	0.72	0.72	0.7
Nominal magnification	28000	28000	28000	34000	28000	28000	28000	28000
Electron exposure (e$^-$/A^2)	62	62	62	68	62	62	62	62
Voltage (kV)	200	200	200	200	200	200	200	200
Atomic Model								
Cross-Correlation	0.85	0.62		0.74	0.83	0.64	0.71	0.61
MolProbity Score	1.44	2.01		2.99	1.51	2.19	1.73	2.46
Clash Score	6.43	11.06		10.93	4.49	10.39	7.70	15.57
Poor Rotamers	0.14	0.17		8.41	0	0	0	8.35
Favored Ramachandran	97.6	92.95		79.86	96.04	91.73	95.5	96.55
Allowed Ramachandran	2.4	6.9		19.42	3.96	8.27	4.5	3.45
Disallowed Ramachandran	0	0.15		0.72	0	0	0	0
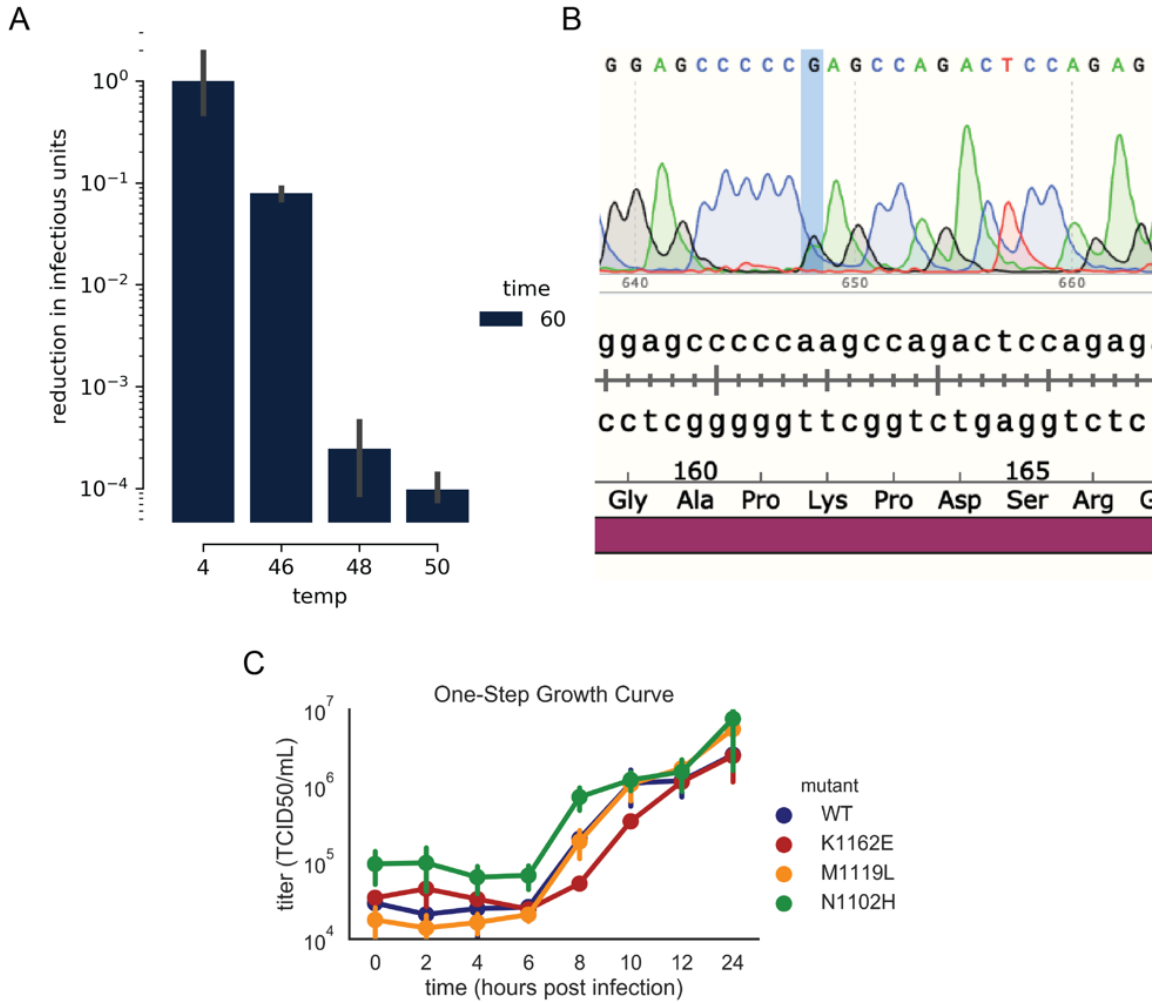
Figure 2.8: Validation of Selected Mutants
A) EV-A71 population reduction at given temperatures for 1 hour, titered by TCID50 **B)** Observed mutation A-¿G at position 2924 from heated passage 6. **C)** One-step growth curve of identified mutations from passaging
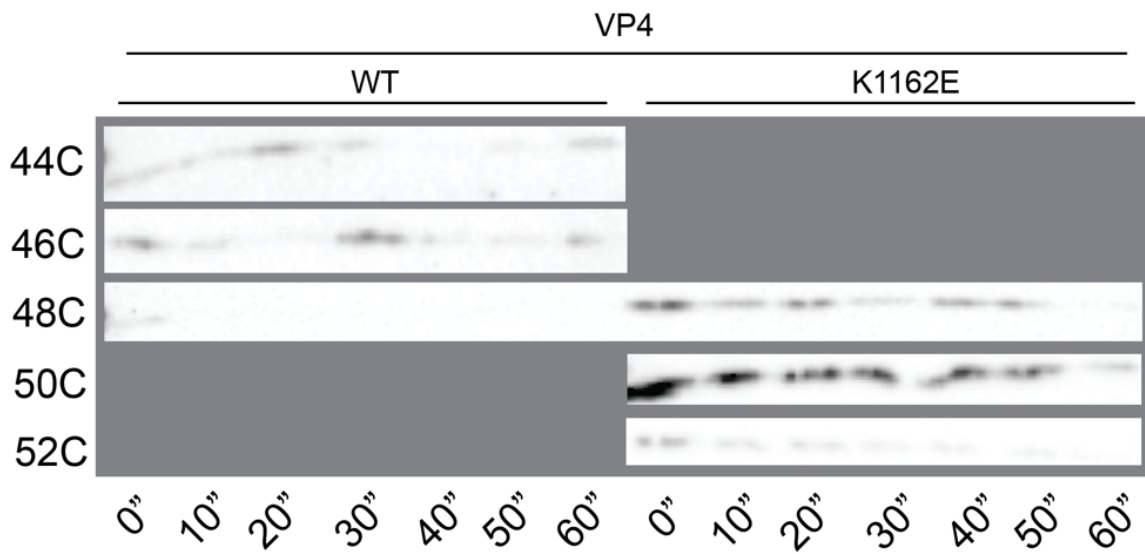
Figure 2.9: Measurement of VP4 Loss by Western Blot

Western blots of protein VP4 from purified and heated WT and K162E capsids.
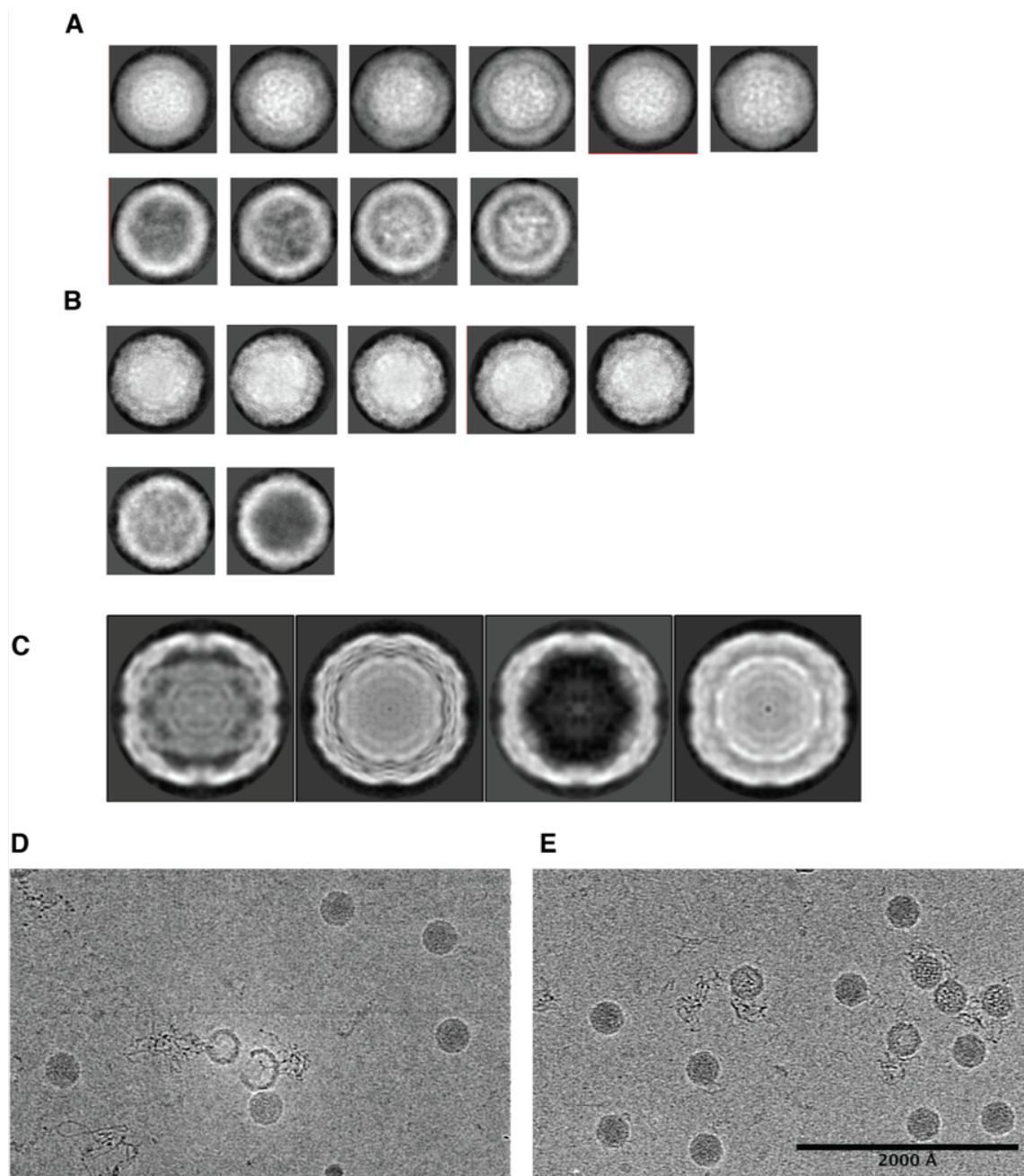
Figure 2.10: Images of Heated WT and K162E Particles
A) 2D class averages of heated WT particles, either used for A-particle (top row) or empty particle (bottom row) reconstruction **B)** 2D class averages of heated K1162E particles, either used for pre-A, A-particle, or post-A (top row) or empty particle (bottom row) reconstructions **C)** Projections of 3D class averages of heated K1162E particles. From left to right, projections are of empty, A-particle, post-A, and pre-A states **D)** Sample micrograph of heated WT particles **E)** Sample micrograph of heated K1162E particles
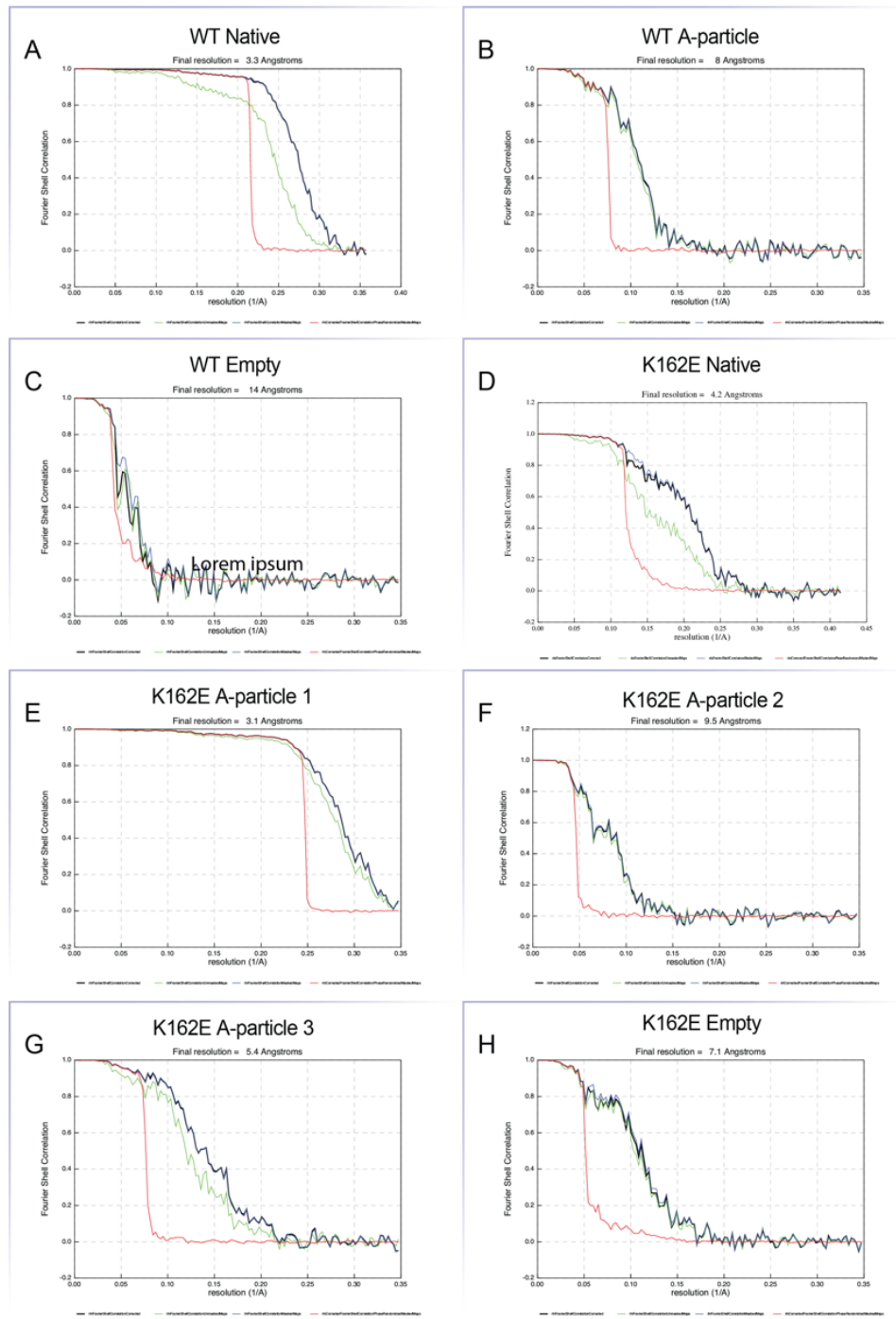
Figure 2.11: FSCs of Structures
Final resolution calculated by gold-standard 0.143 cutoff of masked maps (blue). Also shown are FSC corrected (black), FSC unmasked (green), and FSC phase-randomized masked (red).
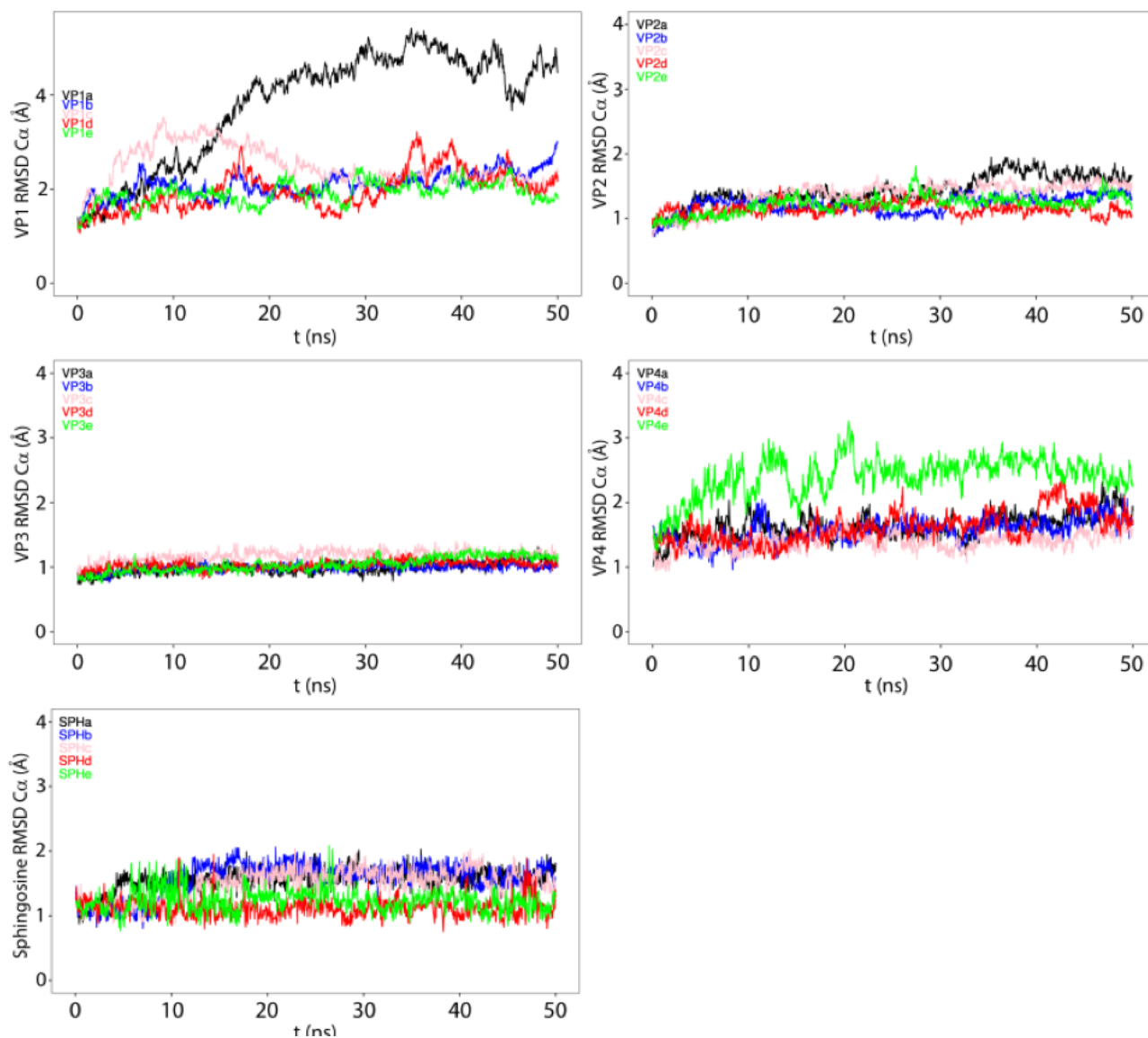
Figure 2.12: RMSD of Capsid Proteins and Pocket Factor at 30°C
Time evolution of the root mean-squared deviations (RMSD) of the VP1, VP2, VP3, and VP4 capsid proteins and of the sphingosine pocket factor for NPT simulations of the EV-A71 wild type carried out at 30 C. The panels show the time evolution of the RMSD of all the capsid proteins and sphingosine forming the five protomers (protomer a: black; b: blue; c: pink; d: red; e: green)
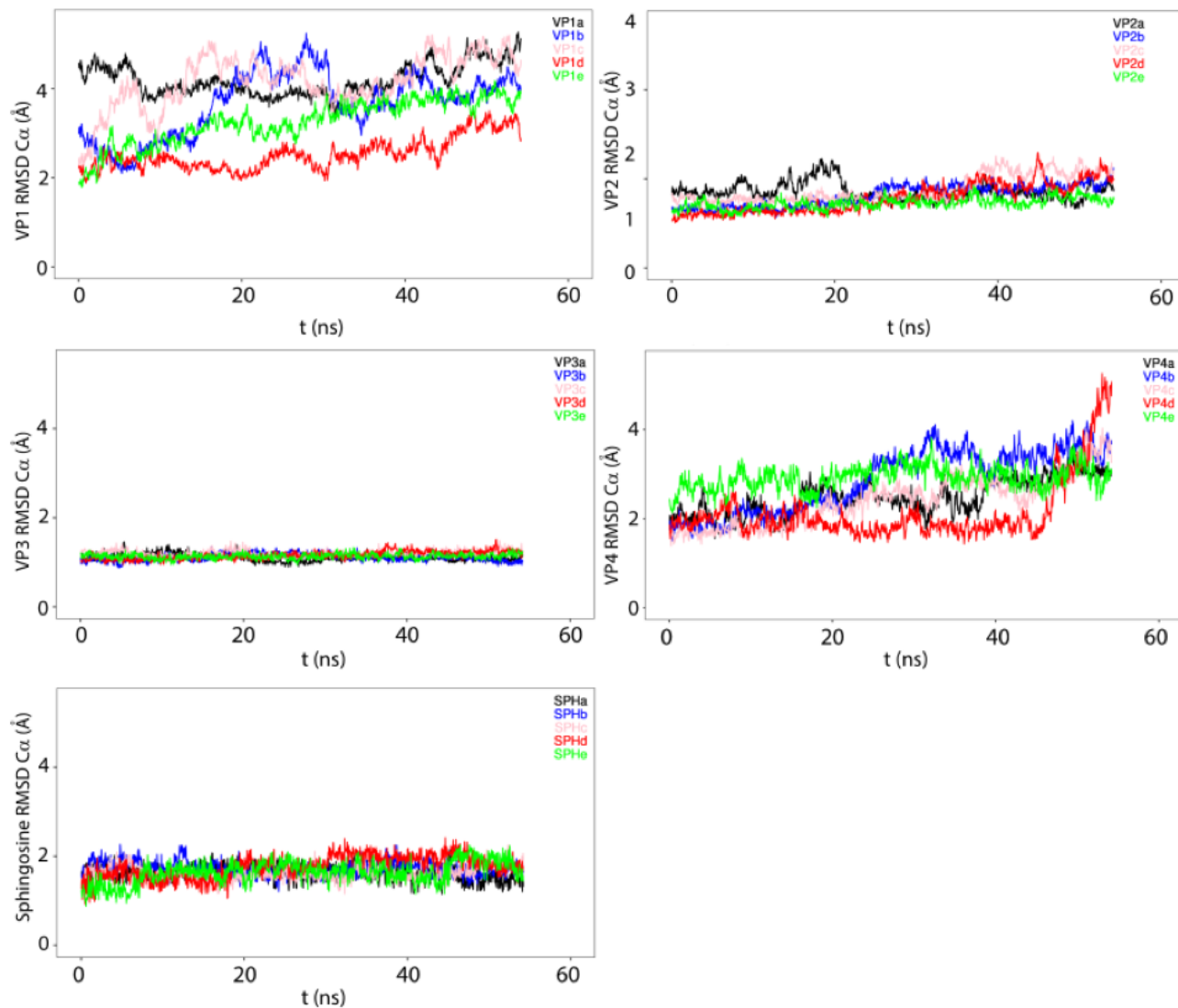
Figure 2.13: RMSD of Capsid Proteins and Pocket Factor at 52°C
Time evolution of the root mean-squared deviations (RMSD) of the VP1, VP2, VP3, and VP4 capsid proteins and of the sphingosine pocket factor for NPT simulations of the EV-A71 wild type carried out at 52 C. The panels show the time evolution of the RMSD of all the capsid proteins and sphingosine forming the five protomers (protomer a: black; b: blue; c: pink; d: red; e: green)
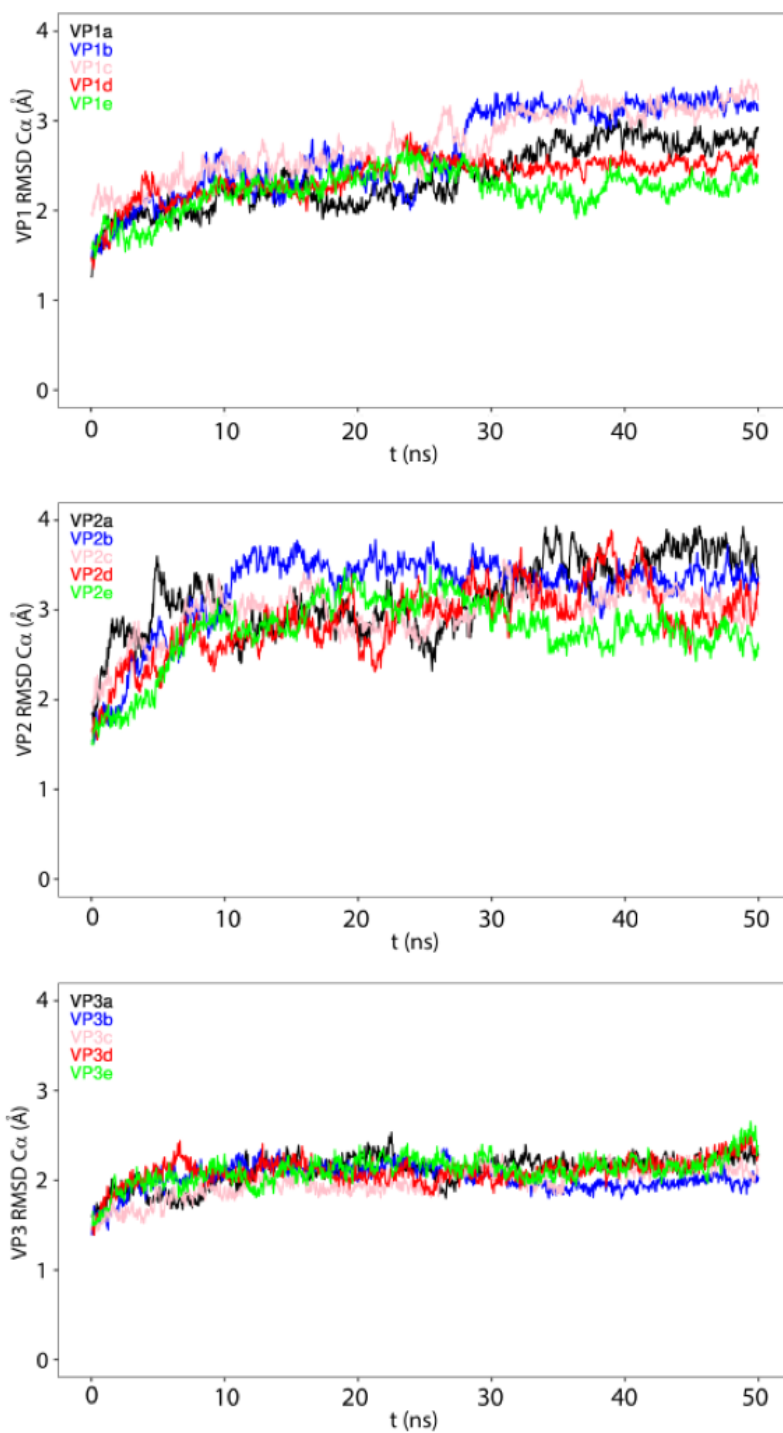
Figure 2.14: RMSD of K162E Capsid Proteins and Pocket Factor at 30°C
Time evolution of the root mean-squared deviations (RMSD) of the VP1, VP2, and VP3 capsid proteins for NPT simulations of the EV-A71 K162E mutant carried out at 30 C. The panels show the time evolution of the RMSD of all the capsid proteins and sphingosine forming the five protomers (protomer a: black; b: blue; c: pink; d: red; e: green)
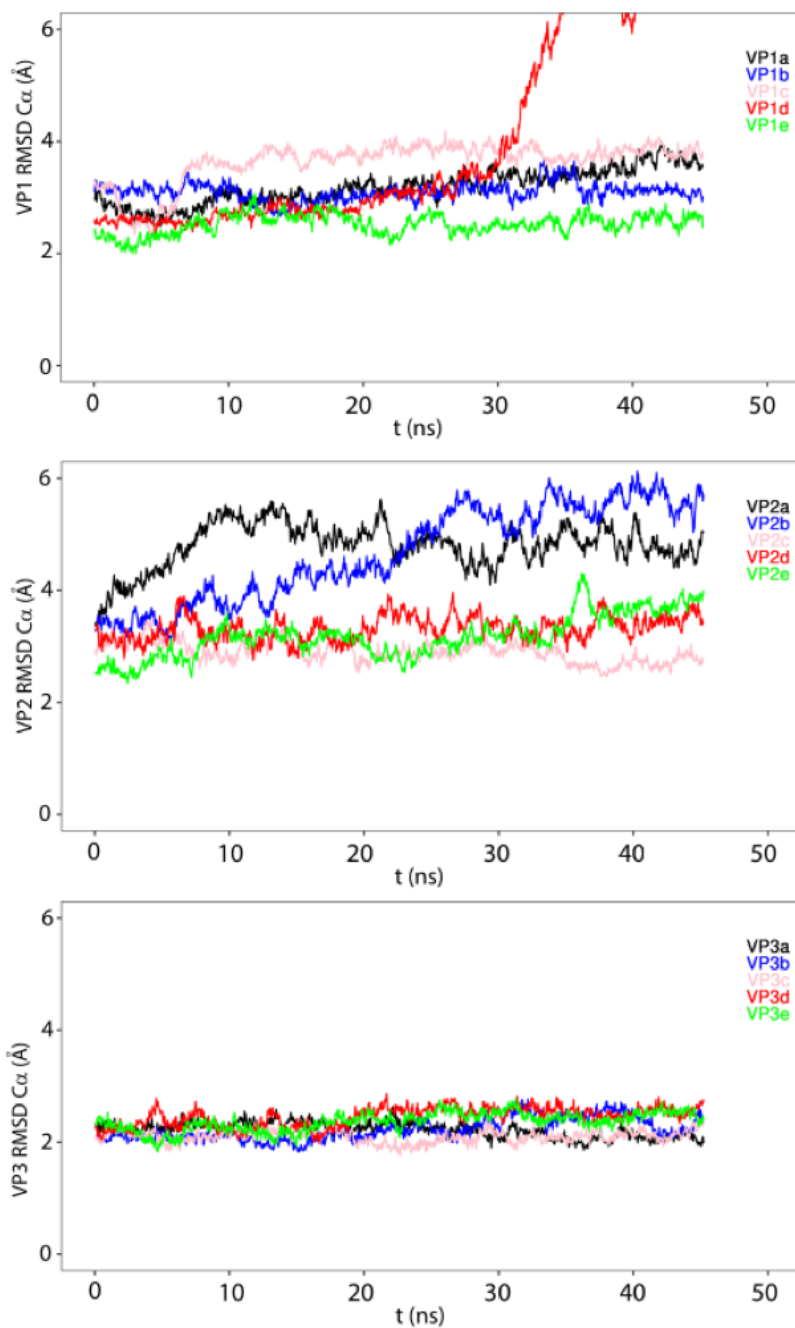
Figure 2.15: RMSD of K162E Capsid Proteins and Pocket Factor at 52°C
Time evolution of the root mean-squared deviations (RMSD) of the VP1, VP2, and VP3
capsid proteins for NPT simulations of the EV-A71 K162E mutant carried out at 52 C.
The panels show the time evolution of the RMSD of all the capsid proteins and sphingosine
forming the five protomers (protomer a: black; b: blue; c: pink; d: red; e: green)
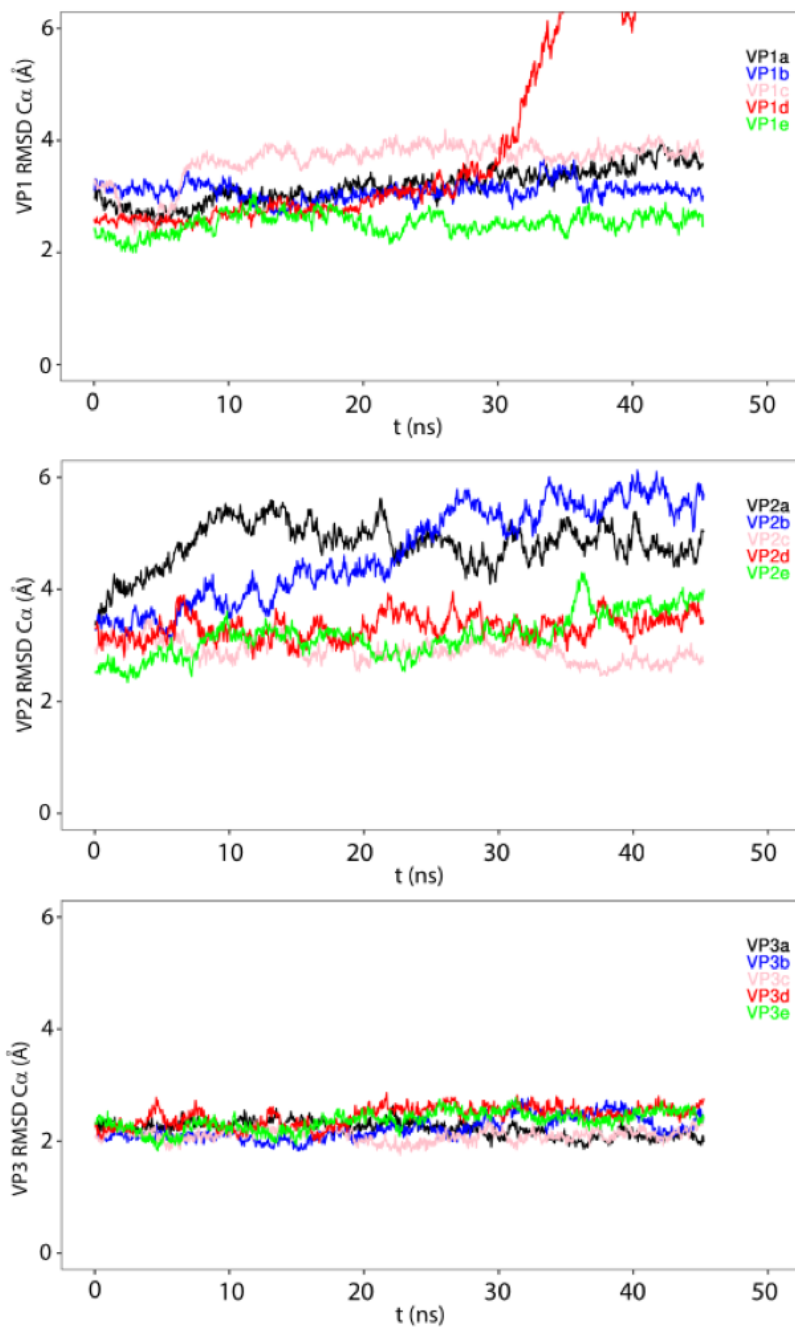
Figure 2.16: SD of WT and K162E HB
Standard Deviation (SD) of the Hydrogen Bond (HB) count between VP1-VP2 and
VP1-VP3 belonging to the same protomer and between VP1-VP3 belonging to adjacent
protomers (VP1-VP3*). The standard deviation is evaluated by considering the five
protomers forming the pentamer.

Chapter 3

Coxsackievirus B3 VP4 Non-Structural Functions

3.1 Introduction

Non-Poliovirus Enteroviruses (NPEVs) are emerging pathogens who have been shown to cause outbreaks that cause severe symptoms including, meningitis, encephalitis, and acute flacid paralysis[171]. Among the NPEVs are Coxsackieviruses (CVs) which have the potential to cause life-long illness including diabetes and cardiomyopathy[120, 216]. However, the number of antivirals available to CVs are limited[45]. To induce immune protection against CVs we can turn to the innate immune system, which can act against the early stages of infection[19]. CVs, like all NPEVs, has a rapid rate of adaptation due the RNA-dependent RNA-polymerase's (RdRp) error-prone replication which allows for a large pool of mutations after each replication cycle[65]. A small subset of these mutations may have beneficial fitness against detection and clearance from the innate immune system. As part of a larger team in the Andino lab, consisting of Orly Laufman, Yinghong Xiao, Eileen Foy, and Alisa Iakupova, we examined mutations in CV strain B3 (CVB3) that arise after selection against passaging CVB3 in cells with increased levels of interferon (IFN) type I (**Figure 2.1A**). From the trajectories of mutation frequencies using Circular Sequencing (CirSeq)[9] a subset of accumulated mutations was determined (**Figure 3.1.B**). Of these mutations the strongest resistance to IFN was determined to arise from a mutation in protein VP4, a protein thought only to have structural functions. VP4 is found in Enterovirus capsids in the interior interface between the capsid proteins and the packaged positive sense single-stranded RNA (+ssRNA).

Several of the mutations identified from the passages were lysine to arginine mutations. This is of interest as lysines are known to be targeted by the ubiquitination pathway in disordered proteins. VP4 is an intrinsically disordered protein due to its structurally-resolved state sandwiched between capsid proteins VP1, VP2, and VP3 and the packaged +ssRNA genome. VP4 is also known to be expelled from the capsid during the genome uncoating process, being released after the externalization of the pocket factor. This conserved process found in Enterovirus genome release is poorly understood, with the current model believing VP4 to form a 'tunnel' in the endosome through which the genome can pass. In the work

of this chapter the non-structural function of VP4 is probed through a charge-conserving mutation.
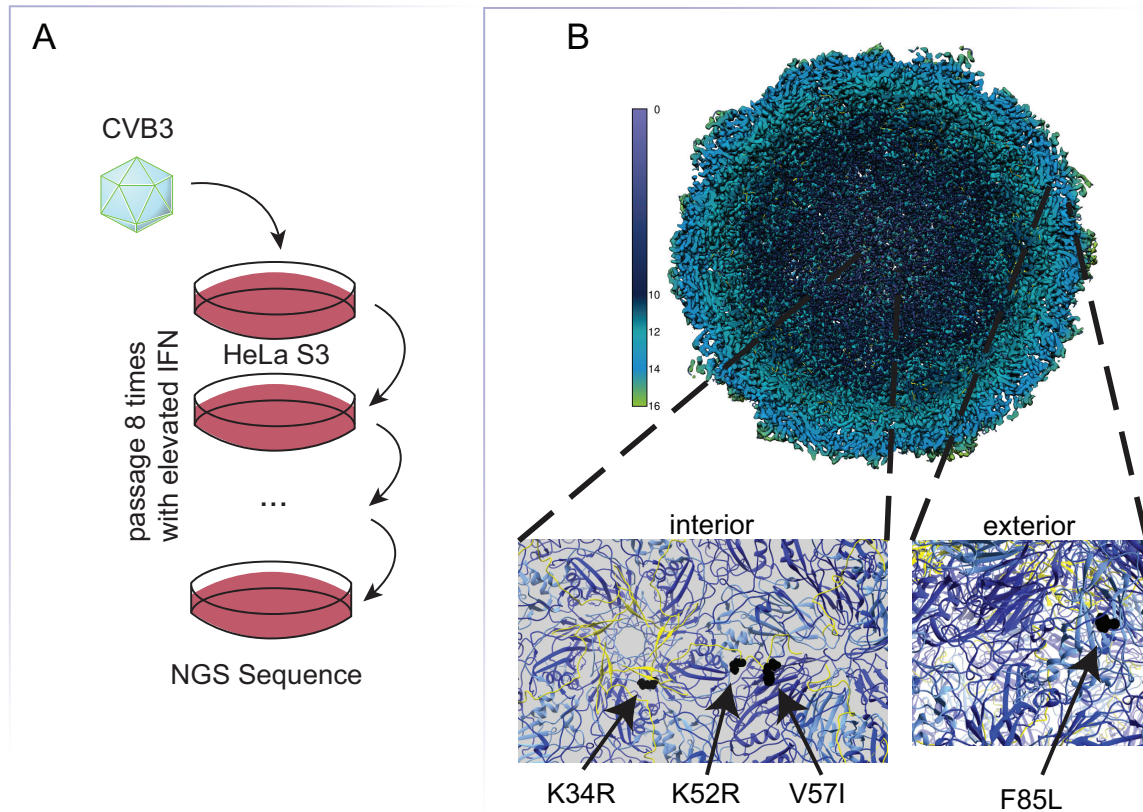
Figure 3.1: Isolation of Innate Immune Response Evading Mutations
A) CVB3 was passaged 7 times under elevated IFN β levels to select for mutations associated with innate immune response. Next Generation Sequencing (NGS) was performed over the passages to identify mutations **B)** Structural mutations were identified in VP4 (K34R, K52R, and V57I) and VP3 (F85L) that increase replication under IFN expressing cells

3.2 Results

3.2.1 Enhanced Cell Entry of Mutant # 6

To assay if the initial stages of replication for CVB3 was affected by this mutation lysine to arginine at position 34 in VP4 (# 6) we first looked at the replication dynamics in a one-step growth curve. Briefly, $1x10^8$ PFUs were inoculated onto $1x10^7$ HeLa S3 cells in 6-well plates, allowed to attach but not start the cell entry process by leaving the plates at 4°C for 30 minutes before aspirating the inoculum and returning the plates to a 37°C

incubator. At each time point a plate was transferred to a -80° C refrigerator to halt the replication cycle. Supernatant from each time-point was then titered by plaque assay. The resulting growth (Figure 3.2A) curve contrasts the WT sample to mutant # 6, showing that late time points in the replication cycle are similar while early time points differ by about five times. This indicates that this mutation has some affect at early time points of the replication cycle, the eclipse phase. In this phase of replication, the +ssRNA genome is released from the capsid, and the first polyprotein is translated followed by +ssRNA genome replication by the RdRp. This is an especially vulnerable stage of replication, as recognition and restriction of the single genome by the innate immune system prematurely ends replication. Fewer particles detected in the first four hours of the replication cycle could indicate a more efficient genome release process, as infectious particles detected before the exponential phase (4-8 hours post infection) are mostly particles from the initial inoculation that did not release their genome and become non-infectious. To test this hypothesis, the uncoating process was examined outside of cell entry process.

The rate of entry into susceptible HeLa S3 cells was determined by neutral red assay. Both WT and # 6 CVB3 were grown in the presence of the compound Neutral Red, where the incorporation of this small molecule into the packaged +ssRNA genome confired light sensitivity (**Supplementary Figure 3.1**). Equal titers of WT and # 6 CVB3 were added onto monolayers of confluent HeLa S3 cells in the absence of broad-spectrum light and allowed to attach but not initiate infection at 4°C. The virus and cell monolayer were then transferred to a 37°C incubator to initiate infection. Time points were taken by exposure of the plates to broad-spectrum light and then immediately returned to the incubator, allowing for the inactivation of only still encapsulated genomes. One round of replication was allowed to take place for 8 hours after the last time point. Each time point was titered by plaque assay and compared to an unexposed control sample (**Figure 3.2.B**). Over the 2 hour entry period it appears that # 6 releases the +ssRNA genome at a faster rate than the WT in the cell. This may be due to # 6 having a stronger ability to protect it's genome at early stages of the
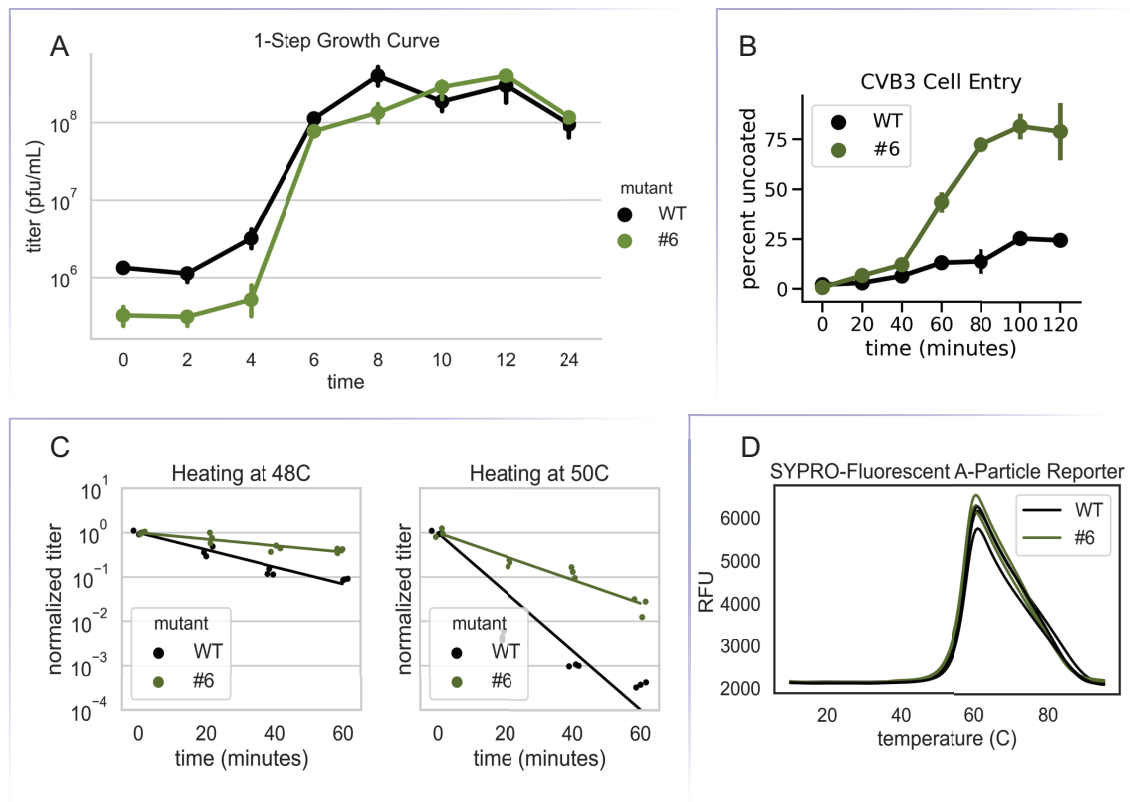
Figure 3.2: Analysis of VP4 Mutation # 6
A) One-step growth curve of mutation # 6 vs WT CVB3 in HeLa S3 cells **B)** Kinetics of cell entry of mutation # 6 vs WT CVB3 during the first 2 hours of replication, assayed by Neutral Red assay **C)** Thermostability of WT and mutation # 6 CVB3, looking at kinetics of inactivation by heating at increasing time points **D)** Measurement of A-particle formation during gradual heating of the purified capsid particles

replication cycle. However, the enhanced entry may also be due to reduced thermostability, which was demonstrated in the previous chapter to have a negative correlation with entry. To rule out reduced thermostability as the cause of enhanced cell entry, the thermostability of the # 6 capsid particle was compared to WT capsid particle.

3.2.2 Thermostability of CVB3 Mutation # 6

Using elevated-temperature-mediated uncoating kinetics, the inactivation rates of WT and mutant # 6 CVB3 were determined. Using purified particles, the samples were heated at either 48°C or 50°C and titered every twenty minutes over an hour (**Figure 3.2.C**). Rates were mapped to both samples for both heating conditions. Interestingly, the # 6 mutation appeared to be more thermostable than WT at both 48°C and 50°C. This implies that the conformational change associated with loss of infectivity has a slower progression from the infectious native state to the non-infectious A-particle state. As the loss of infectivity is associated with the loss of both the hydrophobic pocket factor and VP4[139], it is implied that VP4 is retained with greater affinity in # 6 than in the WT capsid. This is contradicted by the previous data in **Figure 3.2.B**, where genome release is thought to occur earlier in the replication cycle as VP4 is lost from the capsid prior to genome release[168]. With the opposing data of thermostability and cell entry, fluorescent reporters for VP4 loss were used to determine if VP4 is lost at higher temperatures. Purified CVB3 WT and # 6 capsid particles were both gradually heated using the previously described method of PaSTRy[195]. This method allows for the detection of the hydrophobic residues of the VP1 N-terminus and VP4, which have been shown to be released during the inactivation by heating prior to genome release. Measuring fluorescent units for both WT and # 6 during gradual heating the relative amount of VP4 loss was observed (**Figure 3.2.D**). Surprisingly, both fluorescent signals coincided, with half-maximum values around 52°C, representing the halfway point of state transition from the native state to the A-particle state. This indicates that VP4 is not lost either faster or slower in the # 6 mutant and that the phenotype of enhanced entry is

not due to an altered structural ability of VP4. VP4 must then be playing a non-structural function in virus replication, which agrees with the original conditions of selection; mutations that overcome the innate immune response.

3.2.3   Specific Infectivity of CVB3 Mutation # 6

Purified capsid particles of both WT and mutant CVB3 were used to determine the number of physical particles required for one infectious unit. Particles were purified by sucrose cushion and sucrose gradient, where the fraction about midway through the 15-45% gradient was determined to have the highest concentration of infectious particles and had previously been identified to contain the enterovirus capsid in the native state. The number of infectious units was determined by plaque assay for both WT and mutant # 6 and the number of physical particles per μL were counted. A 50 nm latex bead standard of known concentration was used to calibrate the number of particles per μL. Dividing the number of physical particles per infectious units gives the specific infectivity, where the higher the specific infectivity the more particles that are required to initiate an infection (**Figure 3.3.A**). Mutation # 6 requires less than half of the particles of WT CVB3 to initiate a successful infection, reducing from 1143 ± 34 particles/infectious unit to 504 ± 65 particles/infectious unit. This stark difference was also found to be statistically significant, with p-value of 0.0002 by T-test. The reduction in the number of particles required to initiate an infection indicate that the mutation # 6 is more efficient at initiating infection, where VP4 is then thought to be playing a role in inhibiting the innate immune system's ability to halt early stages of the replication cycle. Visualizing the purified CVB3 capsid particles reveals an interesting change in morphology. The WT capsid particles appear as previously imaged Enterovirus capsids, where the capsid is nearly spherical with a radius of 30 nm (**Figure 3.3.B**). Capsids also appeared to clump together, with few capsids not touching at least one other capsid. Almost all capsids appear to have the +ssRNA genome still encapsulated, where the empty capsid appears without the genome density at the center of the particle. For purified
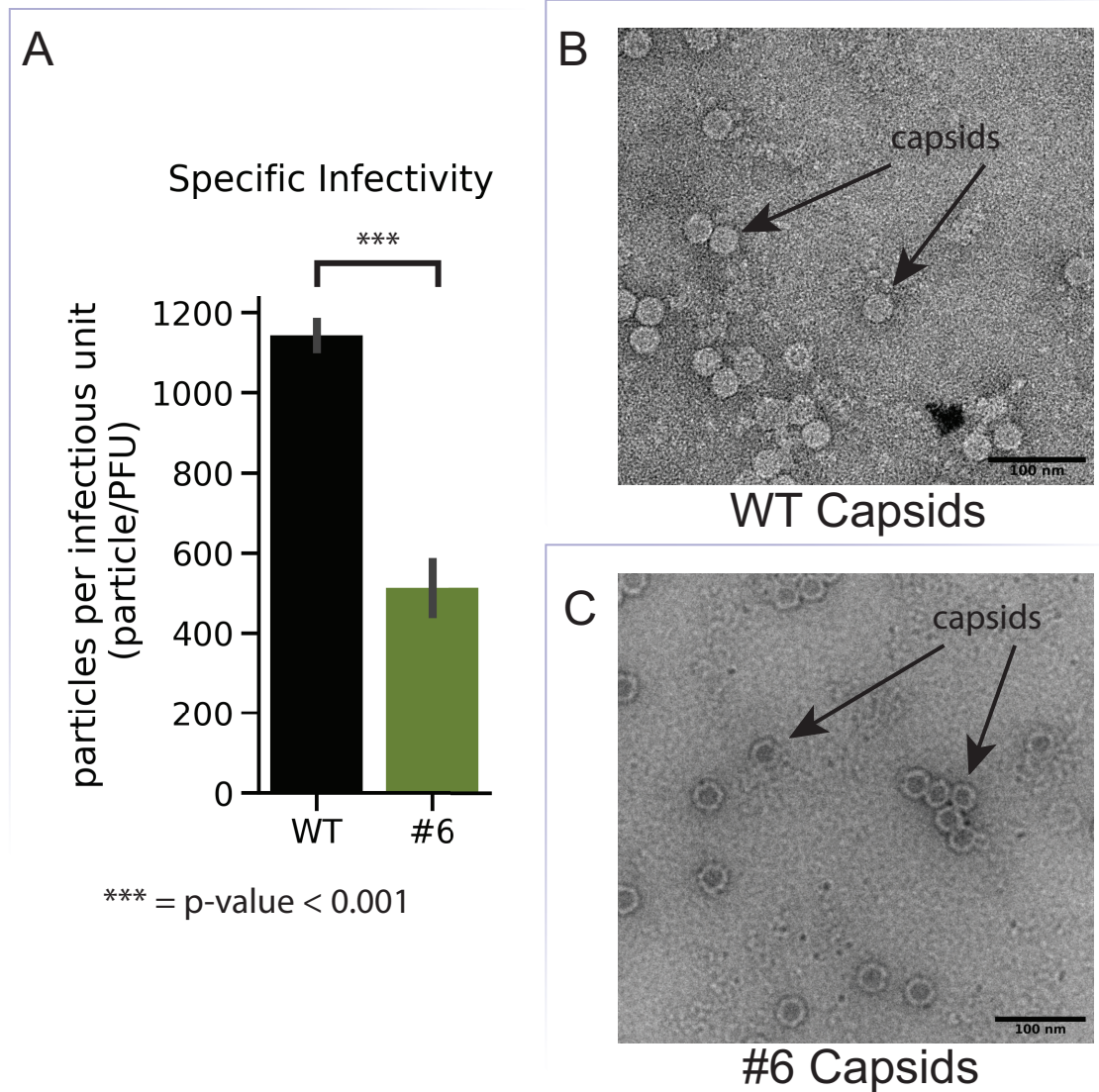
Figure 3.3: Infectious Ability of CVB3 WT and Mutant
A) Ratio of capsid particles per infectious unit (PFU) for mutation # 6 vs WT CVB3 **B)** Negative-stain EM image of WT CVB3 capsid particles, 100 nm scalebar **C)** Negative-stain EM image of mutation # 6 CVB3 capsid particles, 100 nm scalebar

capsids of mutant # 6 this empty capsid morphology was identified for nearly all particles (**Figure 3.3.C**). This is unexpected, but may be due to the method of staining the electron microscopy grid containing the purified capsids, as the genome is visualized nearby most of the capsids as long, coiled strands. This, coupled with the # 6 capsids displaying higher numbers of infectious titer indicate that these empty capsids may not be representative of the purified capsid. Further work may be required to further quantify the morphological changes this mutation induces of the infectious capsid.

3.3 Discussion

The function of the capsid protein VP4 has been an area of interest, with the functionality of the protein has been postulated to interact with capsid formation[111, 25] and facilitating genome release[33]. In this work I demonstrate that VP4 has another functionality, where interactions with the innate immune system are inferred by selection of VP4 mutations in a cell with enhanced levels of IFN β. The subsequent ruling out of structural functionality in state progression required by the genome uncoating process of CVB3 implies that VP4 must be playing a non-structural role in the early phases of replication, where both the number of replicated genomes and polyproteins have been shown to be at low levels[27]. The lower number of capsids required to initiate a successful infection by the introduction of the # 6 mutation indicates that VP4 plays a critical role in the establishment of viral replication. Taken together, it is inferred that VP4 is playing a non-structural role during the first few hours of the viral replication cycle by inhibiting the innate immune response. Previous work was done in the lab to both motivate and elucidate possible functionality of VP4. Not included in this chapter is previous work on cross-linked mass spectroscopy analysis of which cellular factors CVB3 proteins interact with. It was determined that proteins UBXN1 and VCP, which interact with the ubiquitin pathway[122] also interact with VP4. This work, taken with the data in this chapter, implies that VP4 may be interacting with the ubiquitina-

tion pathways to shutdown the misfolded protein response that can inhibit viral replication. VP4 may be released by the capsid during the cell entry process to competitively inhibit the viral protein-detecting side of the innate immune response. Further work must be done to determine the mechanism of VP4 inhibition of the innate immune response. As of writing this chapter work was being continued by Alisa Iakupova on the universality of VP4's ability to increase viral replication using a luciferase encoding poliovirus amplicon[208] to measure viral translation with or without increased levels of VP4. The ubiquitination pathway can also be explored by the addition of known compounds that affect the misfolded protein response, such as MG132. The non-structural functions of a structural protein emphasis how human-adapted pathogens, such as enteroviruses, have evolved encoded proteins that play multiple roles in maximizing the chance of viral replication. This higher level efficiency allows for a smaller genome that enables faster genome replication. Multifunctional proteins then can switch function based on environmental factors and allow for a dynamic infection that is turned to the slower-adapting host. It should be noted that not all Picornaviruses produce the protein VP4, despite high levels of genome identity, and the precursor protein remains uncleaved in the capsid protein. Investigations on how Picornaviruses replicate without the use of the VP4 protein may lead to further understanding of virus-host interactions.

3.4   Materials and Methods

3.4.1   Viral Production

Using cDNA from a plasmid carrying the full genome of CVB3 strain Nancy, the plasmid was linearized and used as a template for in vitro transcription (IVT) using the Promega Megascript T7 kit. 20 μg of IVT RNA was then electroporated into 4×10^6 HeLa S3 cells. Virus was allowed to replicate for 24 hours until visible cytopathic effect (CPE) was observed. Flasks of cell-virus mixture was then frozen and thawed three times at -80°C and room temperature (RT), respectively. Thawed media was then centrifuged at 3000xg for 5 minutes

to pellet cellular debris and supernatant was stored and titered for viral concentration. This was done for both WT and K34R # 6 mutant.

3.4.2 Plaque Assay

To assay the number of infectious CVB3 particles per sample, plaque assays were performed with HeLa S3 cells. Cells were prepared in 6-well plates the day prior at $5x10^5$ cells/well, resulting in a confluent monolayer of cells the day of plaque assay preparation. Viral sample was serially diluted ten-fold, eight times, in 5 mL tubes. The most diluted samples were used for plaque assay, using six dilutions per sample. Media was aspirated from each well immediately prior to added diluted samples to each well. 500 μL of diluted sample was added to each well, always to the side of the well, and immediately placed in a 37°C incubator. Virus was allowed to adhere and enter cells over one hour, with gentle rocking to evenly distribute virus every ten minutes. At one hour the plates were removed from the incubator and 47°C, 1% agarose-DMEM media was added to each well. Agarose-media mixture was allowed to cool and solidify in each well. Plates were transferred back to the 37°C incubator for 48 hours, where viral plaques grew until they were able to be visualized by eye. Each well was then fixed with 1% paraformaldehyde overnight, agarose-media plugs were removed from each well, and the monolayer of fixed cells were stained with 0.1% crystal violet for at least 1 hour. Excess crystal violet was removed by washing with diluted bleach and plates were allowed to dry. Plaques were then counted and multiplied by the well's dilution factor to get the number of plaque forming units (PFU) per mL.

3.4.3 Neutral Red Assay

Neutral Red virus were produced by inoculating HeLa cells with viral stock and allowing virus to attach and enter cells over 1 hour at 37°C. Inoculum was then removed and replaced with viral media containing 20 μM neutral red. Flasks of infected cells were wrapped in foil then returned to a 37°C incubator for 24 hours. Viral supernatant was obtained as

previously described and kept in darkness. During assaying Neutral Red virus was serially diluted and added to 6-well plates of 5x10^5 HeLa cells/well in 500 μL aliquots.

3.4.4 Virus Purification

CVB3 was propagated in 20 100 mm dishes of confluent HeLa cells. Upon total CPE, virus particles were lysed with 0.5% IGEPAL CA-630 and followed by three cycles of freeze-thaw. Resulting supernatant was then centrifuged for 5 minutes at 3000xg to pellet cell debris and resulting supernatant was then precipitated with 8% final concentration PEG 8000 at 4oC for 72 hours. Virus was pelleted at 3000xg for 1 hour, re-suspended in purification buffer (100 mM NaCl, 200 mM NaAc, 10 mM Tris) and remaining debris pelleted at 3000xg for 15 minutes. Supernatant was then purified through a 30% sucrose cushion centrifuged at 100,000xg for 3 hours followed by fractionation by 15-45% sucrose gradient at 100,000xg for 3 hours. Fractions were then dialyzed by Zeba desalting column and concentrated using a Amicon 100,000 MWCO filter.

3.4.5 Viral particle quantification

Known titers of purified mature viral particles were mixed with known concentrations of 50 nm latex beads. Samples were then imaged by negative-stain electron microscopy. Electron micrographs were then used to determine the ratio of viral particles to latex beads and calculate the concentration of viral particles. Ratios of viral particle concentrations and titer were used to determine viral particle to infectious unit ratios.

3.4.6 Thermostability Assay

Purified virus samples were heated using calibrated water heat bathes set for indicated temperatures. Samples were added to the heat bath simultaneously and removed at indicated time points and placed on ice for at least 5 minutes. Samples were then titered by plaque

assay.

3.4.7   Particle Stability Thermo Release Assay

Particle Stability Thermo Release assay (PaSTRy) was performed as previously described [citation needed]. Briefly, purified particles were aliquoted in qPCR tubes with either SYPRO orange, to measure the level of protein unfolding as a proxy for A-particle formation, and SYTO9, a RNA-sensitive dye that reports the release of viral RNA. Samples were gradually heated in a BioRad CFX Connect thermocycler between 4°C and 95°C, relative fluorescent units (RFUs) were taken every 0.5°C.

3.4.8   Negative Stain Electron Microscopy

Negative stain electron microscopy was performed after fixation of purified particle with 0.01% final concentration EM-grade paraformaldehyde. Quantifoil 400 mesh formar copper grids were glow discharged prior to the addition of sample to the gird. Samples were allowed to adhere to grids for 5 minutes followed by wicking away of excess liquid by applying a whatman paper to the edge of the grid. Grids were then washed with deionized distilled H2O and excess liquid wicked before applying 2% neutral phosphotungstic acid for 30 seconds. Excess liquid was wicked away and grids were imaged with a FEI Tecnai T12 120 kV microscope with a Gatan UltraScan 895 4k CCD camera. Images were intensity-adjusted for viewing clarity with ImageJ.

3.5 Supplementary Materials
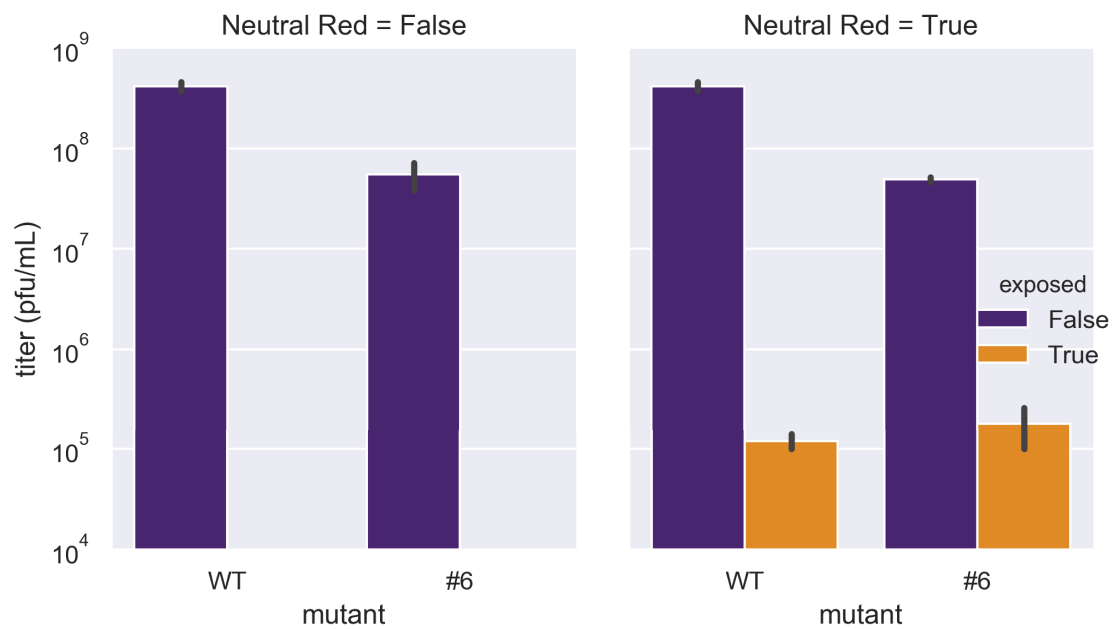
Figure 3.4: Validation of Neutral Red Assay
Neutral Red incorporated particles were validated for being inactivated by broad-spectrum light by titering samples before and after exposure to 15 minutes of light. Samples were then titered by plaque assay in darkness.

Chapter 4

Poliovirus Type 1 Thermostability

4.1 Abstract

This chapter represents my work with a well-known virus, Poliovirus. It also represents another link in the chain of Poliovirus research stretching from myself to my Ph.D. advisor Raul Andino, to his Postdoctoral advisor David Baltimore [21], to his Postdoctoral advisor Renato Dulbecco [53]. This is also the first virus I worked on in the Andino lab, using the strain embed in an infectious clone plasmid by Vincent Racaniello [148]. Much of this work was fueled by enormous mentorship and collaboration with researchers inside and outside the lab, including (but not comprehensively), Ming Te Yeh, Yinghong Xiao, Weiyi Li (now at Stanford), Elsa Rousseau (formerly at IBM), Yuta Shirogane, Gilad Doitsh (now at Vaxart Inc.), Ranen Aviner, Orly Laufman (now at the Weizmann Institute), Weiheng Su (now at Jilin University), Zachary Whitfield (now at Rancho Biosciences), Mariana Tioni (now at Meissa Therapeutics), Colby Gekko (now at Cornell), Dale Talbot, Arabinda Nayak (now at Gilead), and Simone Bianco (now at Altos Labs). My introduction to Poliovirus was through the Defense Advanced Research Projects Agency (DARPA) INTERfering and Co-Evolving Prevention and Therapy (INTERCEPT) program. The combination of the Andino lab, as well as labs at IBM, the Weizmann, Aleph Therapeutics, and Pine.Bio led to one of the best collaborative research project experiences and at least 2 papers to date [161, 208]. While I made contributions to the previous two papers, this chapter discusses a tangential project of mine that relates to the previous two chapters regarding thermostability of the viral capsid. This work was motivated by issues that were ran into during the INTERCEPT program regarding reduced infectivity in the primary product being developed, the engineered enterovirus therapeutic interfering particle (eTIP). This eTIP has been documented to be effective in preventing disease caused by Poliovirus and is still an area of active research in the lab. This work was also motivated by collaboration between myself and LaNell Williams at Harvard, a collaboration initiated and facilitated by Simone Bianco when he was at IBM. This work was aided by a summer intern in the Andino lab, Simone Parker, who will be attending Loyola University, who I had the pleasure of advising.

4.2 Introduction

Poliovirus (PV) outbreaks are as old as human history, with descriptions of outbreaks dating as far back as ancient Egyptian hieroglyphics. The efforts by the World Health Organization (WHO) to eradicate wild PV from the human race has largely been a successful one with all but two countries still suffering from circulating PV. However, setbacks have been suffered during this effort with the recent outbreak of wild PV type 1 (wPV1) in Malawi [2]. This recent outbreak, which undid 5 years of the continent of Africa not experiencing an outbreak of wPV1, is accompanied by the growing number of circulating vaccine-derived PV type 2 (cVDPV2) [1], which has grown from only 2 reported cases in 2016 to 1074 cases as of October 2021. The recent re-emergence of PV underlines the continued research for the molecular mechanisms of PV, as well as possible tools to improve PV vaccines. Recent work in the lab has demonstrated that basic science research on PV can drive the development of novel PV vaccines, with the novel oral PV vaccine type 2 (nOPV2)[212] developed in the Andino lab recently acquiring emergency use listing and administered in 125 million individuals as of October 2021 [1]. Future development of vaccines and therapeutics for PV, as well as other enteroviruses, requires a deep understanding of viral pathogenesis [147, 165]. A critical step of PV pathogenesis is capsid integrity between infection cycles and the ability to enter susceptible cells. Indeed, it has been observed that between the release of the positive-sense, single-stranded RNA (+ssRNA) genome and the replication of the first copy of the enterovirus polyprotein is when replication inhibition by interferron type I is most effective [27]. Targeting this vunerable stage in replication is difficult, as the handful of viral molecules that act at this stage have evolved to avoid detection. This can be overcome through genetic adaptation studies, where the epitopes that interact with the phenotype of interest are forced to overcome some desired selection. Increasing the stability of the infectious particle of PV, the capsid, can give insight on how PV effectively releases the +ssRNA genome into a susceptible cell. It has been established that the capsid must undergo state transitions to release the genome, first converting into into the so-called altered particle (A-particle),

by the loss of the embed hydrophobic lipid molecule, known as the pocket factor, and the short, intrinsically disordered capsid protein VP4[84] . This conversion can be accelerated by heating or by interaction with the poliovirus receptor (PVR)[146, 28]. Increasing the thermostability then should decrease virus's ability to release the +ssRNA genome into cells. This form of attenuation may be useful for developing future vaccines and better understanding the cell entry process. Thermostability can be manipulated by changing select amino acids in the capsid to increase stability or by altering the way the genome interacts with the capsid. Known enterovirus genomes tend to be around 7.5 kilobases in length. Indeed, the genome appears to be optimized in length to fit inside the capsid, where the density of nucleotide per volume is that of crystalized RNA (1 nucleotide / $\mathring{A}^3$). Defective genomes have been known about since the 1970s [39] and their truncated size may have affects on how the capsid releases the genome. Furthermore, defective interfering particles have recently been observed to have deterimental effects on the viral population from which they arise [175] and are of active interest as possible antiviral therapeutics[161, 208]. Better understanding how a truncated genome affects cell entry may aid in defective interfering genome engineering.

4.3 Results

4.3.1 Thermostable mutations

Four thermostability-affecting mutations in the protein VP1 of the PV1 capsid that were previously described were reverse-mutated in an infectious clone of the Mahoney strain of PV1[10]. These mutations include alanine to threonine at position 26 (A1026T, in orange), valine to alanine at position 87 (V1087A, in green), valine to isoleucine at position 160 (V1160I, in purple) and isoleucine to valine at position 194 (I1194V, in brown) (**Figure 4.1.A**). Mutations are structurally indicated on PV1 capsid structure 2PLV[79]. All mutations give rise to small changes in the hydrophobic side-chain composition, with no net

charge change or change in hydrophobicity. Additionally, a combination of mutations V1160I and I1194V was also introduced into the WT infectious clone, resulting in the double-mutant V1087A+I1194V. This double-mutant was created as I1194V was reported to induce thermolability instead of increasing thermostability of the capsid, as well the single mutation V1087A was reported to be non-viable. As I1194V and V1087A were found in the hydrophobic core of the β-barrel, the synergistic effects of pocket factor interactions can be weighed by comparing the combined effects of the opposing mutations and their individual contributions.

4.3.2   Cooperative effects

First, the thermostability effects of each mutation were measured. As the individual mutations were not quantified in the original paper, these values were not known. Each WT and mutant PV1 capsid population was subjected to heating at 48°C for 0-60 minutes, with measurements taken every 30 minutes. Titers of viable virus was then measured by plaque assay (**Figure 4.1.B**). From each mutant's rate of inactivation rates were measured (**Table 3.1**). All rates of inactivation were severely slowed, thereby increasing thermostability, except for mutation I1194V, as expected. However, the combination of I1194V and V1087A barely lowered the rate of inactivation of V1087A by itself. The valine to alanine mutation, a shortening of the side chain by two methyl groups, has a stronger affect on inducing thermostability than adding one linking carbon on a methyl group of the isoleucine to leucine mutation. This suggests that minimizing the surface area of the side chain in the hydrophobic pocket stabilizes the pocket factor and prevents the transition to the non-infectious A-particle.

To better understand the transition of native state to A-particle and the rough nature of the mutations, a deeper probe into the state transition of WT PV1 and mutants by previously discussed method, PaSTRy. Briefly, each purified population of PV1 capsids was gradually heated in the presence of a dye that fluoresces when exposed to hydrophobic amino acids. As the loss of the pocket factor and the hydrophobic VP4 indicate the transition
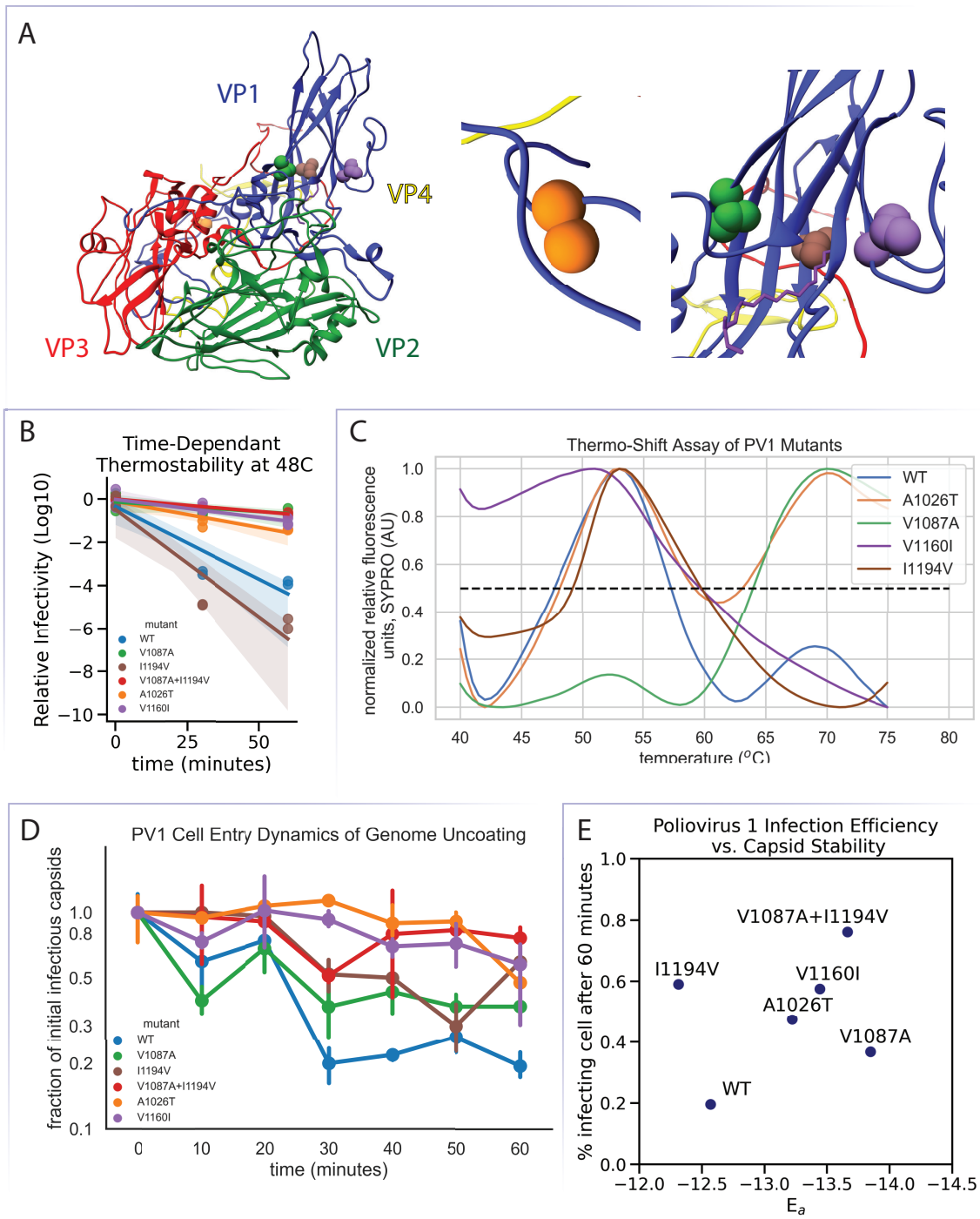
Figure 4.1: Poliovirus Thermostability and Cell Entry

Table 4.1: Rate of Inactivation, k_f ($10^{-3} min^{-1}$)

Strain	48°C
WT	68±12
A1026T	24±4.2
V1087A	9.0±5.0
I1160V	16±4.1
V1194V	100±16
V1087A + I1194V	12±1.0

from the native to the A-particle, the fluorescent readout reports for the fraction of the population in the A-particle state (**Figure 4.1.C**). The WT population transitioned to 50% A-particle around 47°C and particles began completely unfolding around 70°C, which agrees with previously published values[10]. Also of note is mutation A1026T, the weakest of the identified thermostabilizing mutations, barely moved the 50% A-particle temperature point, reinforcing its minimal effect on thermostability. Interestingly, the V1087A fluorescence curve showed that less than 20% of the native particles transitioned to the A-particle state at the 45-55°C range, but all capsids degraded at the expected second fluorescence peak of 70°C, indicating that only a sub-population of V1087A capsids can progress to the canonical A-particle state. The thermolabile mutation I1194V actually increased the 50% A-particle temperature point, increasing by about 2°C from the WT. This was accompanied by a fluorescence signal that remained higher than other mutants, indicating that the native state may not have completely formed viable particles that minimize the surface-exposed hydrophobic residues. All of these associated changes to the mutations in question may also affect the cell entry process.

4.3.3   Entry and thermostability

To assay if thermostability of the indicated mutations had a corresponding decrease in the ability to enter susceptible cells, a neutral red assay was performed to determine the fraction of infectious particles that had released their genomes over a 1 hour time period. As

previously described, WT or mutant viruses were grown in the presence of the compound Neutral Red to induce inactivation when viral capsids are exposed to broad-spectrum light. Over the 1 hour time period the fraction of still infectious particles decreased, with the WT uncoating the most efficiently at 20% of the genomes not uncoated and the double mutant V1087A+I1194V the least efficient with 78% of genomes still encapsulated (**Figure 4.1.D**). All but 2 of the mutants matched the general trajectory shape of WT with a large genome release event between 20 and 30 minutes, with A1026T and V1160I both only moderately increasing in the fraction of uncoated capsids. Indeed, most of the mutants only moderately release their genomes over time, with V1087A having the most similar genome release trajectory when compared to the WT. This is unexpected, as V1087A has the highest thermostability of mutants examined. To truly compare cell entry and thermostability, the energy of inactivation and the final fraction of uninfected were plotted together. To determine the energy of thermostability, the activation energy of native to A-particle state transition was calculated by the Eyring equation: $E_a = RTln\left(\frac{hk_f}{RT}\right)$. Where R is the ideal gas constant, T is the temperature of the system in Kelvin, h is Planck's constant, and k_f is the rate of inactivation. The activation energy of WT was found to be -12.5 kcal/mol, while the most thermostable mutant V1087A was found to be -13.85 kcal/mol and the least thermostable mutant I1194V was found to be -12.3 kcal/mol. In agreement with the conjecture that thermostability reduces cell entry efficiency, there is a general trend of greater E_a resulting in lower final number of uncoated capsids. However, both mutations V1087A and I1194V deviate from this trend while the combination of mutations obeys this trend. The ability for the most thermostable mutant V1087A to also have the closest cell entry efficiency raises the question of why the effectively attenuated mutation I1194V is required for successful replication of the V1087A mutant. This points to the original paper's finding that V1087A was a low viability virus until the introduction of I1194V, this may be due to an equilibrium between cell entry and thermostability fitness. It may also point to other roles that the capsid proteins play, as was illustrated in chapter 2. The cell assembly phenotype

was not addressed in this study and may clarify other roles that the I1194V mutation is playing.

4.3.4   Enterovirus Therapeutic Interferring Particles

When analyzing the thermostability and cell entry of the PV1 capsid, a large focus has been given to the capsid proteins and how mutations and small molecules alter modes of genome release [43, 61, 203] , yet not as much attention has been directed to the RNA genome that the capsid functions to protect and release. The first infecting +ssRNA genome plays a critcal role in the infection process, indeed, the first uncoated strand of viral RNA is the seed from which the replication cycle grows. Therapeutics have targeted the replication of the +ssRNA genome [45] with mixed success [189], but the elusive target of the initial genome is harder to target due to it's short lifespan and difficulty of detection for even the infected cells [27]. Modifying both the size and the proteins expressed by the PV1 genome may also affect the primary functions of the capsid. The lab has produced an engineered, enterovirus defective interfering particle (eTIP1), where the structural-protein-encoding P1 region of the genome has been replaced with the fluorescing GFP-like protein mVenus (**Figure 4.2.A**). This eTIP has been demonstrated to not only replicate similarly to WT PV1 but also has the ability to reduce the replication of WT PV1 during co-infection [161]. When cells are dually-infected, both PV1 and eTIP1 genomes replicate slower during the last 2 hours of the replication cycle, yet eTIP1's efficiency of packaging into infectious capsids is increased while reducing the number of infectious WT PV1 particles by 3 orders of magnitude. This indicates that the defective genome, while lacking capsid proteins of its own to produced infectious particles, can utilize co-expressed capsid proteins to form infectious capsids. This information was used by Yuta Shirogane in the lab to produce a packaging cell line that expressed PV1 capsid proteins, allowing for the production of eTIP infectious particles (see methods). To assay the differences in particle morphology, both WT PV1 and eTIP1 particles were grown in 500 mL volumes and purified for electron microscopy
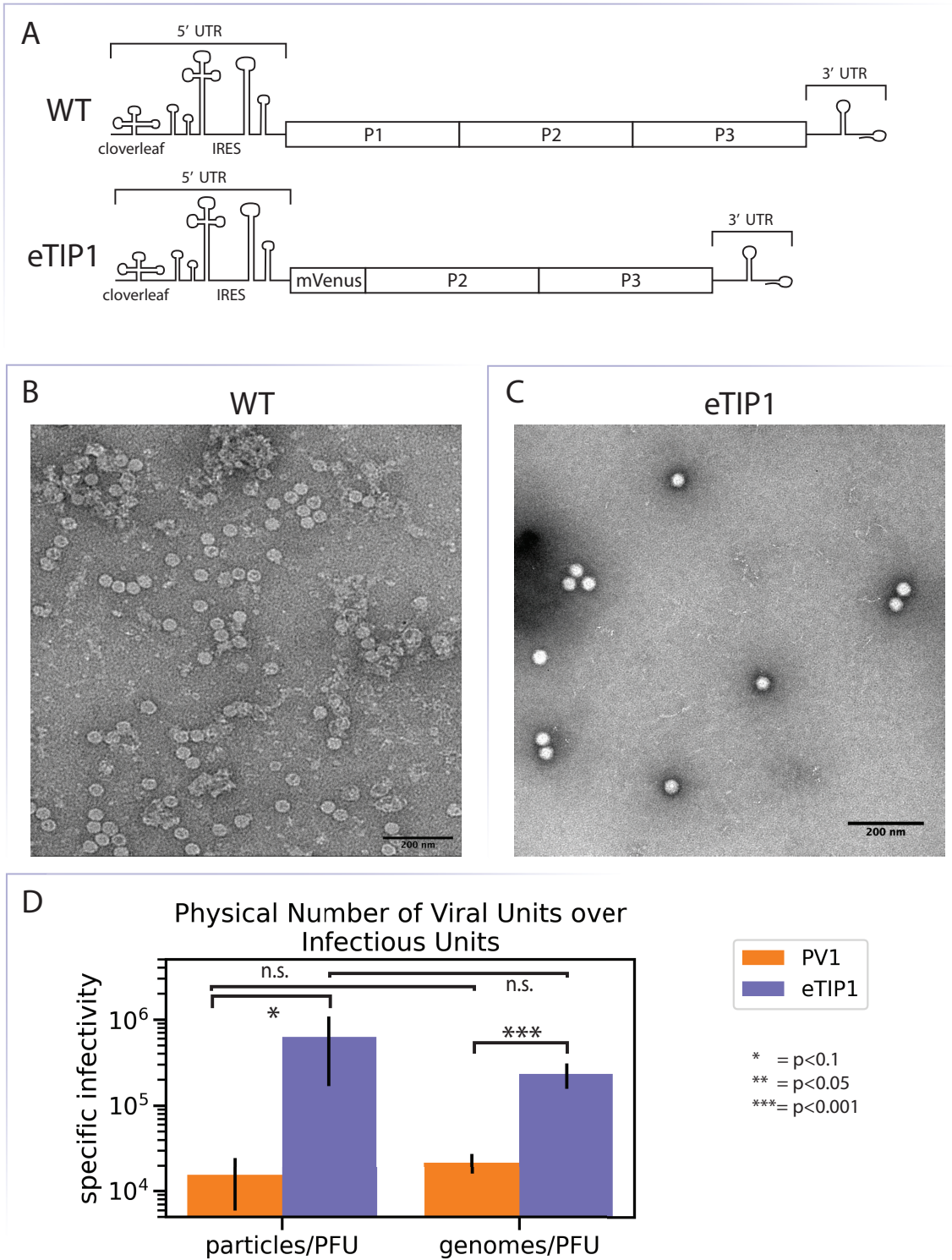
Figure 4.2: Defective Genome Size Reduces Replication Ability

(EM). As both PV1 and eTIP1 produce infectious particles, the same protocol for particle purification was used for both samples (see methods). The fraction expressing the highest concentration of infectious particles, as measured by either plaque assay for PV1 or number of green-fluorescing cells for eTIP1, also known as a focus-forming assay (FFA), was then visualized by negative stain EM. WT particles appeared as previously reported in previous chapters, as all enterovirus capsids, as somewhat-spherical and 30 nm in diameter (**Figure 4.2.B**). WT PV1 capsids were highly abundant in each micrograph, with some 1 μmxμm micrographs having more than 200 particles. On the other hand, eTIP1 particles were in low abundance in each image, with no more than 20 particles per μmxμm micrograph (**Figure 4.2.C**). The same morphology of WT PV1 was observed, but more detailed differences that occur with the smaller genome may be present. These differences would require at least the level of cryogenic EM and a much higher concentration of particles.

4.3.5   Genome size on specific infectivity

As eTIP1 capsid production is limited by the current packaging cell line system, further investigation was made into whether the lower number of infectious particles affected the virus's ability to infect cells. Work had previously shown that eTIP1s produced ¿3 orders of magnitude less infectious particles than PV1 after one replication cycle. Using electron microscopy, RT-qPCR, plaque assays, and FFA, the ratio of physical particles per infectious unit and genomes per infectious unit were calculated (**Figure 3.2.D**). Large differences were observed between the number of physical particles or genomes required to start a successful infection, with around 1.5 orders of magnitude more eTIP1 particles required than PV1 particles. Physical particles per infectious unit were calculated by EM, measuring the number of purified particles compared to a known concentration of 50 nm latex beads, and comparing the number of physical particles titers of plaque assay (PV1) or FFA (eTIP1). Genomes per infectious unit were calculated by measuring the number of genomes by RT-qPCR, against a known +ssRNA genome standard, over titers of plaque assay (PV1) or

FFA (eTIP1). The ratios mostly agreed, with any differences between particle/PFU and genomes/PFU ratios not statistically differing for either PV1 or eTIP1 (**Table 4.2**). This indicates that both ratios give results for measuring specific infectivity. This was validated by finding statistical significance comparing PV1 and eTIP1 for the number of particles required for infection and the number of genomes required for infection. As replication ability is not notably reduced[161], eTIP1 can then be said to be less efficient at initiating infection when packaged in the same capsid as WT PV1.

Table 4.2: Osmotic and Temperature Affects on Viral Viability

	particles/PFU	genomes/PFU
WT	1.5 ± 0.94x10^4	2.2 ± 0.59x10^4
eTIP1	6.3 ± 4.6x10^5	2.3 ± 0.76x10^5

Table 4.3: Specific Infectivity of PV1 and eTIP1)

4.3.6   Smaller genome size removes affect of osmotic pressure

The only noticeable difference between the eTIP1 and WT PV1 particles is the truncated genome, which is   2/3 the size of the WT PV1 genome. The attenuation in cell entry must then be due to how the packaged genome interacts with the capsid. As the size of the capsid remains the same, it is inferred that the volume does as well, and that the density of the packaged genome is decreased by   1/3. As the +ssRNA genome is positively charged, with each nucleotide contributing one negative charge, the charge density is decreased. These negative charges are thought to be balanced by cations incorporated in the packaging process, and it has been observed that the PV1 capsid can allow water molecules to permeate [14]. Therefore, increasing the osmotic pressure should differentially affect eTIP1 and WT PV1 capsids. Osmotic pressure was varied by the addition of sucrose, a known osmolyte, in the presence of purified eTIP1 and PV1 capsids. The samples were also heated for 30 minutes at 48°C to destabilize the capsids. Titers of viable virus was then measured by FFA for eTIP1 (**Figure 4.3.A**) and plaque assay for PV1 (**Figure 4.3.B**). Interestingly, eTIP1 did not
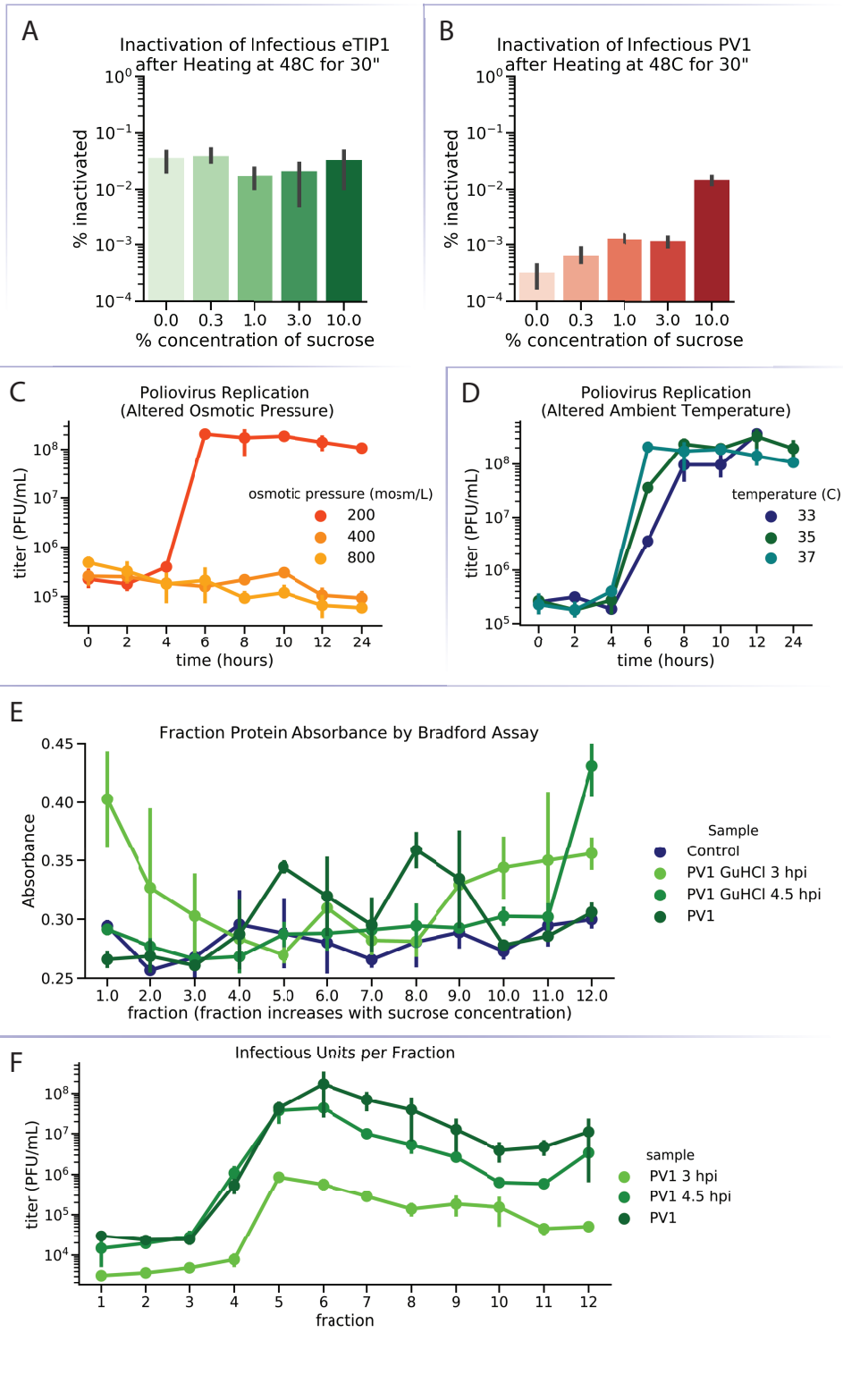
Figure 4.3: Thermostability and Osmotic Stabilty of Truncated Genome

show sensitivity to increasing osmotic pressure over 2 order of osmotic pressure magnitude. This may be due to such low levels of pressure exerted on the capsid by the packaged +ssRNA genome that environmental osmotic pressure is no longer balancing the outward pressure. This relationship of osmotic pressure and capsid viability is found with the WT PV1, where increased osmotic pressure protects the capsid from genome release, where 30% sucrose has 2-order of magnitude protective effect compared to no sucrose. As well, while PV1 titers are reduced more than 3 orders of magnitude when heated, eTIP1 titers are only reduced by about 1.5 orders of magnitude. This is unexpected, with eTIP1 capsids being more thermostable by only reducing the size of the genome. This contributes to the overall thesis, where increased enterovirus capsid thermostability comes at a cost of cell entry efficiency, in this case due to genome modifications rather than mutations encoded in the capsid.

4.3.7   Temperature and osmotic affects on replication

Both osmotic pressure and temperature have an affect on the capsid outside of a host cell. Susceptibility of enterovirus replication to these two factors was tested with WT PV1 in the prototypical HeLa S3 host cell. Osmotic pressure was increased, after HeLa S3 cells were incubated with infectious PV1 capsids, by adding NaCl to the cell media (DMEM + 2% FBS). Strikingly, replication was halted by increasing the osmotic pressure from the baseline 200 mosm/mL to 400 mosm/mL (**Figure 4.3.C**). This was despite no noticeable difference in cell viability when media osmolarity was increased. This indicates that replication is tied with osmotic pressure, although more work is needed to determine what aspect of viral replication is affected. Replication dependence on physiological temperature was measured by lowering temperature of the incubator PV1 was replicating in. Final titers were barely altered by changing the environmental temperature, with the only noticeable affect at the exponential growth phase (**Figure 4.3.D**). The rate of infectious particle formation is slowed between time 4-8 hours post infection. This is most likely due to enzymatic activity of the RNA-dependent RNA-polymerase being correlated with temperature [158]. This has

been observed with other enteroviruses, where the temperature of most efficient replication being closely tied to the physiological temperature of the host organ in which the virus infects. To finally determine if viral capsid packaging occurs at a precise time in replication, Guandinium Hydrochloride (GuHCl), known for inhibiting viral genome reproduction, was added before and during the exponential phase. By inhibiting genome replication capsid protein synthesis was not affected while the +ssRNA packaged within viable capsids was. Replication was allowed to proceed for 12 hours before cell lysate was purified as previously described. Lysate was subjected to sucrose gradient and fractions were measured for protein content (**Figure 4.3.E**) and infectious titer (**Figure 4.3.F**). The addition of GuHCl during to the exponential phase reduced the peaks of virus samples in fractions that contain native, infectious particles while the addition of GuHCl before the exponential phase enriched for low density fractions that contain empty capsids and individual capsomers. The addition of GuHCl prior to replication drastically reduced the infectious titers for all fractions, while the addition of GuHCl during the replication cycle only reduced the infectious titer by about half an order of magnitude for the least-dense fractions. This indicates that genome replication occurs primarily between 3-4.5 hours post infection, while protein translation is not majorly altered. This agrees with previous experiments [21]. This also indicates that the lowered density fractions of the purified virus-infected cell lysate contains capsomeres that have not yet formed infectious particles.

4.4   Discussion

Cell entry is a critical step of viral replication. In this chapter, it has been demonstrated that thermostability, of both the viral capsid and the interaction between the viral genome and the capsid, comes at the cost of efficient cell entry. This is useful for future studies for developing vaccines that can exist at room temperature for longer[74, 152, 176] and for targeting the early stages of viral replication. Poliovirus, a prototypical non-enveloped +ssRNA

virus, is an excellent system to test and develop these approaches. The work done in the chapter, as well as within the Andino lab, give insights to combating Poliovirus outbreaks through the development of therapeutics and vaccines. A rough hierarchy of stabilizing mutations were found in the mutations examined, with the decreasing thermostable mutations following Threonine Alanine Valine Isoleucine. Stability was demonstrated to inversely correlate with cell infectivity, with single mutations in capsid proteins have several-fold increases in resistance to heating while reducing the number of capsids able to infect a cell from 80% to 20%. This points to the viral capsid being evolutionarily tuned for maximizing the number of capsids that survive outside of a host cell while maintaining the highest level of efficiency with regards to receptor-mediated genome release. Of note, even when thermostability was reduced by the introduction of mutation I1194V, cell entry efficiency was reduced by mutationally perturbing the capsid. This suggests that the PV capsid sequence is optimized for efficient receptor-mediated genome release, and that mutations move the capsid away from this equilibrium. Genome size also appears to by optimized for efficient cell entry, as replication of the viral genome is not affected by genome truncation by the engineered eTIP1, but eTIP1 increases the number of viral particles required to successfully initiate infection by about 2 orders of magnitude. This is echoed in both thermo- and osmo-stability of eTIP1 compared to WT PV1, where the eTIP1 capsid is less sensitive to heat and osmotic pressure. While osmotic pressure does play a role with regards to viral replication, there may be a connection between osmotic pressure due to the packaged +ss-RNA genome and a capsid's thermostability. Further work is necessary to better quantify this relationship between genome size, capsid stability, and osmotic pressure. Attempts to modify eTIP1 to either have larger or smaller genomes proved to be unfruitful, as transfection of altered genomes were not observed to express encoded mVenus green-fluorescence or provide the tell-tale sign of cell cytopathic effect. This again may be due to the link between genome size and virus replication viability. As well, attempts to synthesis capsid particles *in vitro* were unsuccessful by using purified unpackaged PV1 capsomers and both *IVT* or

cell-extracted viral RNA. This has been an issue in the field of mammalian viruses, and it is thought that complexity of mammalian viruses requires cellular factors and organelles to successfully replicate. Overall, the work in this chapter indicates that the PV1 capsid is a multi-functional, metastable, protein-RNA complex that has evolved to best protect and deliver the +ssRNA genome to susceptible cells. The connection between the role the +ssRNA genome plays, not just with viral replication, but with capsid structural integrity points to more connected evolutionary adaptation to human hosts. De-optimizing this interaction with vaccines and therapeutics gives hope for combating viral outbreaks of not only PV. Better understanding the modalities of cell entry of non-enveloped viruses also reveals insights on cellular processes such endocytosis and lysosome trafficing. It will also elucidate how oligomeric proteins like enteroviruses undergo coordinated, symmetric, state changes.

4.5   Materials and Methods

4.5.1   Viral Production

Using cDNA from a plasmid carrying the full genome of PV1 strain Mahoney [CITATION NEEDED, Racaniello], the plasmid was linearized and used as a template for in vitro transcription (IVT) using the Promega Megascript T7 kit. 20 μg of IVT RNA was then electroporated into 4x10^6 HeLa S3 cells. Virus was allowed to replicate for 24 hours until visible cytopathic effect (CPE) was observed. Flasks of cell-virus mixture was then frozen and thawed three times at -80°C and room temperature (RT), respectively. Thawed media was then centrifuged at 3000xg for 5 minutes to pellet cellular debris and supernatant was stored and titered for viral concentration. This was done for WT and the mutants of interest.

eTIPs were produced by transfecting the defective IVT RNA into the 'packaging cell line', which had been previously created by transfecting HeLa S3 cells with a plasmid encoding the P1 structural region of the PV1 genome. These packaging cell lines constitutively express the capsid proteins, although the capsid cannot be formed without the entire genome as the

viral protease 2C is required to process the P1 polyprotein to the capsid proteins VP1, VP2, VP3, and VP4.

Generation of mutant virus from cDNA   Using the previously mentioned infectious clone of PV1 strain Mahoney, the plasmid used a template for site-directed mutagenesis. Using overlapping primers with the indicated mutation for each site, a full sense and anti-sense copy of the genome was introduced. Enzyme DpnI was used to restrict the original plasmid and the remaining overlapping copies of the plasmid was transformed into competent E. coli cells. Colonies were picked, grown, and lysed to isolate plasmid. Sanger sequencing was performed to determine which colonies expressed plasmids with the mutation of interest which was propagated and used for virus generation. These plasmids was linearized and used as a template for *in vitro* transcription of single strand RNA (ssRNA). 20 μg of ssRNA was then transfected into 4×10^6 HeLa cells. Transfected ssRNA was allowed to replicate to produce viral particles.

4.5.2   Plaque Assay

To assay the number of infectious PV1 particles per sample, plaque assays were performed with HeLa S3 cells. Cells were prepared in 6-well plates the day prior at 5×10^5 cells/well, resulting in a confluent monolayer of cells the day of plaque assay preparation. Viral sample was serially diluted ten-fold, eight times, in 5 mL tubes. The most diluted samples were used for plaque assay, using six dilutions per sample. Media was aspirated from each well immediately prior to added diluted samples to each well. 500 μL of diluted sample was added to each well, always to the side of the well, and immediately placed in a 37°C incubator. Virus was allowed to adhere and enter cells over one hour, with gentle rocking to evenly distribute virus every ten minutes. At one hour the plates were removed from the incubator and 47°C, 1% agarose-DMEM media was added to each well. Agarose-media mixture was allowed to cool and solidify in each well. Plates were transferred back to the 37°C incubator

for 48 hours, where viral plaques grew until they were able to be visualized by eye. Each well was then fixed with 1% paraformaldehyde overnight, agarose-media plugs were removed from each well, and the monolayer of fixed cells were stained with 0.1% crystal violet for at least 1 hour. Excess crystal violet was removed by washing with diluted bleach and plates were allowed to dry. Plaques were then counted and multiplied by the well's dilution factor to get the number of plaque forming units (PFU) per mL.

4.5.3 Neutral Red Assay

Neutral Red virus were produced by inoculating HeLa cells with viral stock and allowing virus to attach and enter cells over 1 hour at 37°C. Inoculum was then removed and replaced with viral media containing 20 μM neutral red. Flasks of infected cells were wrapped in foil then returned to a 37°C incubator for 24 hours. Viral supernatant was obtained as previously described and kept in darkness. During assaying Neutral Red virus was serially diluted and added to 6-well plates of $5x10^5$ HeLa cells/well in 500 μL aliquots.

4.5.4 Virus Purification

PV1 was propagated in 20 100 mm dishes of confluent HeLa cells. Upon total CPE, virus particles were lysed with 0.5% IGEPAL CA-630 and followed by three cycles of freeze-thaw. Resulting supernatant was then centrifuged for 5 minutes at 3000xg to pellet cell debris and resulting supernatant was then precipitated with 8% final concentration PEG 8000 at 4oC for 72 hours. Virus was pelleted at 3000xg for 1 hour, re-suspended in purification buffer (100 mM NaCl, 200 mM NaAc, 10 mM Tris) and remaining debris pelleted at 3000xg for 15 minutes. Supernatant was then purified through a 30% sucrose cushion centrifuged at 100,000xg for 3 hours followed by fractionation by 15-45% sucrose gradient at 100,000xg for 3 hours. Fractions were then dialyzed by Zeba desalting column and concentrated using a Amicon 100,000 MWCO filter.

4.5.5 Viral particle quantification

Known titers of purified mature viral particles were mixed with known concentrations of 50 nm latex beads. Samples were then imaged by negative-stain electron microscopy. Electron micrographs were then used to determine the ratio of viral particles to latex beads and calculate the concentration of viral particles. Ratios of viral particle concentrations and titer were used to determine viral particle to infectious unit ratios.

4.5.6 Thermostability Assay

Purified virus samples were heated using calibrated water heat bathes set for indicated temperatures. Samples were added to the heat bath simultaneously and removed at indicated time points and placed on ice for at least 5 minutes. Samples were then titered by plaque assay.

4.5.7 Particle Stability Thermo Release Assay

Particle Stability Thermo Release assay (PaSTRy) was performed as previously described [citation needed]. Briefly, purified particles were aliquoted in qPCR tubes with either SYPRO orange, to measure the level of protein unfolding as a proxy for A-particle formation, and SYTO9, a RNA-sensitive dye that reports the release of viral RNA. Samples were gradually heated in a BioRad CFX Connect thermocycler between 4°C and 95°C, relative fluorescent units (RFUs) were taken every 0.5°C.

4.5.8 Negative Stain Electron Microscopy

Negative stain electron microscopy was performed after fixation of purified particle with 0.01% final concentration EM-grade paraformaldehyde. Quantifoil 400 mesh formar copper grids were glow discharged prior to the addition of sample to the gird. Samples were allowed to adhere to grids for 5 minutes followed by wicking away of excess liquid by applying a

whatman paper to the edge of the grid. Grids were then washed with deionized distilled H2O and excess liquid wicked before applying 2% neutral phosphotungstic acid for 30 seconds. Excess liquid was wicked away and grids were imaged with a FEI Tecnai T12 120 kV microscope with a Gatan UltraScan 895 4k CCD camera. Images were intensity-adjusted for viewing clarity with ImageJ.

Part II

Coronavirus Epidemiology

Chapter 5

Examining the interplay between face mask usage, asymptomatic transmission, and social distancing on the spread of COVID-19

5.1 Abstract

This work was spear-headed by myself with the expert guidance of Ming Te Yeh, a researcher in the lab, and Sara Capponi of IBM. Work on this project began in March 2020, with the conversation with Ming Te of how to prove the effectiveness of face-masks at the start of the COVID-19 Pandemic. All code, analysis, and the majority of the writing was done by myself with the advice of Sara and Ming Te. Both my advisor Raul Andino and Simone Bianco, formerly at IBM but now at Altos Labs, oversaw research and assisted with writing and editing the manuscript that was finally accepted by Scientific Reports in August 2021. This work was published with a open-access agreement and the Creative Commons license, which authorizes reproduction of this work provided proper citation to the original work is made. The simulations in this chapter represent a reproducible, tune-able, method for examining the transmission of a respiratory disease in a circulating population. By abstracting individuals as 'agents' and the rate of viral transmission as a probabilistic event dependent on real-world parameters, such as the reproductive number R_o, the stochastic process of viral spread can be visualized. Adding parameters that blunt the rate of transmission, mask usage and social distancing in this paper, also enrich understanding of combating the early stages of a viral outbreak.

5.2 Introduction

The COVID-19 outbreak has caused high levels of mortality and economic damage around the world. The causative agent of COVID-19, SARS-CoV-2, is an airborne pathogen that can be transmitted between humans through droplets and aerosols that can travel 1–8 m [29]. The virus is transmitted by both symptomatic and asymptomatic individuals. COVID-19 can cause severe symptoms that require hospitalization in 1–5% of cases, as well as severe long-term sequels and death. Accordingly, the outbreak has seriously impacted healthcare systems around the world [129]. One of the major difficulties to contain the COVID-19

pandemic has been detection of infected asymptomatic or pre-symptomatic individuals, who are estimated to be responsible for as much as 95% of all transmissions [20, 207]. As these individuals carry and spread the virus without manifesting any sign of the disease, they represent a crucial variable in managing the outbreak. In the absence of an effective vaccine or antiviral, most countries have implemented non-pharmaceutical interventions (NPIs) to curb the spread of COVID-19 [156]. These include closure of schools, workplaces, churches, offices, factories and other social venues, while encouraging preventative measures ranging from maintaining social distancing (SD, usually 2 m/6 ft. between individuals) to total quarantine and societal lockdowns. These measures aim to reduce the effective contact rate of the population, which in turn decreases the disease reproductive number R_e. These NPIs limit the epidemic, but they present important drawbacks. Total can only be implemented for short periods, due to its severe impact on the social fabric and economy of a country. Meanwhile, essential workers remain vulnerable to infection and transmission due to the frequent encounters with infected, often asymptomatic, individuals. Because of their social and economic impact, lock-downs and SD measures have been lifted in some countries, leading to reactivation of virus spread and ensuing increased morbidity and mortality. Face masks covering the nose and mouth area also provide a level of filtration that blocks virus transmission to a certain extent[58, 135, 169]. Masks prevent the spread of droplets and aerosols generated by an infected individual, where correctly worn surgical masks can reduce viral transmission by 95%. Uninfected individuals wearing a surgical mask are about 85% protected against infection[137]. Masks may be more effective than restrictions in people's interactions for controlling the spread of infectious virus because they prevent the larger expelled droplets from being converted into smaller droplets that can travel farther, rather than removing the interactions between individuals that cause droplets . Accordingly, face masks reduce the spread of influenza[68] and coronaviruses[13, 112]. In the past, several papers have used theoretical models to study how efficacious mask wearing is in avoiding the spread of airborne viruses. In 2010 at least two studies were focused on the effect of face

mask usage to contrast the diffusion of Novel Influenza A (H1N1)[178, 31]. Although these works are not on COVID-19 or another coronavirus disease, they underline the necessity of developing more accurate models to describe similar diseases and reinforce their results in the light of new diseases. Specifically on COVID-19, the efficacy of mask wearing has recently been studied using an ordinary differential equations (ODE) model[136], which considered also a varying percentage of asymptomatic individuals, compliance with mandate to wear masks, and a different inward and outward efficacy of protection. However, the authors consider face masks as the sole preventative, excluding additional NPIs like SD or shelter in place[29]. Additionally, the problem has been studied in several papers using agent-based models, each being focused on a specific part of the problem. In some cases, the presence of asymptomatic infected individuals was not considered[124, 36]. In other studies, the efficacy of wearing masks was not analyzed when combined with other NPIs[97]. Finally, the difference in inward and outward protection given by a face mask was often neglected or parametrized with a single value[163]. A rather comprehensive data-driven investigation of all these effects has been performed by Hoertel et al.[77]. However, their results are specific to the country of France, and the high dimensionality of the parameter space makes it difficult to disentangle the effect of the various interventions. In our current study, we analyzed the relative efficacy of wearing face masks and/or exercising SD to reducing the spread of COVID-19 in the presence of asymptomatic individuals. This analysis may be particularly important in the current phase of the pandemic. As pharmaceutical interventions (e.g. vaccines) are deployed, people may experience a false sense of safety, which may lead to unsafe behavior. This may allow the virus to circulate at the interface between immune and non-immune individuals, accelerating the emergence of variants resistant to vaccination. Face masks have distinct inward and outward protection, parameterized using a Gamma function (see Methods). Through stochastic computer simulations of infection spread, we modeled realistic outbreak scenarios and found that SD only yields beneficial effects if accompanied by a widespread population adherence to SD. In contrast, wearing face masks is a highly

99

effective strategy to reduce the spread of infection. Our results are general, and suggest that, even when a large fraction of infected individuals is asymptomatic, mask wearing is the most effective strategy to control virus spread and alleviate the impact of COVID-19 outbreak, particularly when combined with conditions of partial SD compatible with the function of society.

5.3 Results

5.3.1 Stochastic model description and calibration

We developed an agent-based model (ABM) to examine the effectiveness of wearing masks and SD on the rate of infections and viral spread during the pandemic. Unlike ODE models of the spread of COVID-19 disease[136, 109], ABMs are stochastic models that allow the description of non-homogeneous distributions of agents that act individually[80, 24]. In ABMs, each individual behaves dynamically and independently in response to environmental changes[149] according to rules that describe their interactions. To model the COVID-19 pandemic, we used a SEAIR system in which each agent represents an individual who can be susceptible (S), exposed (E), asymptomatically infected (A), symptomatically infected (I), or recovered (R). Although important, we do not explicitly consider reinfection with the same or a different viral variant, as it is outside the scope of this work. To obtain a realistic model of virus spread, we chose parameters that describe the spread of SARS-CoV2: transmission events occur through contacts made between susceptible and infectious individuals in close proximity (distance $\leq$ 2r, **Figure 5.1.A**), and exposed individuals undergo an incubation period of 5.1 days to become infectious (Fig. 1, spheres with red border). This incubation time represents the interval required to increase viral loads to levels sufficient for transmission[20, 207, 59]. We assume that recovered individuals (Fig. 1, spheres with black border), who resolve the infection, cannot be re-infected or infect others, which is a reasonable assumption for the duration of our models (45 days). Symptomatic agents are in

100
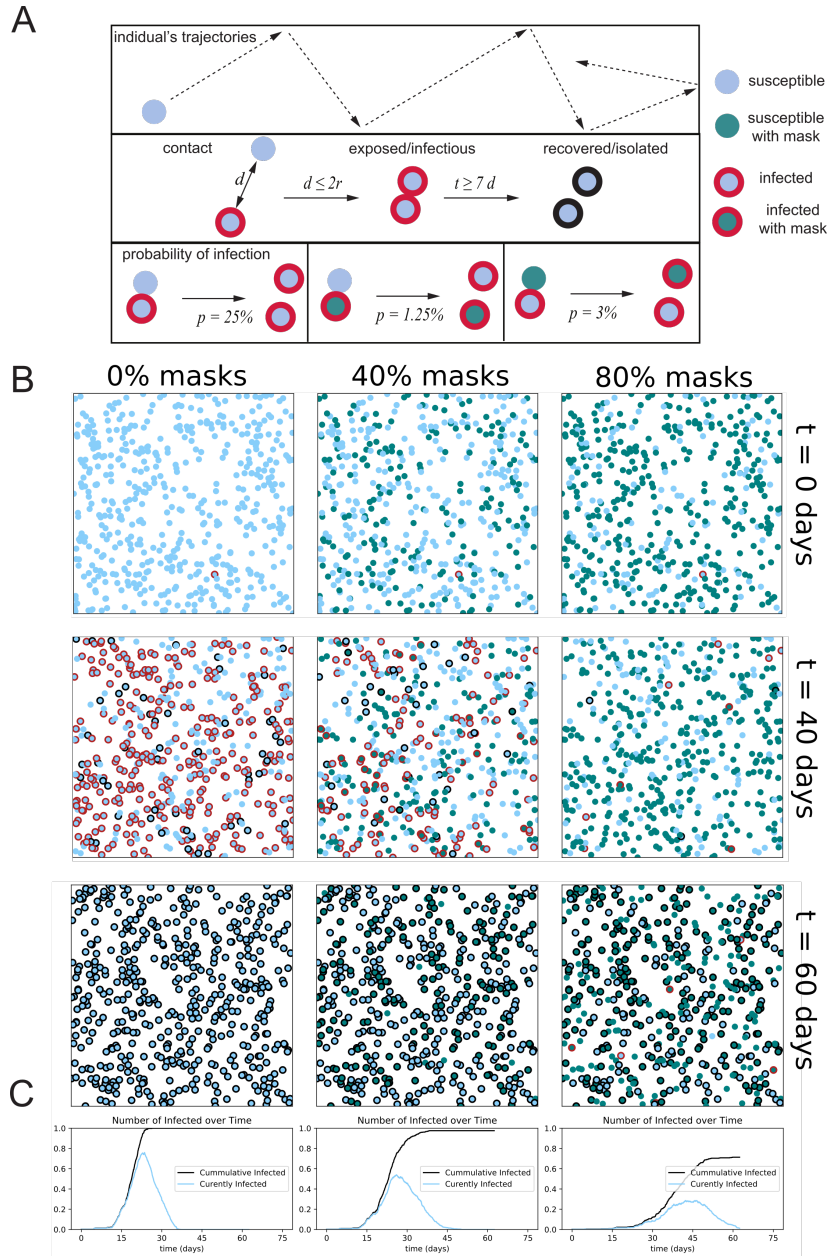
Figure 5.1: Individual states and rules of interactions

(a) Different states an individual can be in during a simulation using the same coloring system used in animated simulations. Individuals keep the mask or not masked attribute assigned at initialization during the course of the simulation.
A) Spread of infection is caused by interactions of overlapping trajectories between infected and susceptible individuals. If the distance between individuals, d, is less than the radius of the two individuals, r, then an interaction occurs. Interactions initiate the generation of a random number that determines if transmission occurs. **B)** Individuals social distance by not moving during the simulation such that the rate of contact with other individuals is decreased. **C)** demonstrate the probabilities of interactions when infected and susceptible individuals are both not masked, infected is masked, and susceptible is masked, respectively.

the Infected state for 7 days but are only infectious to other agents for 12 hours. Asymptomatic agents are infectious for all 7 days but the probability of transmission is reduced by 33%. Presymptomatic agents are similar to Susceptible agents in their interactions but have a countdown for 5.1 days until they become either asymptomatically or symptomatically Infected. To define the probabilities of infection, we used reported COVID-19 parameters[59]. The probability of transmission follows a G (gamma) distribution (see Methods) whose shape is described by a constant (a), estimated to be 0.25. Wearing masks reduces this probability (**Figure 5.1**, probability of infection). To estimate the protective effect of masks, we used parameters determined for FDA-approved surgical masks, whose efficacy has been experimentally verified to inhibit virus transmission[137]. Based on previous studies (Leung et al.)[113], we assumed that, if an infectious individual wears a mask, the effective probability of transmission is reduced by 95%. If a susceptible individual wears a mask, a is reduced by 85% (**Figure 5.1.A**). Our assumption that wearing masks is more effective to reduce transmission than to prevent getting infected is supported by experimental data[115]. However, if both infectious and susceptible individuals wear masks the probability of transmission is the product of these probabilities (0.0075) and, thus, sufficiently low such that transmission is effectively null. We calibrated our model by running simulations without any individuals wearing a face mask or practicing SD and considering that 50% of infected individuals are asymptomatic at the beginning of the simulation, with each new infection throughout the epidemic having a 50% probability of being asymptomatic. In this way, we determined the simulation parameters, such as velocity and density of individuals, to obtain a value of R_O = 2.5, consistent with what was reported early on as the infection rate of the epidemic in Wuhan[113].
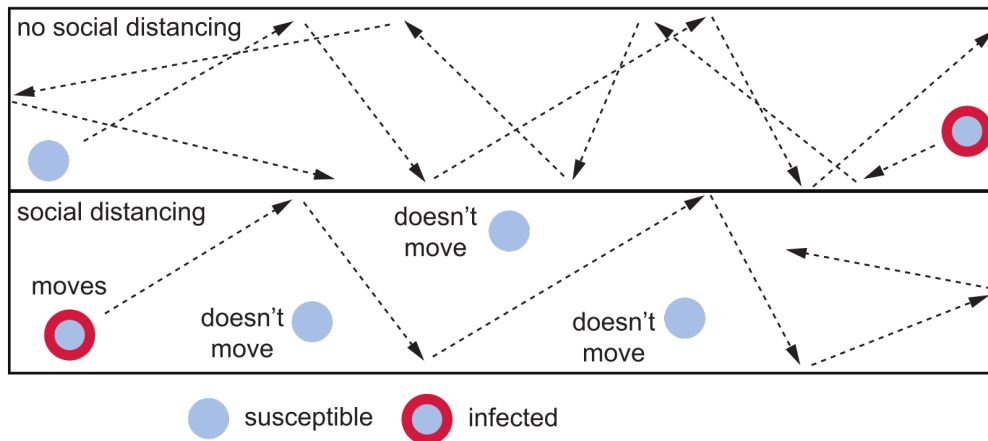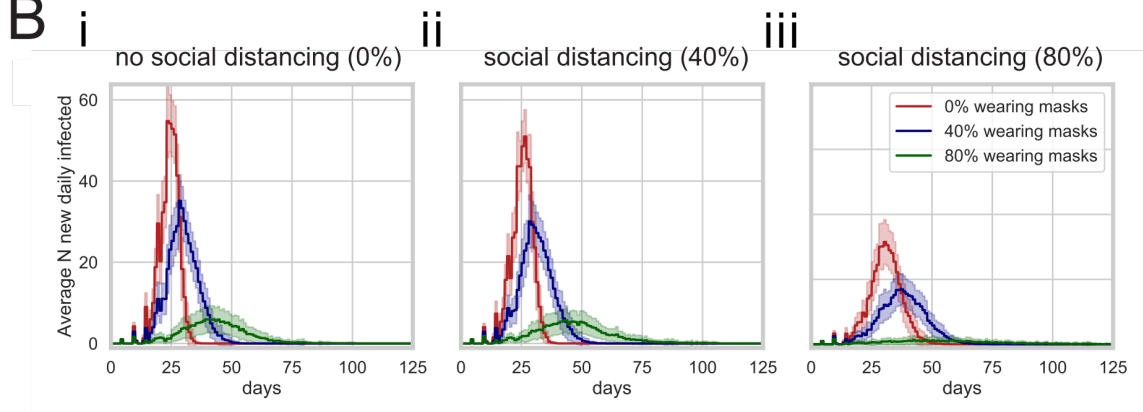
Figure 5.3: Average new infections per day varying the population wearing masks and practicing social distancing

The number of new infections per day for 0%, 40%, or 80% of a population wearing face-masks are displayed by the red, blue, or green trajectory, respectively, for 0% of the population practicing social distancing (A), for the 40% (B) and for the 80 % (C). Simulations were repeated 100 times for each condition, the curves and the highlighted regions around the curves represent the mean value ± one standard deviation.

5.3.2 Percentage of population wearing masks changes the daily disease incidence

We started each simulation with one individual being infected and all others susceptible and assuming all subsequent infections have a 50% chance of being an asymptomatic. Non-infected and asymptomatic individuals circulate in the population without any restriction (i.e., they do not isolate themselves or become hospitalized) (see Methods). In contrast, symptomatic individuals no longer move after 12 hours of the symptom onset, simulating hospitalization or self-isolation. Thus, symptoms are assumed to manifest after the incubation time of 5.1 days (**Figure 5.2.B**). Using these assumptions and model calibration, we carried out a set of simulations in which we gradually increased the percentage of individuals in the population that wear masks. Individuals, who are assigned randomly to wear a mask at the beginning of the simulation, keep on the mask for the entire duration of the simulation. Increasing the fraction of the population wearing face masks has a highly significant effect on the spread of the virus (**Figure 5.1.B**, **Figure 5.1.C**). Mask wearing reduces the cumulative number of infected individuals at the end of the simulation (Fig. 1B). Strikingly, we observed a negative correlation between the percentage of the population wearing masks and the overall number of cases (Fig. 5.1.B). The description of the dynamics of infection generated by this model is consistent with previous clinical studies[113, 115] and highlights the benefit of wearing masks (**Figure 5.1.C**). If the daily incidence surpasses the treatment capacity, it will overwhelm the healthcare system with detrimental consequences for medical care of infected individuals and increased mortality and morbidity. Thus, we examined the effects of face masks on the daily incidence of infection over time (**Figure 5.2.B**). If all individuals move freely and randomly interact with others (i.e., 0% SD), the rate of daily infection through the population depends on the percentage of individuals wearing masks. The average number of new daily infection varies considerably, according to the number of individuals wearing face masks. When 0% of individuals wear face 195 masks (**Figure 5.2.B**, red line), the number of daily infections peaks sharply at day 27 with a maximum of 54.8

(51.2, 58.4 95% C.I.) infections per day for a population of 500 individuals. No additional infections are observed after day 39, when the entire population (100%) has been infected. Thus, without any intervention, the infection quickly reaches every individual through an epidemic characterized by a very sharp infection peak. Note that, in these original models, we assume all individuals recover after 11 days post-infection and cannot be re-infected. When 40% of all individuals wear masks, the number of individuals infected at any given day is reduced by approximately 30% (maximum of infected individuals 35.1 (32.6, 37.7 95% C.I.) **Figure 5.2.A**, blue line), both flattening the curve and extending the duration of the outbreak by more than 10 days, with a peak maximum at day 32. By day 52, an average of 472 individuals has been infected, and none of the individuals is infectious or exposed any longer. Even more significantly, if 80% of the population wear masks, we observed a significant flattening of the curve, with a substantial reduction in the maximum number of infected individuals per day, 5.9 (4.6, 7.3 95% C.I.) (**Figure 5.2.A**, green line), and the number of new infected individuals reached zero by day 57.8 ± 35.0. Thus, the shape of the outbreak changes from a curve characterized by a sharp peak when no intervention is considered to a broader peak when 80% of the individuals wear masks. By increasing the percentage of the individuals wearing masks, the number of newly infected individuals per day substantially decreases, which will reduce mortality and morbidity. Moreover, since the use of masks eliminates the sharp peak that characterizes SARS CoV2 epidemics, the overall impact of the outbreak on the health system is alleviated. These results highlight the importance of widespread mask wearing as an effective intervention that can be implemented as soon as the first cases are reported.

5.3.3 Effect of social distancing on viral infection spread.

Next, we evaluated the effect of SD in shaping the spread of infection. Practicing SD does not affect the probability of infection conditional on an encounter but reduces the chances of encounters leading to transmission. Thus, SD was introduced into the model by

limiting the proportion of individuals in the population that move freely in the field. This simulates a scenario in which a given proportion of individuals in the population quarantine or shelter-in-place, thereby reducing the probability of contacts and transmission (**Figure 5.2.A**). As reported, if a percentage of individuals practice SD, even without any other non-pharmacological intervention, the number of infections and daily infection rate are reduced (compare **Figure 5.2.B**, SD 0, 40, and 80%, red line). However, if no one wears masks but 40% of individuals practice SD, we observed a very small effect in the shape of the infection curve (**Figure 5.2.B**, the peak maximum decreases from 51.0 (48.3, 53.6 95% C.I.) to 30.1 (27.5, 32.7 95% C.I.) ()). When 80% of the population practices SD, a more significant reduction in the number of new daily infections was observed (Fig. 2B, 80%). Notably, the shape of the new daily infection curve broadens considerably upon increasing the percentage of individuals wearing face masks (Fig. 5.2.B, compare blue and green curves with red curve). For instance, if 80% of the population wears masks with 40% SD, the peak maximum decreases to one-tenth (from 51.0 (48.3, 53.6 95% C.I.) to 5.7 (4.5, 6.7 95% C.I.)) and is slightly delayed (**Figure 5.2.B**). At 80% SD, the peak of new daily infections is no longer observed, and the number of new infected individuals per day averages 1.6 (1.4, 1.9 95% C.I.) (**Figure 5.2.B**). Thus, the effects of individuals wearing face masks and practicing SD are synergistic, with the most pronounced effects occurring when 60% or 80% of individuals wear masks. It is possible that our results may vary depending on the way social distancing is implemented in the model. To test this possibility, we carried out additional simulations in which modulate the amounts of social distancing by completely removing infected agent practicing SD from the simulation, and only allowed infected agents to be symptomatically infected (see **SM 5.6**). The results from these simulations were similar to those described above, confirming that around 60-80% of the population is required to practice SD to effectively slow the rate of infection, even when SD reduce the probability of transmission to zero. Our results also show that, if infection is always symptomatic, the number of infections drops significantly, which is consistent with the spread driven by

asymptomatic individuals.

5.3.4 Effectiveness of combining mask wearing and social distancing to control infection in populations with high proportions of pre-symptomatic and asymptomatic cases

Asymptomatic or pre-symptomatic SARS-CoV-2 infection is emerging as possibly the most common clinical manifestation of COVID-19[138, 88, 15, 47, 38]. This finding could only be revealed once mass testing campaigns were performed, regardless of symptoms (e.g., universal testing campaigns). One of the earliest studies documenting clinical manifestations in a testing campaign (which still focused testing mainly on symptomatic individuals) was on the Diamond Princess cruise ship, where the rate of asymptomatic infection was 18%[132, 131]. In a mass testing campaign in Iceland, where testing was offered to a segment of the general population (regardless of symptoms), 43% of individuals were asymptomatic at the time of testing[69]. Thus, the actual percentage of pre-symptomatic and asymptomatic cases is currently unknown, but it is clear that a large number of SARS-CoV-2 new infections derive from undetected infections. Controlling the outbreaks by isolation or even by increased population testing is a big challenge and may be difficult to implement. We thus determined the efficacy of mask wearing and SD in the context of different proportions of asymptomatic incidence. We assume that asymptomatic individuals are less infectious than symptomatic individuals: asymptomatic individuals may have lower viral loads and reduced coughing, sneezing, and nasal secretions, all of which may facilitate transmission[32, 153, 60]. The model considers that symptomatic infected individuals isolated themselves 12 hours after the onset of symptoms, because they get hospitalized or self-isolated. In contrast, asymptomatic individuals remain infectious, circulate and transmit for a period of 7 days (**Figure 5.3.A**). Because some individuals can be pre-symptomatic (i.e., symptoms emerge later after the initial incubation time (**Figure 5.2.B**, t= 5.1 days)), we modeled infectivity of asymptomatic/pre-
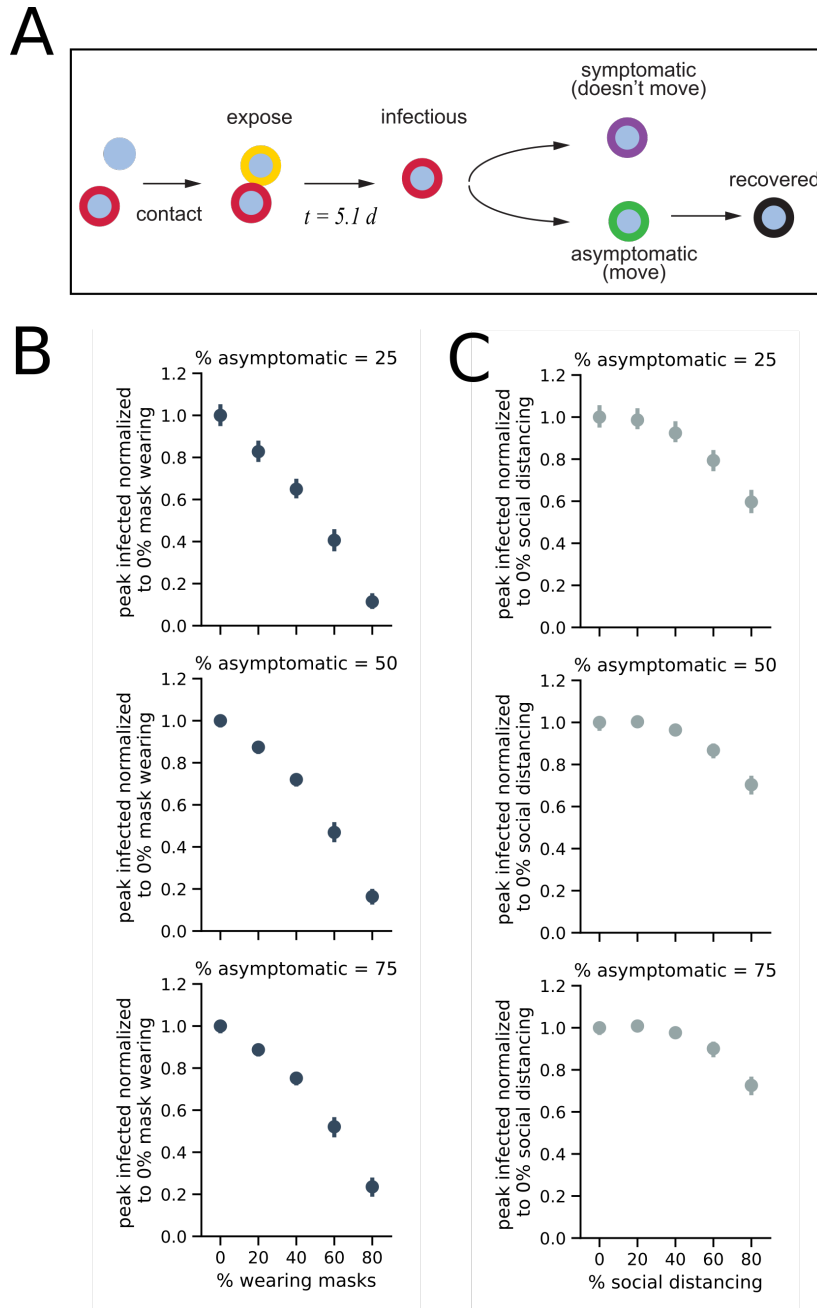
Figure 5.4: Summary values from 2500 simulations of varying percentages of population wearing masks or social distancing

A) The average cumulative incidence is represented as a function of the population practicing social distancing or wearing a mask, which are given by the x and y axis, respectively. B) Full-width half-maximum (FWHM), denoting the number of days between the first day and last day of cases that have half the peak number of infected individuals. C) Extinction rate of the infection estimated as the average number of days for which the simulation reports no new infected individuals. In the figure, the numbers represent the mean value calculated over 100 of simulations carried out for each condition. For clarity, we reported the standard deviation of the mean for each value reported in this figure in Fig. SM 5.5.

108

symptomatic as linearly declining until the individual is no longer infectious, after 7 days[73]. Using these assumptions, we performed a sensitivity analysis by carrying out simulations, varying the percent of asymptomatic/pre-symptomatic cases to determine the efficiency of non-pharmacological interventions in populations with 25, 50, and 75% pre-symptomatic and asymptomatic infected individuals (**Figure 5.3**). Our simulations demonstrate that the total number of infected individuals increases linearly with the increase of the percentage of asymptomatic individuals in the population (**Figure 5.3.B**). To compare each condition, we normalized the peak of new daily infected individuals 277 to conditions in which no one practiced SD or wore masks. Strikingly, increasing the percentage of individuals wearing masks linearly reduces the normalized peak number of infected individuals per day (**Figure 5.3.B**). For instance, when 40% of the individuals wear face masks, the peak number of infected decreases similarly independently of the percent of asymptomatic cases considered (to 0.6–0.7, Fig. 3B). Furthermore, the linear relationship between the decrease in peak number of newly infected individuals per day and increase in percent individuals wearing masks is independent of the proportion of asymptomatic individuals in the population (**Figure 5.3.B**). This finding indicates that, when the fraction of asymptomatic cases is high, as in the case for COVID-19, wearing face masks is as effective to reduce the peak number of infected as when a low percentage of individuals are asymptomatically infected. In contrast, SD was only effective in populations with high incidence of asymptomatic infections when a very high fraction of the population practice SD (more than 60%) (**Figure 5.3.B**). Furthermore, the low efficacy of SD as a containment strategy is more pronounced when the proportion of asymptomatic individuals increase (compare 25, 50, and 75%). Of note, if the number of individuals wearing face masks is high, increasing the number of individuals practicing SD has negligible effects on the daily number of infected individuals (see supplementary materials). One noteworthy observation from our model is that, at high rates of SD (e.g. 80 %), there is more variability. Our analysis uncovers a linear relationship between the fraction of a population wearing masks and the reduction in infection rate. In contrast, we find SD

109

requires a high fraction of compliance to be effective. These findings indicate that having a high percentage of individuals wearing face masks is more beneficial in preventing virus spread and reducing the peak number of infected individuals than having a high percent of people practicing SD. Notably, the benefit of wearing masks is not affected if the percent of pre-symptomatic and asymptomatic increases.

5.3.5 Interplay of face masks and social distancing for controlling infection spread and protecting from COVID-19

Next, we determined the average cumulative incidence as a function of the percentage of individuals wearing masks and practicing SD (standard deviation 304 described in **Figure SM 5.3-A**). When neither SD nor masks were used our simulations indicate that up to 99% of the population will end up infected, leading to unacceptable levels of mortality and morbidity. When the proportion of the population wearing masks was increased, no significant effect on the total number of infected people was noted until more than 40% of the population wore masks. However, if 80% of people use masks, the average cumulative incidence of infection decreased to around 35%. Therefore, wearing face masks alone would greatly limit the spread of the virus. In contrast, SD alone does not have a significant effect. Increasing SD compliance to 80% only reduced total infections by 8%, and 87% of the population was eventually infected. Importantly, the combination of wearing masks and practicing SD by a high proportion of the population dramatically reduces the total number of infected individuals to 10% of the population (**Figure 5.4.A**; and **Figure SM 5.2.C**). To gain additional insights into the characteristics of the epidemic in response to these mitigation strategies, we studied the shape of the epidemic curve by calculating the peak and full width half-maximum (FWHM) of the peak of the new daily infections (Methods). While the peak reports on the maximum number of daily infections at the height of the epidemic, the FWHM is a simple way to represent the duration of the characteristic peak of new daily infections. Indeed FWHM reports on the extinction time of the infection
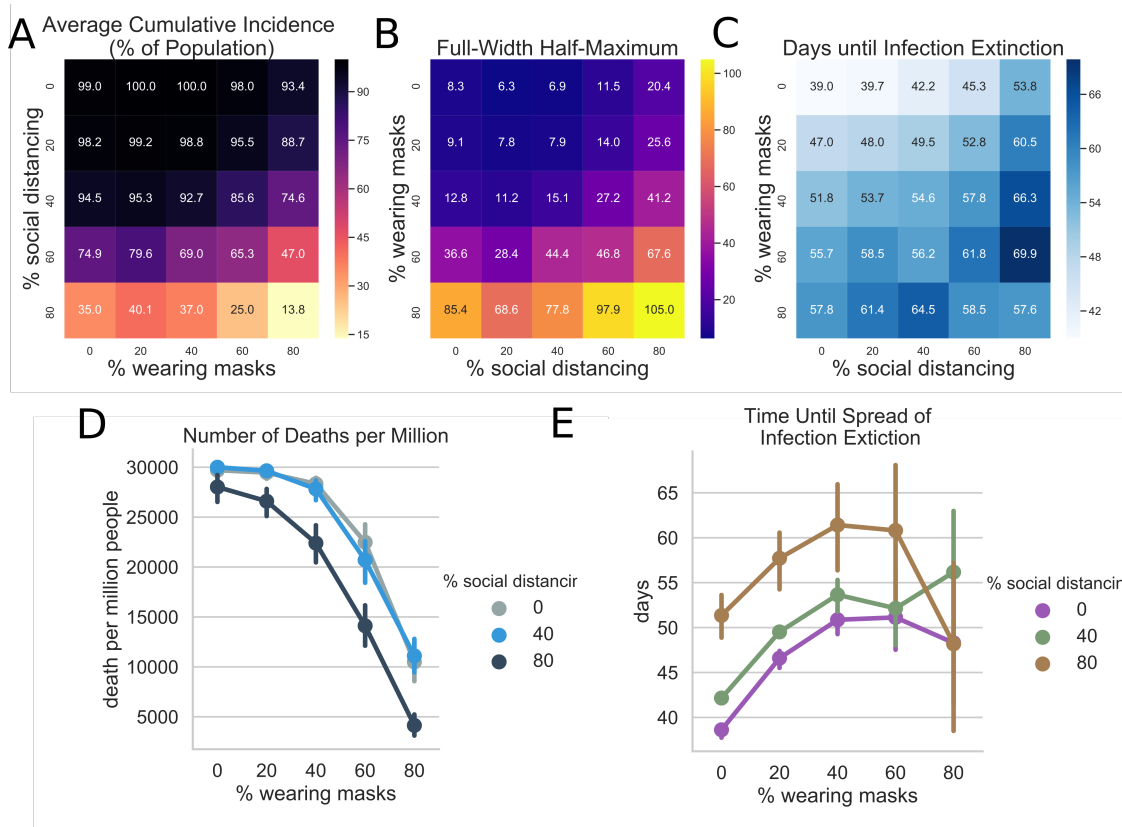
Figure 5.5: Effects of the asymptomatic population on the infected peak number
A) The peak number of infected individuals is represented as a function of the percentage of the population wearing face mask and as a function of the percentage of asymptomatic individuals. 25 % of asymptomatic individuals is colored gray, 50 % bright blue, 75 % dark blue as the legend reports. Sensitivity analysis reporting how the peak number of infected individuals is impacted by the 25 % **B)**, 50 % **C)**, and 75% **D)** of asymptomatic individuals varying the percentage of the population wearing face masks and the percentage of the population practicing social distancing. The legend reports the percentage of individuals practicing social distancing: 0% is colored gray, 20% bright blue, 40% dark blue, 60 % purple, 80 % red. Error bars are the standard deviation of the mean.

within the population (number of days until no individual is still infected) (**Figure 5.4.A**, and **Figure SM 5.3.B** standard deviation). A larger FWHM corresponds to a flatter but longer epidemic curve. A flatter epidemic curve enables better management of the epidemic, as the healthcare system is not overwhelmed by the number of cases at a given time. Initially, the FWHM was calculated assuming no individual practice SD. FWHM was 8.3 days if none of the individuals wears masks, 12.8 if 40% of individuals wear masks, and but increases dramatically to 85.4 when 80% of the population wears masks (**Figure 5.2.B**). Our data indicate that wearing masks has a more profound effect than SD on flattening the epidemic curve. For instance, when 80% of the population wears masks, the epidemic curve is eight times flatter than without any non-pharmacological intervention (**Figure 5.4.B**). In contrast, if 80% of the population practices SD, the flattening of the curve is less than threefold. The most dramatic effect on flattening of the curve is observed when wearing masks is combined with SD; for instance, if 80% of the population wears masks and 80% practices SD, the curve is flattened over 10-332 fold, compared to no intervention. We also find that the reduction in the number of infected individuals per day correlates with a lengthening of the outbreak. Broadening of the peak affects the extinction time of the infection (**Figure 5.4.C**). For instance, when the percentage of individuals wearing face masks rises from 0 to 80% of the population, the extinction time increases from 39.0 to 58 days (**Figure 5.4.C**). Similarly, as a higher proportion of individuals practice SD, the time to extinction of the infection also increases (Fig. 5.4.C, 39 to 54 days for 0% to 80% of SD). Importantly, even though the time to epidemic extinction is extended, the total number of infected individuals dramatically decreases (**Figure 5.4.A**). If a higher proportion of the population (80%) wears face masks and practices SD, the time to epidemic extinction is reduced (**Figure 5.4.C**) because the total number of infected individuals is dramatically reduced (**Figure 5.4.A**). Thus, stochastic effects dominate, and this can be appreciated by the wider error bars (**Figure 5.4.F**). To relate the impact of these interventions to their societal impact, we determined the number of deaths per million after each mitigation

112

strategy, assuming a mortality rate of %3 [4]. This analysis illustrates the heavy cost of lives of the virus, but also demonstrates that a high level of mask wearing compliance is the most effective non-pharmacological approach to protect human lives, particularly when combined with even moderate SD measures (**Figure 5.4.D**). In contrast, SD, without masks wearing is not effective to reduce mortality (**Figure 5.4.E**). Finally, our simulations predict that increasing the proportion of the population wearing masks will increase the time to outbreak extinction (from 40 to 60 days) (**Figure 5.4.F**). Together with the broadening of the peak (**Figure 5.4.C**), this shows an effective flattening of the curve. Importantly, with 80% mask wearing, we observed an increase in the statistical distribution from the average time to extinction (**Figure 5.4.F**, see 95% confidence intervals). Thus, a generally low disease incidence triggers stochastic events leading to extinction of the infection. Our simulations represent real outbreak scenarios and reveal that as the outbreak approaches its extinction there is an increase in the uncertainty of whether or not the infection has been completed eliminated, which argue to be prudent before society reopening can be done safety.

5.4 Discussion

Here we use realistic simulations rooted in experimentally measured parameters of SARS-Cov2 spread, contagion mode and mortality, to evaluate two available NPIs that reduce the spread of a respiratory infection, such as COVID-19. In our simulation, we assumed proper use of FDA-approved face masks. We showed that a high degree of compliance in the use of masks, regardless of whether the wearer displays symptoms, slows the spread of infection. Face masks substantially reduce the transmission of respiratory droplets and aerosols containing viral particles[113, 137, 105]. Increasing the fraction of the population wearing face masks reduces the number of new infected individuals per day and flattened the curve of total individuals infected (**Figure 5.2.A and 5.4.A**). These two effects should reduce mortality and morbidity, alleviate the current stress on healthcare systems, and en-

able a more effective management of severe cases. However, solely wearing masks cannot entirely prevent an outbreak from occurring. It cannot by itself extinguish the virus, since as long as a small fraction of the population is non-compliant, the virus can persist in the population. Our models show that combining proper use of masks with practices such as SD, indisputably decreases the number of new infected individuals per day (**Figure 5.2**). The asymmetry between the effectiveness of SD and mask wearing is of particular interest. In a classical, ODE-based epidemiological model, mask wearing and SD would both affect the transmission rate. In the absence of SD, imagining a 100% effectiveness of mask, the reduction in transmission due to mask wearing would be the same as the decrease due to SD in the absence of mask wearing. In fact, both controls would be, effectively, modeled as a removal of people from the population. On the other hand, our simulations show that mask wearing has a stronger effect than SD on the disease incidence. This is due to the way we model SD, that is, as a decrease in mobility. A better approximation of our model is to consider an epidemic dynamic on a scale-free network, where homogeneous mixing is relaxed and SD is modeled as a change in the degree distribution of the network[98]. In addition, our model was demonstrated to be scalable and able to describe realistic situations such as interactions between 5000 agents (see supplementary materials). Our analysis provides guidance for policies to protect the population from COVID-19. Optimizing the use of masks with SD practices effectively limits the virus spread and reduces several parameters in the epidemic, including cumulative incidence, shape of the peak, and the extinction rate (**Figure 5.3**). In particular, we observed that wearing masks is more effective than SD. Even in a population with a high number of asymptomatic infections, increasing the use of masks up to 80% results in a significant reduction in infection (**Figure 5.4.A**). Meanwhile, even 80% of individuals practicing SD has only a marginal effect (**Figure 5.4.D**). This result can be understood in terms of contact rate, since we assume that asymptomatic infectious individuals have higher mobility than symptomatic infectious ones. If the vast majority of the population is asymptomatic, then high compliance with face mask use is a

114

key factor for curbing the epidemic. Moreover, we believe that our methods are general and they may inform policies against other respiratory infections like influenza. Our simulations also provide insights into how enforcing different mitigation practices affects the length of the epidemic. Assuming a homogeneous population, the trajectory of epidemic extinction lasts 50–60 days, when 80% of the population either wears masks or practices SD (**Figure 5.4.C**). However, when 80% of the population is wearing masks and 0% of the population is practicing SD, the cumulative incidence is reduced three times (35%), and the peak is very broad (FWHM of 85 days). In contrast, when the population solely practices SD (80%), the majority of the population (93%) will end up infected, and the peak of daily infected individuals will be sharper (FWHM of 20 days). Our model indicates that the synergistic utilization of face mask wearing and social distancing practice is most effective in controlling SARS-CoV-2 spread. We observed that wearing masks in combination with some degree of SD relaxes the need for a complete lockdown, leading to a potential suggestion for an intervention policy based on a mix of the two measures. The effectiveness of mask wearing to control virus spread is not reduced if a large fraction of the population is asymptomatic. This suggests that, in the absence of universal 412 testing, widespread use of face masks is necessary and sufficient to prevent a large outbreak. Our results are supported by the real data of Iceland[69] and Taiwan[32], where an early mandate to requiring face mask usage, in combination with SD, severely limited the spread of the virus. While more work is necessary to specifically assess the impact of other variables shaping COVID-19 outbreaks, such as increased mobility, age stratification, testing a fraction of the population, our study can accurately inform strategies to reduce the spread of the virus. In particular, our results may be highly relevant toward informing specific realistic situations, such as the spread of the disease in a confined space, where effective SD may not be easily achievable (e.g., schools, essential businesses, correctional facilities, public transportation, hospitals). These strategies, if effectively implemented, will save countless lives from the SARS-Cov2 infection. According to our model, if the United States (330 million people) does not implement any NPIs,

then 627,000 people are expected to die. Contrastingly, if 80% of the population wear face masks, that number would significantly shrink to about 250,000. If both face masks and SD were practiced by 80% of the population from the start of a pandemic, the mortality rate decreases to 65,600 people.

5.5 Materials and Methods

We developed and used our python codes using the NumPy library version 1.15.422 [184] to carry out ABM and describe the dynamic evolution of a SEAIR system affected by COVID-19 disease, in which each individual can be in a susceptible (S), exposed (E), asymptomatic infected (A), symptomatic infected (I), or recovered (R) status. In addition, each individual can wear a face mask (M) or can practice social distancing (SD), where wearing face masks or practicing social distancing are independent binary values of an individual. In the simulations, each individual was represented by a position in a 2-D lattice of 21x21 dimension. Individual initial positions are assigned randomly by NumPy's random module and the simulations start with all susceptible individuals but only one exposed. During the simulation, each individual move along a randomly oriented trajectory at a constant velocity, moves the same distance between each time step of the simulation, and interacts with individuals whose position is within a fixed diameter of another individual. During the simulations, each individual's data are saved as vector of attributes including position, velocity, state (S, E, A, I, R, M, SD), and number of individuals they come into contact with at every simulation time step. A time step corresponds to 1 hour. We implemented the state of M by defining sub-routine during the interaction between two individuals where the probability of infection is reduced by an amount corresponding on which of the two individuals are wearing a mask. For the SD state, we assigned the individual to be stationary and not follow along a randomly assigned trajectory. We refer to Ferguson et al. for defining the rules governing the interactions among individuals[124]. For the interaction between symptomatic infected

and susceptible individuals, the infection probability was randomly sampled from a gamma distribution with a mean of 1 and a shape of 2.5, whereas for that between asymptomatic infected and susceptible individuals, that infection probability is reduced by 33%. We assume this reduction of infectivity for the asymptomatic based on the absence of transmission-aiding symptoms such as coughing, sneezing, and a runny nose[124]. The time between a susceptible individual being exposed to being infected is 5.1 days. Symptomatic infected individuals are infectious for 12 hours. After this time, we assume that these individuals no longer infect those around them because they are hospitalized or self-isolating. Asymptomatic infected individuals are infectious for 7 days and the infectivity linearly declines until the individual is no longer infectious on day seven[149]. If an infected, a susceptible, or both individuals are wearing a mask their probability of another individual being infected is reduced by 95%, 85%, or 100%, respectively, from the original gamma distribution. First, we carried out a simulation with 500 individuals with 0% of individuals wearing face masks and 0% practicing social distancing to optimize parameters as velocities and individual density in order to obtain a basic reproduction number, R0, equal to 2.5 based on previously reported values. The basic reproduction number was computed from the mean number of symptomatic cases resulting from a single symptomatic individual. Then, we carried out 4 more sets of simulations in which we increased the percentage of individuals wearing masks by the 20, 40, 60, and 80 %. Finally, for each of these simulation sets we carried out 4 more sets in which we increased the percentage of individuals practicing social distancing by the 20, 40, 60, and 80%. Simulations are stochastic and we simulated each condition 100 times in order to have good statistics. Totally, we simulated 25 different conditions for a total of 2500 simulations, 100 for each condition. In all these simulations, the probability of a new infection being asymptomatic is 50%. Simulations were run until there were not any individuals either infected or exposed. Summary values were computed by methods in the NumPy module. Error bars were calculated by the standard deviation method in NumPy. The full-width half-maximum (FWHM) is calculated for each simulation from the newly

117

infected per day data by taking the maximum and using it to find the days that intersect the value of half the maximum value. The first and last days of this intersection were then used to calculate the number of days of the FWHM. From the set of FWHM for each simulation, an average and standard deviation were calculated using the NumPy module. FWHM error bars are large due to a large variation in how flat the curves are. Graphs were created by using the Matplotlib[3] and Seaborn[5] modules in python. We followed the same protocol described above to perform simulations with varying to 25 and 75% the probability of a new infection being asymptomatic. Finally, to monitor the reproducibility of our results with a larger population and contrast with real data, we ran 4 sets of 30 simulations with 5000 individuals in the combinations of 0% or 80% social distancing and 0% or 80% wearing masks. All 5000 individual simulations were done with 50% asymptomatic infection rates. As the position, trajectory, and state of each individual in the simulation is explicitly known, using the matplotlib library's animation package, we converted each time step of the simulation to an image in a movie, representing one day as a second spanning the length of the simulation. For each simulation, we saved in a .csv in tidy data format the summary values of the simulations, which we used for the analysis. The simulation was written in python and all scripts are available on GitHub at `https://github.com/adamcatching/SARS_SEIR_Simulation`, simulations were generated using script `mask_single_sim.py`.

5.6   Supplementary Materials
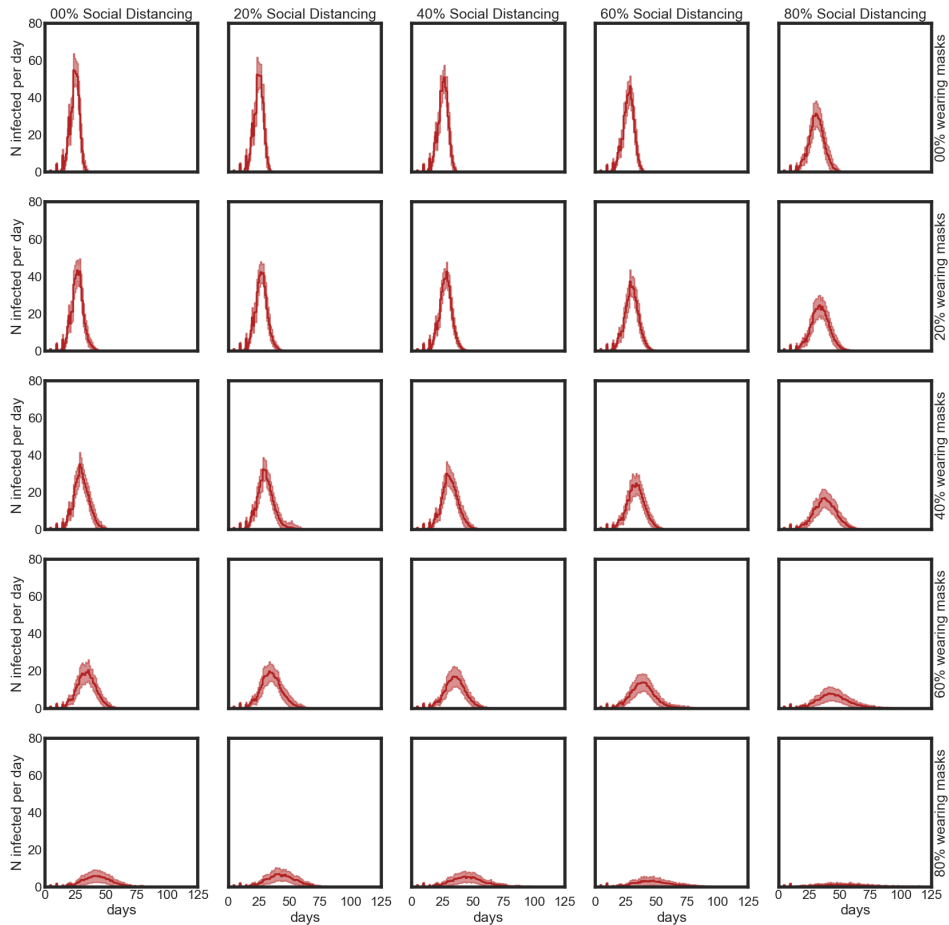
Supplementary Figure 5.1: Number of infected agents with 50 percent of asymptomatic infected population

Number of infected agents as a function of time for all combinations of different percentage of the agent population practicing social distancing (x-axis) and wearing masks (y-axis). 100 simulations are represented for each condition and each simulation is displayed as a low-opacity trajectory over time.
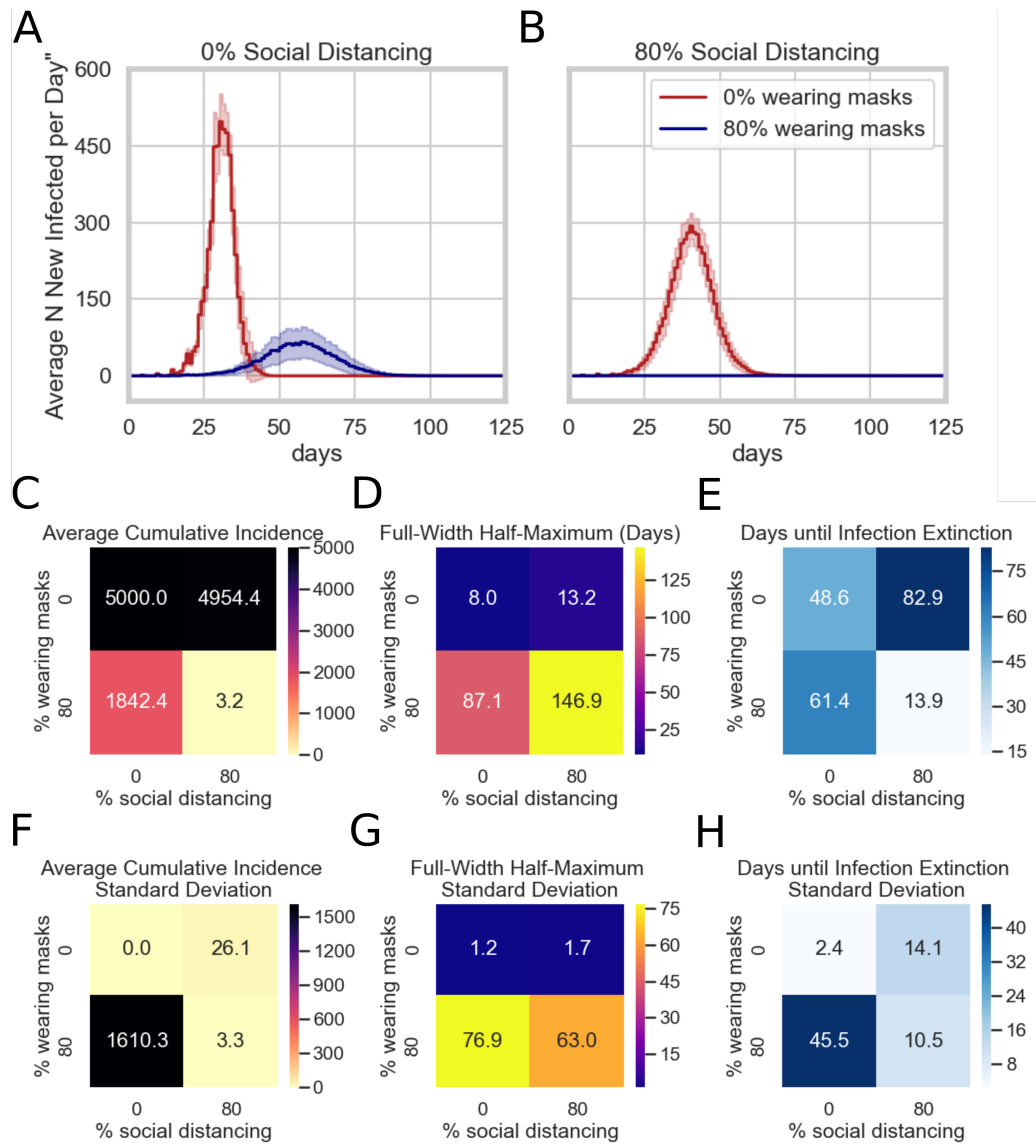
Supplementary Figure 5.2: Dynamics of the epidemic with simulations of 5000 agents

Simulations were run with 500 agents. **A)** and **B)** report the number of new infected agents per day calculated for either 0 % (red line) or 80 % (blue line) of the population wearing masks and for either **A)** 0 % practicing social distancing or **B)** 80 % practicing social distancing. **C)** The average cumulative incidence is represented as a function of the population practicing social distancing or wearing a mask, which are given by the x and y axis, respectfully. **D)** Full-width half-maximum (FWHM), denoting the average number of days between the first day and last day of cases that have half the peak number of infected agents. **E)** Extinction rate of the infection estimated as the average number of days for which the simulation reports no new infected individuals. Data for each condition was simulated 30 times and the highlighted regions around lines in figures **A)** and **B)** represent the mean value +/- one standard deviation. **F)**, **G)**, and **H)** represent the standard deviation of the mean reported in **C)**, **D)**, and **E)**.
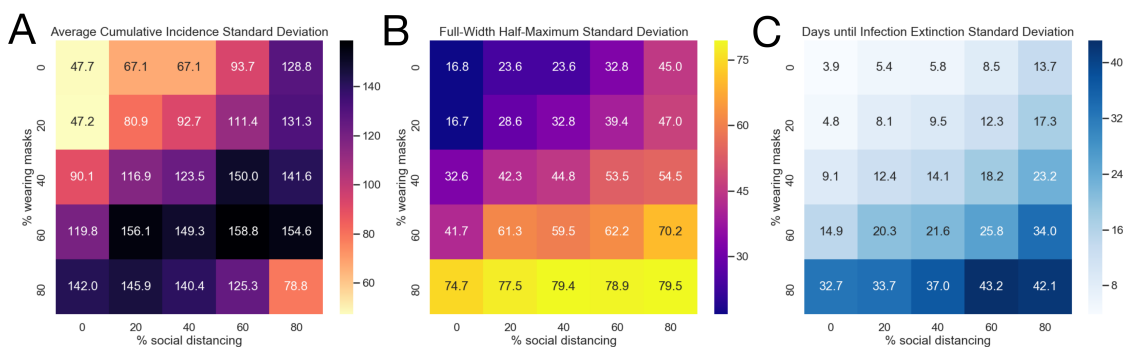
Supplementary Figure 5.3: Standard deviation of summary values from 500 agent simulations varying percentages of population wearing masks or social distancing.

Each condition was simulated 100 times and standard deviation of the mean values reported in Figure 2 is represented. **A)** The standard deviation of the average cumulative incidence is represented as a function of the population practicing social distancing or wearing a mask, which are given by the x and y axis, respectfully. **B)** The standard deviation of the Full-width half-maximum (FWHM), denoting the standard deviation number of days between the first day and last day of cases that have half the peak number of infected agents. **C)** Standard deviation of the extinction rate of the infection estimated as the standard deviation number of days for which the simulation reports no new infected individuals.
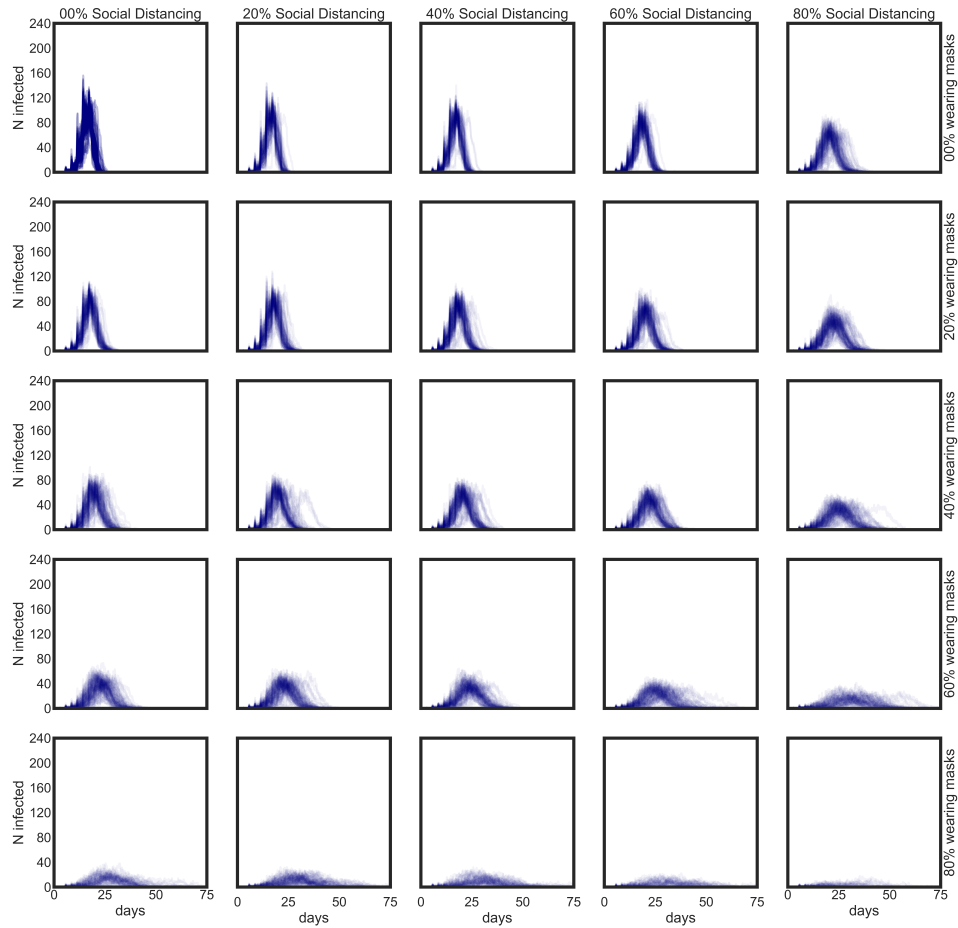
Supplementary Figure 5.4: Number of infected agents with 25 percent of asymptomatic infected population.

Number of infected agents as a function of time for all combinations of different percentage of the agent population practicing social distancing (x-axis) and wearing masks (y-axis). 100 simulations are represented for each condition and each simulation is displayed as a low-opacity trajectory over time.
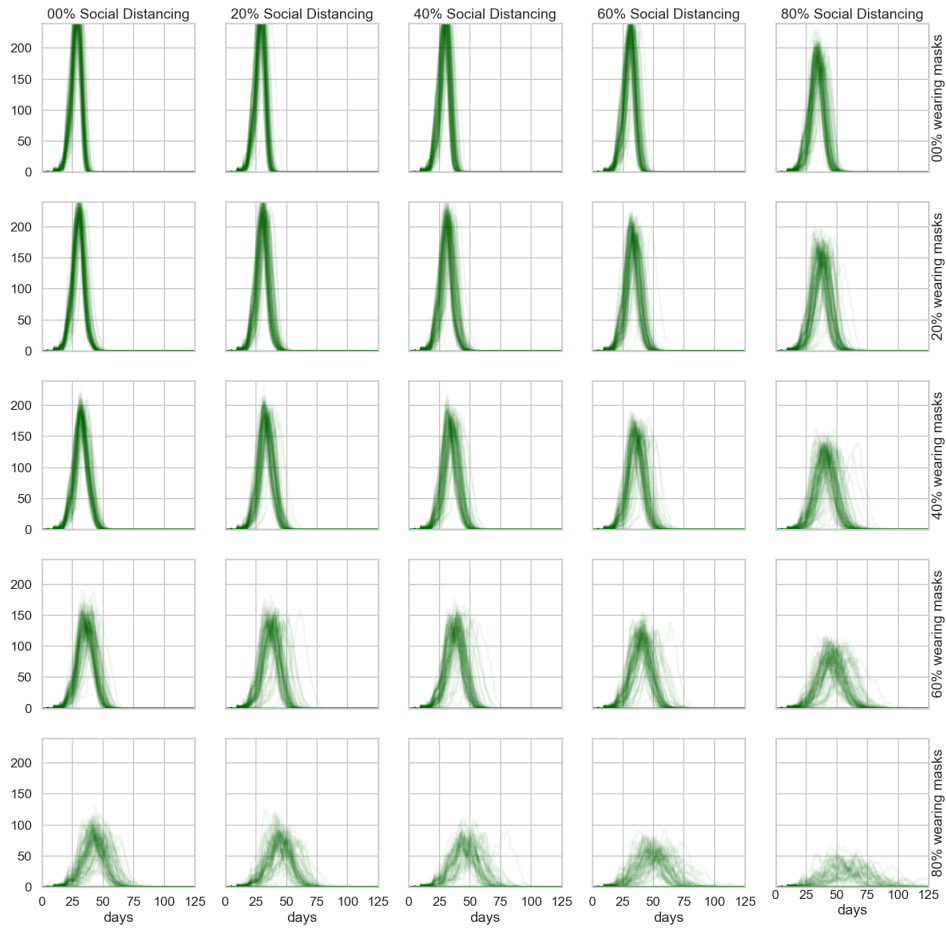
Supplementary Figure 5.5: Number of infected agents with 75 percent of asymptomatic infected population

Number of infected agents as a function of time for all combinations of different percentage of the agent population practicing social distancing (x-axis) and wearing masks (y-axis). 100 simulations are represented for each condition and each simulation is displayed as a low-opacity trajectory over time.

Chapter 6

Infectious viral shedding 1 of SARS-CoV-2 Delta following vaccination: a longitudinal cohort study

## 6.1 Abstract

Pandemic severely affected the globe. This effect manifested as a retooling and refocusing of efforts in the Andino lab to help out in the fight against the spread of COVID-19. The previous chapter was spearheaded by myself to address the importance of face-mask wearing and reducing social interactions. This chapter began as small part of a collaborative effort to measure the effectiveness of the mRNA vaccines against viral shedding. I worked closely with Michel Tassetto and Miguel Garcia-Knight to analyze data from the UCSF FIND-COVID project. This collaboration included epidemiology researchers at UCSF and the Centers for Disease Control and Prevention. The work in this chapter represents my contributions to the final paper that has been submitted and is under consideration at the time of writing. The work here is my own and represents the analysis done on data provided during this project. The manuscript *Infectious viral shedding of SARS-CoV-2 Delta following vaccination a longitudinal cohort study* has recently been submitted to *PLoS Pathogens* using the mentioned data but with slightly different data analysis.

6.2 Introduction

The Severe Acute Respiratory Syndrome Coronavirus-2 (SARS-CoV-2) vaccination is a critical tool in battling the ongoing COVID-19 pandemic[191, 17, 143]. This key public health measure is effective on reducing the rates of hospitalization yet a sizeable portion of the United States population is not yet vaccinated. The SARS-CoV-2 vaccine also plays a role in reducing the rate of shedding transmissible viral particles, and the efficacy is of great interest to not only the medical and virology community but to the world at large. Even more, the waning efficacy of the vaccine against emerging variants poses a risk to undue all the progress so far made in immunizing the world against COVID-19[116]. Of note, the Delta and Omicron variants have been shown to have high levels of vaccine-derived immune escape[40] and transmission[6]. To detect if shedding is inhibited by vaccination, many studies have used RNA detection by quantitative polymerase chain reaction (qPCR) to determine levels of key SARS-CoV-2 in the nasal passage[114]. However, the entire viral genome is not expressed equally, with fragments of different length being expressed at different levels[140]. This, along with viral RNA being cleared at higher rates in vaccinated patients suggests that the levels of infectious virus should be compared by cytopathic effect (CPE) in vaccinated and unvaccinated populations to determine viral clearance rates by vaccination status.

6.3 Results

6.3.1 Cohort data

Eighty-four participants in the following analysis were from a UCSF-based cohort study known as FIND-COVID. All participant were over eighteen, non-hospitalized, and were diagnosed with SARS-CoV-2 infection. They were also all immunocompetent and were not treated with monoclonal therapy. Of these eighty-four participant, 52 were unvaccinated (**Figure 6.1**) and 32 were vaccinated (**Figure 6.2**). The x-axis is represented in days

Figure 6.1: Unvaccinated Participant Shedding Data (Part 1)

N, E, and replicating virus per participant per day. Each graph represents the quantity of E (orange) or N (grey) viral RNA, with the day's sample containing infectious particles represented by a yellow bar.
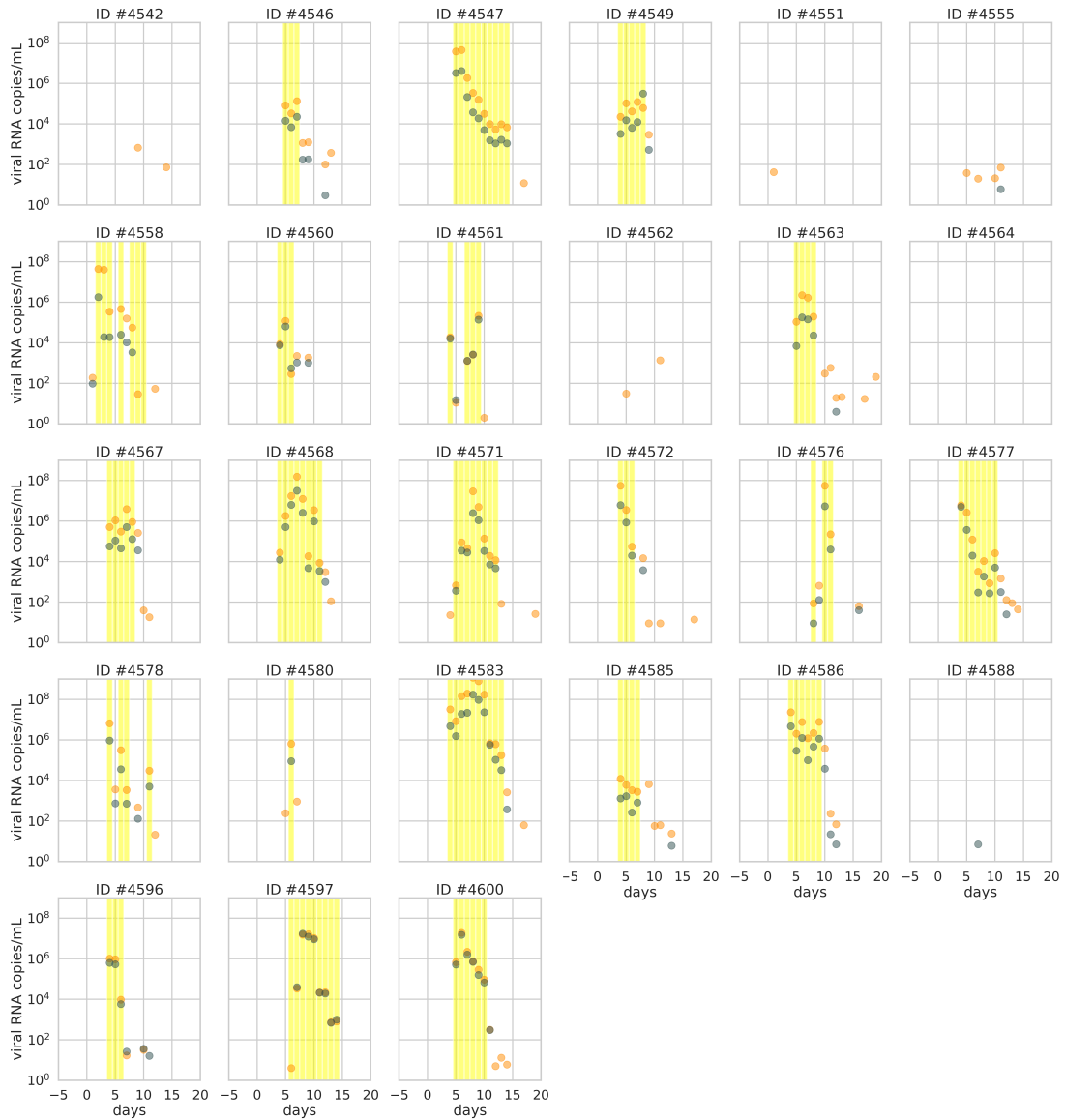
Figure 6.1: Unvaccinated Participant Shedding Data (Part 2)
N, E, and replicating virus per participant per day. Each graph represents the quantity of E (orange) or N (grey) viral RNA, with the day's sample containing infectious particles represented by a yellow bar.

post symptom onset, with day 0 being the first day that the participant reports symptoms. Patient samples are able to be collected prior to symptom onset due to the process of study recruitment, where index participants' households were invited also to participate in the study immediately after the index patient was identified to have a qPCR-positive sample. Identification numbers were created procedurally as participant were recruited to the study, with personal identifiable data anonymized in the study. As evidence by both vaccinated and unvaccinated datasets, RNA copies tend to peak around 5-7 days post-symptom onset. This indicates that viral shedding ramps up in the early days of illness and decays rapidly after peak viral replication. To further study this correlation with infectious viral particles with peak viral shedding, further analysis was performed on these data.

6.3.2 Infectious virus shedding

To investigate the correlation of infectious SARS-CoV-2 particles in shedding, each participant's sample that was positive for both nucleocapsid (N) and envelope (E) RNA was used for logistic regression (**Figure 6.3**). Briefly, the presence of CPE-positive nasal samples was turned into a binary distribution based on days post symptom onset. From this dataset a Poisson-process logistic curve was optimized for either the vaccinated or unvaccinated participants. A 95% confidence interval was also calculated for each logistic curve. The curve then serves as a probability distribution of whether an individual has infectious particles a certain number of days post symptom onset. Remarkably, the CPE data itself showed a clear division between vaccinated and unvaccinated participants in the last day that each group had a CPE-positive sample. For the unvaccinated group, the latest day a participant had a CPE-positive sample was thirteen days symptom onset, while the last CPE-positive sample was found nine days post symptom onset. This indicates that vaccinated individuals may not need to wait as long as unvaccinated individuals after positive diagnosis of COVID-19 to stop isolating.
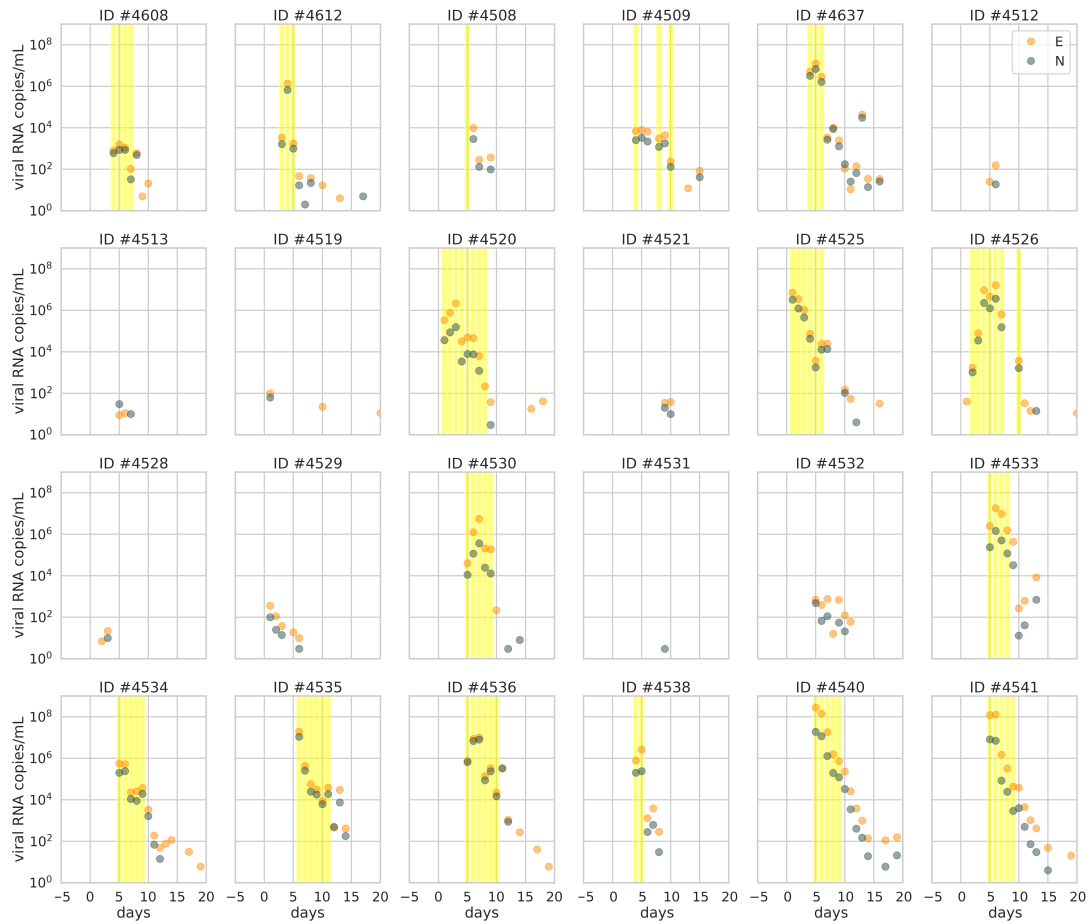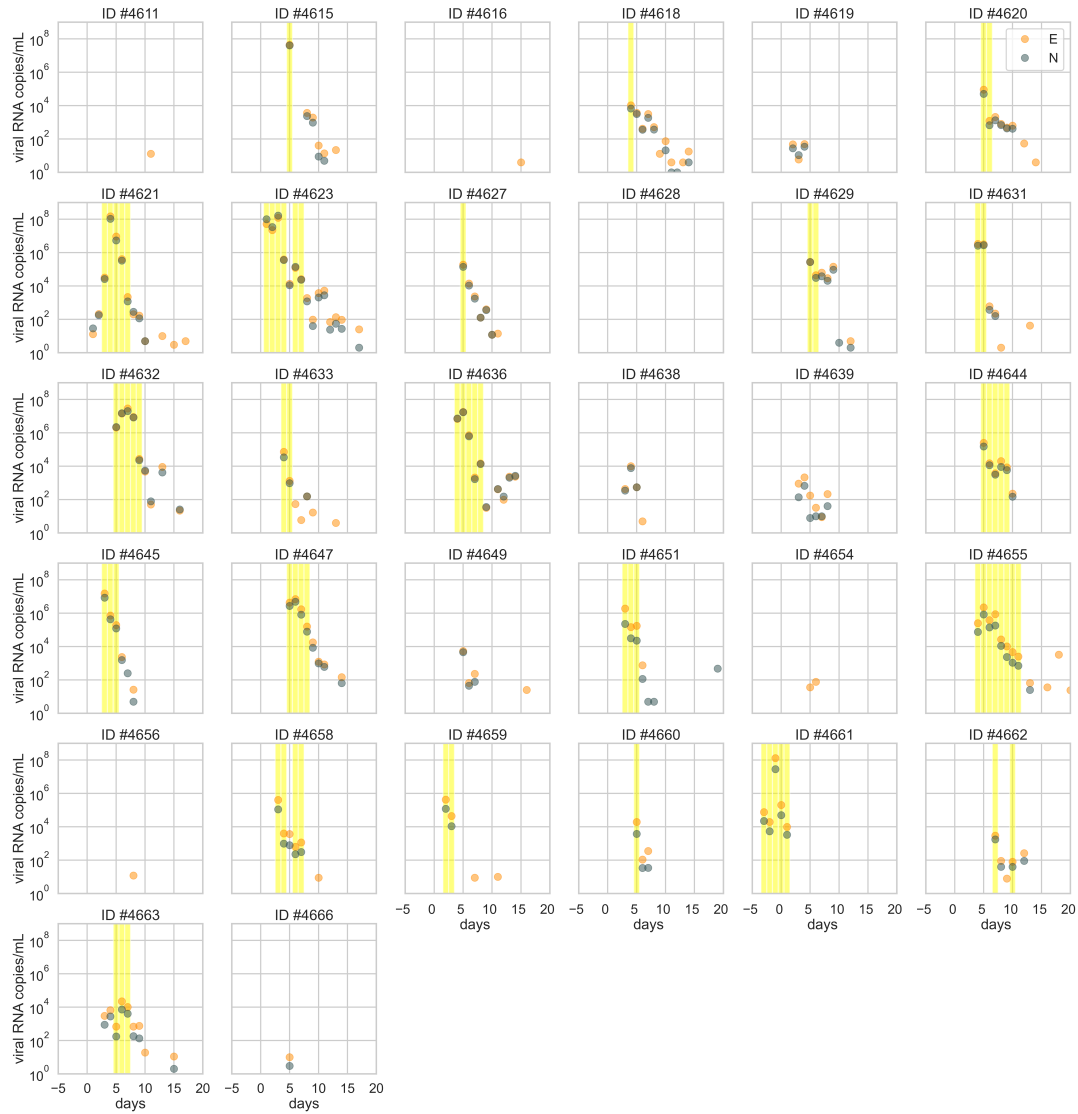
Figure 6.2: Vaccinated Participant Shedding Data
N, E, and replicating virus per participant per day. Each graph represents the quantity of E (orange) or N (grey) viral RNA, with the day's sample containing infectious particles represented by a yellow bar.
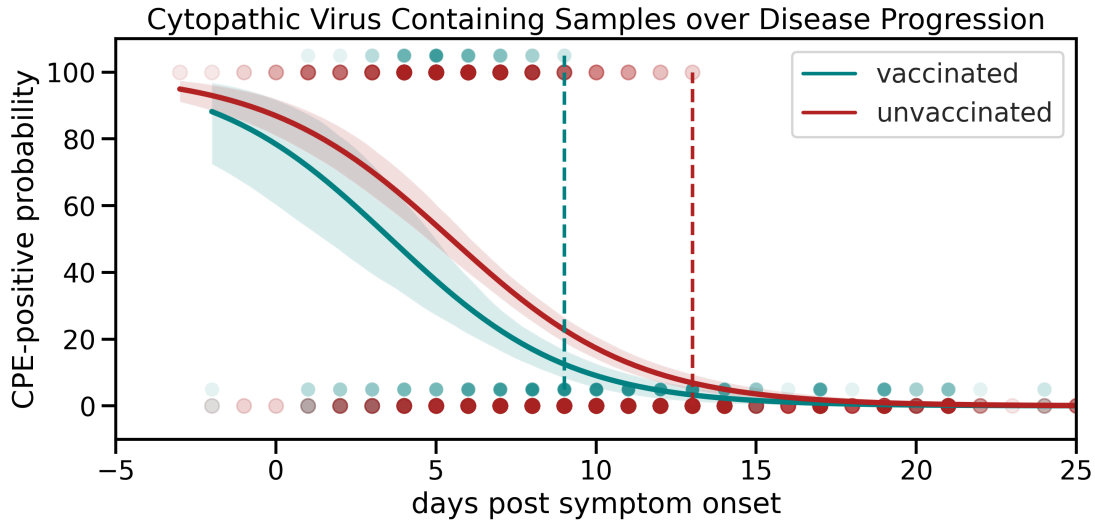
Figure 6.3: Logistic Curve for Probability of Infectious Particle Shedding
Logistic curve of CPE-inducing samples, split by vaccinated (teal) or unvaccinated (red) status. Time-points are days post symptom onset.

6.3.3 Relationship between infectious virus shedding and RNA copies

From the shedding rates of infectious SARS-CoV-2 particles represented in **Figure 6.3** it was found that vaccinated individuals had steeper, faster rates of shedding that could be also found in viral RNA measurements. This is of interest as viral RNA is the rapid diagnostic used to determine if an individual has COVID-19. To measure differences in rates of viral shedding the best measurement is by measuring CPE or virus titer by plaque assay. As this highly infectious virus can only be measured by these two methods in a high-containment biosafety level 3 (BSL3) facility, a faster measurement can be performed by RT-qPCR. Using a known copy-number standard for Orf1b, N, or E genes, the copy-number of these three genes can be measured for samples that have CPE already determined (**Figure 6.4**). This was done for either the vaccinated (teal) or unvaccinated (red) participant datasets. Logistic regression was performed between the binary CPE dataset and the quantified number of viral gene copies to determine the probability of a given number of RNA copies indicating infectious virus. As expected, no difference was found between the vaccinated or unvaccinated
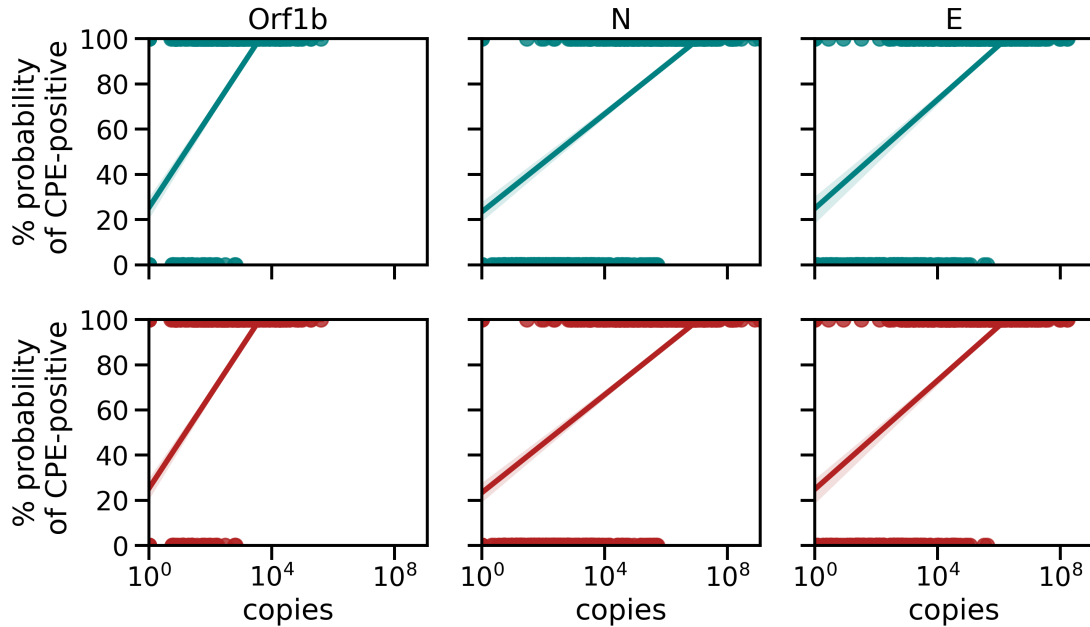
Figure 6.4: RT-qPCR as a reporter of Infectious Particle Shedding
Logistic curve between copy number of E, N, and Orf1b genes and days post symptom
onset.

dataset, with logistic curves, plotted over a logistic x-axis, for the most part matching. Both
N and E RNA measurements showed a large dynamic range of detection, with six orders
of magnitude where detection of viral RNA did not conclusively determine the presence of
infectious virus. Samples with more than one million detected copies of N and E did deter-
mine the presence of infectious virus. Orf1b showed a smaller dynamic range, with less than
4 orders of magnitude of dynamic range on the logistic curve and samples past ten-thousand
copies indicated the presence of infectious virus.

6.3.4   Decay rates of RNA

As a positive correlation between the copy number of N, E, or Orf1b RNA and the presence
of infectious virus, as measured by CPE assay, the rates of viral shedding was measured for
RNA copies. Rates of shedding copies of E was found to have similar intercepts of peak copy
number but the rates of E clearance was found to be faster for the vaccinated population

than for the unvaccinated population (**Figure 6.5.A**). On average, complete clearance of viral copies was found to occur on eleven days post peak copy number for the vaccinated population this found to be past fourteen days post peak copy number for the unvaccinated population. This relationship was altered slightly for the decay rate of N copy number (**Figure 6.5.B**). Rates of copy loss for vaccinated and unvaccinated populations were fairly similar while the peak number of copies was slightly higher for the unvaccinated population. The complete clearance of copy numbers for N followed the trend found in E, where the unvaccinated population took longer for complete clearance than the vaccinated population. However, this difference was smaller, with vaccination population occurring at day 14 post peak copy number while occurring around day 15 for the unvaccinated population. As well, many samples still had detectable copies of N up to twenty days post peak copy number for the unvaccinated population but only to fourteen days for the vaccinated population. Both of these pairs of rates of viral copy loss indicate that viral clearance is sped up in vaccinated individuals, although not by many days. Orf1b copy number was more sparsely detected in patient samples, where there were 53 and 191 Orf1b datapoints for vaccinated and unvaccinated populations, respectively, and 191 and 438 N datapoints for vaccinated and unvaccinated populations, respectively. Yet, Orf1b copy number was found to be a better reporter for infectious virus particles in participant samples (**Figure 6.4**), so rates of Orf1b copy loss was plotted (**Figure 6.5.C**). Agreeing with trends found in the decay rates of E and N, Orf1b was found to be cleared faster in vaccinated individuals than in unvaccinated individuals. These rates were plotted against each other in **Figure 6.5.D**. N was cleared at -0.27 $\pm$ 0.037 1/days in vaccinated vs. -0.25 $\pm$ 0.02 1/days in unvaccinated individuals. E was cleared at -0.30 $\pm$ 0.048 1/days in vaccinated vs. -0.25 $\pm$ 0.02 1/days in unvaccinated individuals. Finally, Orf1b was cleared at -0.286 $\pm$ 0.089 1/days in vaccinated vs -0.13 $\pm$ 0.022 1/days in unvaccinated individuals. For all three measured viral RNA copies, vaccinated individuals had a higher rate of clearance.
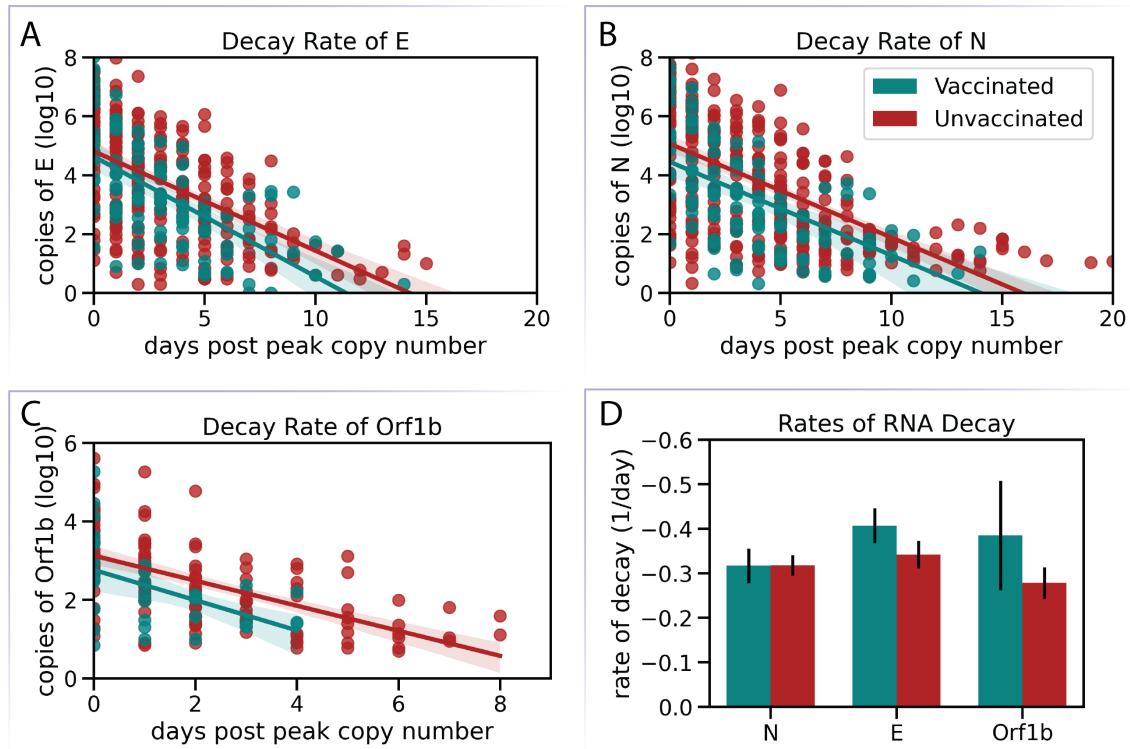
Figure 6.5: Viral RNA Shedding Rates for E, N, and Orf1b Genes
A) Rates of E-encoding RNA loss, average rates determined for vaccinated (teal) or unvaccinated (red) B) Rates of N-encoding RNA loss, average rates determined for vaccinated (teal) or unvaccinated (red) C) Rates of Orf1b-encoding RNA loss, average rates determined for vaccinated (teal) or unvaccinated (red) D) Rates of RNA loss, average rates determined for vaccinated (teal) or unvaccinated (red)

6.4 Discussion

This work demonstrates that vaccinated individuals, who have been previously shown to suffer less severe symptoms of COVID-19[100], also shed infectious, detectable virus for shorter periods of time than unvaccinated individuals. However, the effects tend to be on the order of a few days with enough standard deviation to make it unclear if vaccination status is sufficient to determine if a major change in risk of transmission is present. However, this is complicated by individuals recruited for the vaccinated dataset, as the most prevalent strain of SARS-CoV-2 at the time of sample collection was Delta, which has different infection dynamics than the original strain[121, 37, 54]. However, studies have shown that vaccination does reduce the transmission of COVID-19[102, 8, 164]. Furthermore, viral shedding of the Delta variant of COVID-19 has shown to be reduced by vaccination[144]. This agrees with the overall trend of viral shedding in the presented data. As the COVID-19 pandemic continues during the writing of this thesis there is still potential for new variants of concern to emerge. Vaccination has proven to be an effective method of reducing the number of severe cases yet the amplitude of infection waves have not decreased with increased percentages of the population being vaccinated. Further work must be done to develop novel attenuated vaccines to attempt to slow transmission[179, 101, 170].

6.5 Materials and Methods

6.5.1 Study design

Participants were part of an observational longitudinal cohort based in the San Francisco Bay Area initiated in August 2020 designed to study shedding dynamics in early infection and transmission in a household setting. Index cases (IC) were identified from individuals with a positive health provider-ordered SARS-CoV-2 nucleic acid amplification test result on a nasopharyngeal or oropharyngeal (NP/OP) specimen done at UCSF-affiliated health facilities.

ICs were recruited if they were within 5 days of symptom onset, had ¿1 household member (HM) and had no HMs with COVID-19 symptoms in the preceding week. Participants under 18 years of age and adults who were immunocompromised, hospitalized or who had received monoclonal antibody therapy, were excluded from this analysis. Participants were provided with specimen collection kits with instructions and self-collection demonstrations by study clinicians. For ICs, specimen collection was targeted for the day of enrollment (dE), daily thereafter up to day 14 and on days 17, 19, 21 and 28 post symptom onset. For HMs, daily specimen collection was targeted from dE and thereafter on the same days as the IC, counted relative to symptom onset of the IC. For all participants, symptom surveys, clinical and epidemiologic questionnaires, done either by phone or written, were completed on dE, and on days 9, 14, 21, and 28 after IC symptom onset. The type and timing of COVID-19 vaccination was verified with the vaccination card of each participant at enrollment and each subsequent survey. To be included in this analysis, vaccinated participants had to be fully vaccinated, defined as the receipt of all recommended doses (2 doses $\leq$ 28 days apart of an mRNA vaccine or 1 dose of JNJ-78436735) of a COVID-19 primary vaccine series under EUA by FDA, 14 days prior to infection or enrollment. The study was reviewed by the UCSF Institutional Review Board and given a designation of public health surveillance according to federal regulations as summarized in 45 CFR 46.102(d)(1)(2). Written informed consent was obtained from all participants.

6.5.2   Sample collection

All anterior nasal specimens were self-collected by participants. We instructed participants to rotate flocked swabs 5 times in each nostril and place in conical tubes containing 3mL of Viral Transport Medium (CDC SOP # DSR-052-03). Samples were stored in study-dedicated -20°C freezers at the participant's homes until weekly collection by the study team, at which time they were transported on dry ice for storage at -80°C. For study assays, the samples were thawed and aliquoted into screw cap microtubes. RNA extraction was done

after this initial thaw cycle and virus culture was attempted following a second freeze-thaw cycle. We performed additional testing to evaluate for infectious viral degradation between these freeze thaw cycles and did not observe any evidence of degradation.

6.5.3   RNA extraction

Automated RNA extraction was done using the KingFisher (Thermo Scientific) automated extraction instrument and compatible extraction kits in a 96 well format. $200\mu L$ of nasal samples were used for extraction with the MagMAX Viral/Pathogen Nucleic Acid Isolation Kit (Thermo Scientific) following the manufacturer's protocol and eluted into $50\mu L$ of nuclease free water. For confirmatory RT-qPCR following viral culture, RNA extraction was done using $300\mu L$ of inactivated sample (1:1 mixture of 2x RNA/DNA Shield and culture supernatant) and the Quick-DNA/RNA Viral MagBead kit (Zymo).

6.5.4   RT-qPCR assay

For each RT-qPCR reaction, $4\mu L$ of RNA sample were mixed with $5\mu L$ 2x Luna Universal Probe One-Step Reaction Mix, $0.5\mu L$ 20x WarmStart RT Enzyme Mix (NEB), $0.5\mu L$ of target gene specific forward and reverse primers and probe mix (Supp. Table 1). RT-qPCR were run for SARS-CoV2 N and E and for host mRNA, RNaseP, as a control for RNA extraction. Primers (forward and reverse) and probe concentrations in each mix used per RT-qPCR reaction were as follows: $8\mu M$ forward/reverse each and $4\mu M$ probe for E, $5.6\mu M$ forward/reverse each and $1.4\mu M$ probe for N and $4\mu M$ forward/reverse each and $1\mu M$ probe for RNaseP. Each 96 well RT-qPCR plate was run with a 10-fold serial dilution of an equal mix of plasmids containing a full copy of nucleocapsid (N) and envelope (E) genes (IDT) as an absolute standard for RNA copies calculation and primer efficiency assessment. RT-qPCR were run on a CFX Connect Real-Time PCR detection system (Biorad) with the following settings: 55°C for 10 min, 95°C for 1 min, and then cycled 40 times at 95°C for 10s followed by 60°C for 30s. Probe fluorescence was measured at the end of each cycle. All

probes, primers and standards were purchased from IDT. We defined a sample as being RNA positive if both N and E were detected at Ct ≤40. These two RNA targets were selected to optimize specificity of the PCR platform, excluding spurious RT-qPCR signals that would have been false positives. To control for the quality of self-sampling, RNAse P Ct values 2 standard deviations from the mean of all samples were repeated or excluded.

6.5.5 CPE assay

All anterior nares samples up to 14 days post symptom onset (PSO) of the index case were assayed for CPE (cytopathic effect, which is reflective of detectible infectious virus). In cases where CPE was positive within days 11-14, we continued to test samples beyond day 14 until three consecutive samples were CPE negative. CPE was assessed on Vero-hACE2-TMPRSS2 cells (gifted from A. Creanga and B. Graham at NIH) and are available from BEI Resources (NR-54970). Cells were maintained at 37°C and 5% CO2 in Dulbecco's Modified Eagle medium (DMEM; Gibco) supplemented with 10% fetal calf serum, $100\mu g/mL$ penicillin and streptomycin (Gibco) and $10\mu g/mL$ of puromycin (Gibco). The assay was adapted from Harcourt el al42 355 and done in a 96-well format. 200uL of nasal specimen were added to a well of a 96-well plate and serially diluted 1:1 with DMEM supplemented with 1X penicillin/streptomycin over two additional wells. $100\mu L$ of freshly trypsinized cells, resuspended in infection media (made as above but with 2x penicillin/streptomycin, $5\mu g/mL$ amphotericin B [Bioworld] and no puromycin) at $2.5x10^5$ cells/mL, were added to each sample dilution. Cells were cultured at 37°C and 5% CO2 and checked for CPE from day 2 to 5. Vero-hACE2-TMPRSS2 cells form characteristic syncytia upon infection with SARS-CoV-2, enabling rapid and specific visual evaluation for CPE. After 5 days of incubation, the supernatant ($200\mu L$) from one well from each dilution series was mixed 1:1 with 2x RNA/DNA Shield (Zymo) for viral inactivation and RNA extraction as described above. Among specimens with visible CPE, the presence of infectious SARS-CoV-2 was confirmed by RT-qPCR using N primers as described above. All assays were done in the

BSL3 facility at Genentech Hall, UCSF, following the study protocol that had received Biosafety Use Authorization.

6.5.6 Data Analysis

Data was collected from a shared spreadsheet with measurements for each participant for each day samples were collected. Data collected from each sample included participant ID#, days post symptom onset, CPE positivity, Ct value of N, copy number of N, Ct value of E, copy number of E, Ct value of Orf1b, and copy number of Orf1b. Other data collected was not used in this chapter's analysis. Data was tidied and read into a jupyter notebook [CITATION NEEDED, jupyter] and analyzed using a suite of python modules including `NumPy`, `Matplotlib`, `Pandas`, `Scipy.Stats`, and `StatsModels`[103, 71, 86, 127, 190, 157]. For logistic regression analysis in **Figure 6.3**, `StatsModels` was used to create a binomial regression model between CPE and days post infection. For the logistic regression in **Figure 6.4** a binomial regression model was created between CPE and copy number of N, E, or Orf1b. For the linear regression in **Figure 6.5** `Scikit.Stats` was used to estimate the average and standard deviation of the rate of N, E, and Orf1b copy loss using the least-squares method. Rate of copy loss was compared between vaccinated and unvaccinated populations by `Scikit.Stats` independent T-test.

Bibliography

[1] GPEI-nOPV2.

[2] Malawi declares polio outbreak.

[3] Matplotlib: A 2d graphics environment - IEEE journals & magazine.

[4] Mortality risk of COVID-19 - statistics and research. Library Catalog: ourworldindata.org.

[5] mwaskom/seaborn: v0.8.1 (september 2017) | zenodo.

[6] SARS-CoV-2 omicron VOC transmission in danish households | medRxiv.

[7] *et al.* A. Waterhouse. *Nucleic Acids Research*, 46:W296–W303, 2018.

[8] Emma K. Accorsi, Amadea Britton, Katherine E. Fleming-Dutra, Zachary R. Smith, Nong Shang, Gordana Derado, Joseph Miller, Stephanie J. Schrag, and Jennifer R. Verani. Association between 3 doses of mRNA COVID-19 vaccine and symptomatic infection caused by the SARS-CoV-2 omicron and delta variants. 327(7):639–651.

[9] Ashley Acevedo, Leonid Brodsky, and Raul Andino. Mutational and fitness landscapes of an RNA virus revealed through population sequencing. 505(7485):686–690. Bandiera_abtest: a Cg_type: Nature Research Journals Number: 7485 Primary_atype: Research Publisher: Nature Publishing Group Subject_term: Experimental evolution;Viral evolution Subject_term_id: experimental-evolution;viral-evolution.

[10] Oluwapelumi O. Adeyemi, Clare Nicol, Nicola J. Stonehouse, and David J. Rowlands. Increasing type 1 poliovirus capsid stability by thermal selection. 91(4):e01586–16. Publisher: American Society for Microbiology.

[11] Oluwapelumi O. Adeyemi, Lee Sherry, Joseph C. Ward, Danielle M. Pierce, Morgan R. Herod, David J. Rowlands, and Nicola J. Stonehouse. Involvement of a nonstructural protein in poliovirus capsid assembly. 93(5):e01447–18. Publisher: American Society for Microbiology.

[12] Rafael Aldabe, Angel Barco, and Luis Carrasco. Membrane permeabilization by poliovirus proteins 2b and 2bc*. 271(38):23134–23137.

[13] Gary An. Introduction of an agent-based multi-scale modular architecture for dynamic knowledge representation of acute inflammation. 5(1):11.

[14] Y. Andoh, N. Yoshii, A. Yamada, K. Fujimoto, H. Kojima, K. Mizutani, A. Nakagawa, A. Nomoto, and S. Okazaki. All-atom molecular dynamics calculation study of entire poliovirus empty capsids in solution. 141(16):165101. Publisher: American Institute of Physics.

[15] Melissa M. Arons, Kelly M. Hatfield, Sujan C. Reddy, Anne Kimball, Allison James, Jesica R. Jacobs, Joanne Taylor, Kevin Spicer, Ana C. Bardossy, Lisa P. Oakley, Sukarma Tanwar, Jonathan W. Dyal, Josh Harney, Zeshan Chisty, Jeneita M. Bell, Mark Methner, Prabasaj Paul, Christina M. Carlson, Heather P. McLaughlin, Natalie Thornburg, Suxiang Tong, Azaibi Tamin, Ying Tao, Anna Uehara, Jennifer Harcourt, Shauna Clark, Claire Brostrom-Smith, Libby C. Page, Meagan Kay, James Lewis, Patty Montgomery, Nimalie D. Stone, Thomas A. Clark, Margaret A. Honein, Jeffrey S. Duchin, and John A. Jernigan. Presymptomatic SARS-CoV-2 infections and transmission in a skilled nursing facility. 382(22):2081–2090. Publisher: Massachusetts Medical Society _eprint: https://doi.org/10.1056/NEJMoa2008457.

[16] *et al.* B. Martinez-Gualda. *J. Med. Chem.*, 63:349–368, 2020.

[17] Lindsey R. Baden, Hana M. El Sahly, Brandon Essink, Karen Kotloff, Sharon Frey, Rick Novak, David Diemert, Stephen A. Spector, Nadine Rouphael, C. Buddy Creech, John McGettigan, Shishir Khetan, Nathan Segall, Joel Solis, Adam Brosz, Carlos Fierro, Howard Schwartz, Kathleen Neuzil, Lawrence Corey, Peter Gilbert, Holly Janes, Dean Follmann, Mary Marovich, John Mascola, Laura Polakowski, Julie Ledgerwood, Barney S. Graham, Hamilton Bennett, Rolando Pajon, Conor Knightly, Brett Leav, Weiping Deng, Honghong Zhou, Shu Han, Melanie Ivarsson, Jacqueline Miller, and Tal Zaks. Efficacy and safety of the mRNA-1273 SARS-CoV-2 vaccine. 384(5):403–416. Publisher: Massachusetts Medical Society.

[18] Jim Baggen, Yue Liu, Heyrhyoung Lyoo, Arno L. W. van Vliet, Maryam Wahedi, Jost W. de Bruin, Richard W. Roberts, Pieter Overduin, Adam Meijer, Michael G. Rossmann, Hendrik Jan Thibaut, and Frank J. M. van Kuppeveld. Bypassing pan-enterovirus host factor PLA2g16. 10(1):3171. Bandiera_abtest: a Cc_license_type: cc_by Cg_type: Nature Research Journals Number: 1 Primary_atype: Research Publisher: Nature Publishing Group Subject_term: Virus–host interactions;Virus structures Subject_term_id: virus-host-interactions;virus-structures.

[19] Jim Baggen, Hendrik Jan Thibaut, Jeroen R. P. M. Strating, and Frank J. M. van Kuppeveld. The life cycle of non-polio enteroviruses and how to target it. 16(6):368–381. Number: 6 Publisher: Nature Publishing Group.

[20] Yan Bai, Lingsheng Yao, Tao Wei, Fei Tian, Dong-Yan Jin, Lijuan Chen, and Meiyun Wang. Presumed asymptomatic carrier transmission of COVID-19. 323(14):1406–1407. Publisher: American Medical Association.

[21] David Baltimore. In vitro synthesis of viral rna by the poliovirus rna polymerase*. 51(3):450–456. Publisher: Proceedings of the National Academy of Sciences.

[22] E Baranowski, C M Ruiz-Jarabo, and E Domingo. Evolution of cell recognition by viruses. *Science*, 292(5519):1102–1105, May 2001.

[23] Angel Barco, Elena Feduchi, and Luis Carrasco. Poliovirus protease 3cpro kills cells by apoptosis. 266(2):352–360.

[24] Amy L. Bauer, Catherine A.A. Beauchemin, and Alan S. Perelson. Agent-based modeling of host–pathogen systems: The successes and challenges. 179(10):1379–1389.

[25] George A. Belov and Frank J. M. van Kuppeveld. Lipid droplets grease enterovirus replication. 26(2):149–151.

[26] Erik Boehm, Ilona Kronig, Richard A. Neher, Isabella Eckerle, Pauline Vetter, Laurent Kaiser, and Geneva Centre for Emerging Viral Diseases. Novel SARS-CoV-2 variants: the pandemics within the pandemic. 27(8):1109–1117.

[27] Sanne Boersma, Huib H. Rabouw, Lucas J. M. Bruurs, Tonja Pavlovič, Arno L. W. van Vliet, Joep Beumer, Hans Clevers, Frank J. M. van Kuppeveld, and Marvin E. Tanenbaum. Translation and replication dynamics of single RNA viruses. 183(7):1930–1945.e23.

[28] Mihnea Bostina, Doryen Bubeck, Cindi Schwartz, Daniela Nicastro, David J. Filman, and James M. Hogle. Single particle cryoelectron tomography characterization of the structure and structural variability of poliovirus–receptor–membrane complex at 30Å resolution. 160(2):200–210.

[29] Lydia Bourouiba. Turbulent gas clouds and respiratory pathogen emissions: Potential implications for reducing transmission of COVID-19. 323(18):1837–1838. Publisher: American Medical Association.

[30] Elizabeth B Brickley, Ruth I Connor, Wendy Wieland-Alter, Joshua A Weiner, Margaret E Ackerman, Minetaro Arita, Chris Gast, Ilse De Coster, Pierre Van Damme,

Ananda S Bandyopadhyay, and Peter F Wright. Intestinal antibody responses to 2 novel live attenuated type 2 oral poliovirus vaccines in healthy adults in belgium. page jiaa783.

[31] Nicole C. J. Brienen, Aura Timen, Jacco Wallinga, Jim E. Van Steenbergen, and Peter F. M. Teunis. The effect of mask use on the spread of influenza during a pandemic. 30(8):1210–1218. _eprint: https://onlinelibrary.wiley.com/doi/pdf/10.1111/j.1539-6924.2010.01428.x.

[32] Diana C. Buitrago-Garcia, Dianne Egli-Gany, Michel J. Counotte, Stefanie Hossmann, Hira Imeri, Aziz Mert Ipekci, Georgia Salanti, and Nicola Low. Asymptomatic SARS-CoV-2 infections: a living systematic review and meta-analysis. page 2020.04.25.20079103. Publisher: Cold Spring Harbor Laboratory Press.

[33] Carmen Butan, David J. Filman, and James M. Hogle. Cryo-electron microscopy reconstruction shows poliovirus 135s particles poised for membrane interaction and RNA release. 88(3):1758–1770. Publisher: American Society for Microbiology.

[34] Brenno Moura Castro, Yuri de Abreu de Melo, Nicole Fernanda dos Santos, André Luiz da Costa Barcellos, Ricardo Choren, and Ronaldo Moreira Salles. Multi-agent simulation model for the evaluation of COVID-19 transmission. 136:104645.

[35] Jasper Fuk-Woo Chan, Shuofeng Yuan, Anna Jinxia Zhang, Vincent Kwok-Man Poon, Chris Chung-Sing Chan, Andrew Chak-Yiu Lee, Zhimeng Fan, Can Li, Ronghui Liang, Jianli Cao, Kaiming Tang, Cuiting Luo, Vincent Chi-Chung Cheng, Jian-Piao Cai, Hin Chu, Kwok-Hung Chan, Kelvin Kai-Wang To, Siddharth Sridhar, and Kwok-Yung Yuen. Surgical mask partition reduces the risk of noncontact transmission in a golden syrian hamster model for coronavirus disease 2019 (COVID-19). 71(16):2139–2149.

[36] Sheryl L. Chang, Nathan Harding, Cameron Zachreson, Oliver M. Cliff, and Mikhail Prokopenko. Modelling transmission and control of the COVID-19 pandemic in australia.

[37] Paul A. Christensen, Randall J. Olsen, S. Wesley Long, Sishir Subedi, James J. Davis, Parsa Hodjat, Debbie R. Walley, Jacob C. Kinskey, Matthew Ojeda Saavedra, Layne Pruitt, Kristina Reppond, Madison N. Shyer, Jessica Cambric, Ryan Gadd, Rashi M. Thakur, Akanksha Batajoo, Regan Mangham, Sindy Pena, Trina Trinh, Prasanti Yerramilli, Marcus Nguyen, Robert Olson, Richard Snehal, Jimmy Gollihar, and James M. Musser. Delta variants of SARS-CoV-2 cause significantly increased vaccine breakthrough COVID-19 cases in houston, texas. 192(2):320–331.

[38] Sara Cline. Cases at seafood plant cause spike in oregon COVID numbers | news break. Library Catalog: www.newsbreak.com.

[39] Charles N. Cole, Donna Smoler, Eckard Wimmer, and David Baltimore. Defective interfering particles of poliovirus i. isolation and physical properties. 7(4):478–485. Publisher: American Society for Microbiology.

[40] Shirley Collie, Jared Champion, Harry Moultrie, Linda-Gail Bekker, and Glenda Gray. Effectiveness of BNT162b2 vaccine against omicron variant in south africa. 386(5):494–496. Publisher: Massachusetts Medical Society.

[41] Karen S. Conrad, Ting-Wen Cheng, Daniel Ysselstein, Saskia Heybrock, Lise R. Hoth, Boris A. Chrunyk, Christopher W. am Ende, Dimitri Krainc, Michael Schwake, Paul Saftig, Shenping Liu, Xiayang Qiu, and Michael D. Ehlers. Lysosomal integral membrane protein-2 as a phospholipid receptor revealed by biophysical and cellular studies. 8(1):1908. Bandiera_abtest: a Cc_license_type: cc_by Cg_type: Nature Research Journals Number: 1 Primary_atype: Research Publisher: Nature Publishing Group Sub-

ject_term: Membrane trafficking;X-ray crystallography Subject_term_id: membrane-trafficking;x-ray-crystallography.

[42] Kizzmekia S Corbett, Darin K Edwards, Sarah R Leist, Olubukola M Abiona, Seyhan Boyoglu-Barnum, Rebecca A Gillespie, Sunny Himansu, Alexandra Schäfer, Cynthia T Ziwawo, Anthony T DiPiazza, and et al. Sars-cov-2 mrna vaccine design enabled by prototype pathogen preparedness. *Nature*, 586:567–571, Oct 2020.

[43] T. Couderc, F. Delpeyroux, H. Le Blay, and B. Blondel. Mouse adaptation determinants of poliovirus type 1 enhance viral uncoating. 70(1):305–312.

[44] H. R. Cox, V. J. Cabasso, F. S. Markham, M. J. Moses, A. W. Moyer, M. Roca-Garcia, and J. M. Ruegsegger. Immunological response to trivalent oral poliomyelitis vaccine. 2(5152):591–597.

[45] Shane Crotty and Raul Andino. Implications of high RNA virus mutation rates: lethal mutagenesis and the antiviral drug ribavirin. 4(13):1301–1307.

[46] Minghao Dang, Xiangxi Wang, Quan Wang, Yaxin Wang, Jianping Lin, Yuna Sun, Xuemei Li, Liguo Zhang, Zhiyong Lou, Junzhi Wang, and Zihe Rao. Molecular mechanism of SCARB2-mediated attachment and uncoating of EV71. 5(9):692–703.

[47] Michael Day. Covid-19: four fifths of cases are asymptomatic, china figures indicate. 369. Publisher: British Medical Journal Publishing Group Section: News.

[48] Stephen B. Deitz, Dana A. Dodd, Stewart Cooper, Peter Parham, and Karla Kirkegaard. MHC i-dependent antigen presentation is inhibited by poliovirus protein 3a. 97(25):13790–13795. Publisher: Proceedings of the National Academy of Sciences.

[49] Francesco Di Gennaro, Damiano Pizzol, Claudia Marotta, Mario Antunes, Vincenzo Racalbuto, Nicola Veronese, and Lee Smith. Coronavirus diseases (COVID-19) current

147

status and future perspectives: A narrative review. 17(8):2690. Number: 8 Publisher: Multidisciplinary Digital Publishing Institute.

[50] Ken A. Dill and Sarina Bromberg. *Molecular Driving Forces: Statistical Thermodynamics in Chemistry and Biology.* Garland Science. Google-Books-ID: hdeODhjp1bUC.

[51] Dimiter S Dimitrov. Virus entry: molecular mechanisms and biomedical applications. *Nature Reviews. Microbiology*, 2(2):109–122, Feb 2004.

[52] Stuart Dowall, Francisco J. Salguero, Nathan Wiblin, Susan Fotheringham, Graham Hatch, Simon Parks, Kathryn Gowan, Debbie Harris, Oliver Carnell, Rachel Fell, Robert Watson, Victoria Graham, Karen Gooch, Yper Hall, Simon Mizen, and Roger Hewson. Development of a hamster natural transmission model of SARS-CoV-2 infection. 13(11):2251. Number: 11 Publisher: Multidisciplinary Digital Publishing Institute.

[53] R. Dulbecco and Marguerite Vogt. PLAQUE FORMATION AND ISOLATION OF PURE LINES WITH POLIOMYELITIS VIRUSES. 99(2):167–182.

[54] David W. Eyre, Donald Taylor, Mark Purver, David Chapman, Tom Fowler, Koen B. Pouwels, A. Sarah Walker, and Tim E.A. Peto. Effect of covid-19 vaccination on transmission of alpha and delta variants. 386(8):744–756. Publisher: Massachusetts Medical Society.

[55] R. J. Fallon. SEROLOGICAL EPIDEMIOLOGY OF POLIOMYELITIS: DISTRIBUTION OF IMMUNITY TO POLIOMYELITIS VIRUS. 267(6907):65–69.

[56] Wenchun Fan, Katrina B. Mar, Levent Sari, Ilona K. Gaszek, Qiang Cheng, Bret M. Evers, John M. Shelton, Mary Wight-Carter, Daniel J. Siegwart, Milo M. Lin, and John W. Schoggins. TRIM7 inhibits enterovirus replication and promotes emergence of a viral variant with increased pathogenicity. 184(13):3410–3425.e17.

[57] Georges Feller. Protein stability and enzyme activity at extreme biological temperatures. 22(32):323101.

[58] Shuo Feng, Chen Shen, Nan Xia, Wei Song, Mengzhen Fan, and Benjamin J. Cowling. Rational use of face masks in the COVID-19 pandemic. 8(5):434–436. Publisher: Elsevier.

[59] Neil Ferguson, Daniel Laydon, Gemma Nedjati-Gilani, Natsuko Imai, Kylie Ainslie, Marc Baguelin, Sangeeta Bhatia, Adhiratha Boonyasiri, Zulma Cucunubá, Gina Cuomo-Dannenburg, Amy Dighe, Ilaria Dorigatti, Han Fu, Katy Gaythorpe, Will Green, Arran Hamlet, Wes Hinsley, Lucy C Okell, Sabine van Elsland, Hayley Thompson, Robert Verity, Eric Volz, Haowei Wang, Yuanrong Wang, Patrick GT Walker, Caroline Walters, Peter Winskill, Charles Whittaker, Christl A Donnelly, Steven Riley, and Azra C Ghani. Impact of non-pharmaceutical interventions (NPIs) to reduce COVID-19 mortality and healthcare demand.

[60] Marisa Fernandez. WHO: Data suggests it's "very rare" for coronavirus to spread through asymptomatics. Library Catalog: www.axios.com.

[61] M P Fox, M J Otto, and M A McKinlay. Prevention of rhinovirus and poliovirus uncoating by WIN 51711, a new antiviral drug. 30(1):110–116. Publisher: American Society for Microbiology.

[62] D. J. Tobias G. J. Martyna and M. L. Klein. *J. Chem. Phys.*, 101:4177–4189, 1994.

[63] S. Gard. Studies in the epidemiology of poliomyelitis. i. on the theory of pooling of specimens in mass investigations. 5(2):110–120.

[64] Derek Gatherer and AlainYR 2016 Kohl. Zika virus: a previously slow pandemic spreads rapidly through the americas. 97(2):269–273. Publisher: Microbiology Society,.

[65] Ron Geller, Sebastian Pechmann, Ashley Acevedo, Raul Andino, and Judith Frydman. Hsp90 shapes protein and RNA evolution to balance trade-offs between protein stability and aggregation. 9(1):1781. Bandiera_abtest: a Cc_license_type: cc_by Cg_type: Nature Research Journals Number: 1 Primary_atype: Research Publisher: Nature Publishing Group Subject_term: Biochemistry;Computational biology and bioinformatics;Virology Subject_term_id: biochemistry;computational-biology-and-bioinformatics;virology.

[66] Peng Gong and Olve B. Peersen. Structural basis for active site closure by the poliovirus RNA-dependent RNA polymerase. 107(52):22505–22510. Publisher: Proceedings of the National Academy of Sciences.

[67] Mariam Bernadette González-Hernández, Jeffrey William Perry, and Christiane E. Wobus. Neutral red assay for murine norovirus replication and detection in a mouse. 3(7):e415.

[68] António Grilo, Artur Caetano, and Agostinho Rosa. Agent based artificial immune system. page 7.

[69] Daniel F. Gudbjartsson, Agnar Helgason, Hakon Jonsson, Olafur T. Magnusson, Pall Melsted, Gudmundur L. Norddahl, Jona Saemundsdottir, Asgeir Sigurdsson, Patrick Sulem, Arna B. Agustsdottir, Berglind Eiriksdottir, Run Fridriksdottir, Elisabet E. Gardarsdottir, Gudmundur Georgsson, Olafia S. Gretarsdottir, Kjartan R. Gudmundsson, Thora R. Gunnarsdottir, Arnaldur Gylfason, Hilma Holm, Brynjar O. Jensson, Aslaug Jonasdottir, Frosti Jonsson, Kamilla S. Josefsdottir, Thordur Kristjansson, Droplaug N. Magnusdottir, Louise le Roux, Gudrun Sigmundsdottir, Gardar Sveinbjornsson, Kristin E. Sveinsdottir, Maney Sveinsdottir, Emil A. Thorarensen, Bjarni Thorbjornsson, Arthur Löve, Gisli Masson, Ingileif Jonsdottir, Alma D. Möller, Thorolfur Gudnason, Karl G. Kristinsson, Unnur Thorsteinsdottir, and Kari Stefansson.

Spread of SARS-CoV-2 in the icelandic population. 382(24):2302–2315. Publisher: Massachusetts Medical Society _eprint: https://doi.org/10.1056/NEJMoa2006100.

[70] A. Windemuth H. Grubmüller, H. Heller and K. Schulten. *Mol. Simul.*, 6:121–142, 1991.

[71] Charles R. Harris, K. Jarrod Millman, Stéfan J. van der Walt, Ralf Gommers, Pauli Virtanen, David Cournapeau, Eric Wieser, Julian Taylor, Sebastian Berg, Nathaniel J. Smith, Robert Kern, Matti Picus, Stephan Hoyer, Marten H. van Kerkwijk, Matthew Brett, Allan Haldane, Jaime Fernández del Río, Mark Wiebe, Pearu Peterson, Pierre Gérard-Marchant, Kevin Sheppard, Tyler Reddy, Warren Weckesser, Hameer Abbasi, Christoph Gohlke, and Travis E. Oliphant. Array programming with NumPy. 585(7825):357–362. Number: 7825 Publisher: Nature Publishing Group.

[72] Andrew G. Harrison, Tao Lin, and Penghua Wang. Mechanisms of SARS-CoV-2 transmission and pathogenesis. 41(12):1100–1115.

[73] Xi He, Eric H. Y. Lau, Peng Wu, Xilong Deng, Jian Wang, Xinxin Hao, Yiu Chung Lau, Jessica Y. Wong, Yujuan Guan, Xinghua Tan, Xiaoneng Mo, Yanqing Chen, Baolin Liao, Weilie Chen, Fengyu Hu, Qing Zhang, Mingqiu Zhong, Yanrong Wu, Lingzhai Zhao, Fuchun Zhang, Benjamin J. Cowling, Fang Li, and Gabriel M. Leung. Temporal dynamics in viral shedding and transmissibility of COVID-19. pages 1–4. Publisher: Nature Publishing Group.

[74] Nagendra R. Hegde, Mohan S. Maddur, Pavuluri Panduranga Rao, Srini V. Kaveri, and Jagadeesh Bayry. Thermostable foot-and-mouth disease virus as a vaccine candidate for endemic countries: a perspective. 27(16):2199–2201.

[75] C. U. Hellen and E. Wimmer. Maturation of poliovirus capsid proteins. 187(2):391–397.

[76] Joel Hellewell, Sam Abbott, Amy Gimma, Nikos I Bosse, Christopher I Jarvis, Timothy W Russell, James D Munday, Adam J Kucharski, W John Edmunds, Fiona Sun, Stefan Flasche, Billy J Quilty, Nicholas Davies, Yang Liu, Samuel Clifford, Petra Klepac, Mark Jit, Charlie Diamond, Hamish Gibbs, Kevin van Zandvoort, Sebastian Funk, and Rosalind M Eggo. Feasibility of controlling COVID-19 outbreaks by isolation of cases and contacts. 8(4):e488–e496.

[77] Nicolas Hoertel, Martin Blachier, Carlos Blanco, Mark Olfson, Marc Massetti, Marina Sánchez Rico, Frédéric Limosin, and Henri Leleu. A stochastic agent-based model of the SARS-CoV-2 epidemic in france. 26(9):1417–1421. Number: 9 Publisher: Nature Publishing Group.

[78] Markus Hoffmann, Nadine Krüger, Sebastian Schulz, Anne Cossmann, Cheila Rocha, Amy Kempf, Inga Nehlmeier, Luise Graichen, Anna-Sophie Moldenhauer, Martin S. Winkler, Martin Lier, Alexandra Dopfer-Jablonka, Hans-Martin Jäck, Georg M. N. Behrens, and Stefan Pöhlmann. The omicron variant is highly resistant against antibody-mediated neutralization: Implications for control of the COVID-19 pandemic. 185(3):447–456.e11.

[79] J. M. Hogle, M. Chow, and D. J. Filman. Three-dimensional structure of poliovirus at 2.9 a resolution. 229(4720):1358–1365.

[80] Jeremy Howard, Austin Huang, Zhiyuan Li, Zeynep Tufekci, Vladimir Zdimal, Helene-Mari van der Westhuizen, Arne von Delft, Amy Price, Lex Fridman, Lei-Han Tang, Viola Tang, Gregory L. Watson, Christina E. Bax, Reshama Shaikh, Frederik Questier, Danny Hernandez, Larry F. Chu, Christina M. Ramirez, and Anne W. Rimoin. Face masks against COVID-19: An evidence review. Publisher: Preprints.

[81] Yang Hsia, Jacob B Bale, Shane Gonen, Dan Shi, William Sheffler, Kimberly K Fong, Una Nattermann, Chunfu Xu, Po-Ssu Huang, Rashmi Ravichandran, and

et al. Design of a hyperstable 60-subunit protein dodecahedron. [corrected]. *Nature*, 535(7610):136–139, Jul 2016.

[82] Ben Hu, Hua Guo, Peng Zhou, and Zheng-Li Shi. Characteristics of SARS-CoV-2 and COVID-19. pages 1–14.

[83] Lihong Huang and Jianbo Yue. The interplay of autophagy and enterovirus. 101:12–19.

[84] Yan Huang, James M. Hogle, and Marie Chow. Is the 135s poliovirus particle an intermediate during cell entry? 74(18):8757–8761. Publisher: American Society for Microbiology.

[85] W. Humphrey, A. Dalke, and K. Schulten. *J. Mol. Graph.*, 14:33–38, 1996.

[86] John D. Hunter. Matplotlib: A 2d graphics environment. 9(3):90–95. Conference Name: Computing in Science Engineering.

[87] Khairunnisa' Mohamed Hussain, Kim Lian Janet Leong, Mary Mah-Lee Ng, and Justin Jang Hann Chu. The essential role of clathrin-mediated endocytosis in the infectious entry of human enterovirus 71*. 286(1):309–321.

[88] Alvin Ing, Christine Cocks, and Jeffery Peter Green. COVID-19: in the footsteps of ernest shackleton | thorax.

[89] Alicia Irurzun and Luis Carrasco. Entry of poliovirus into cells is blocked by valino-mycin and concanamycin a. 40(12):3589–3600. Publisher: American Chemical Society.

[90] *et al.* J. Huang. *Nat. Methods*, 14:71–73, 2017.

[91] G. Ciccotti J.-P.Ryckaert and H. J. C. Berendsen. *J. Comput. Phys.*, 23:327–341, 1977.

[92] *et al.* J.C. Phillips. *J. Comput. Chem.*, 26:1781–1802, 2005.

[93] *et al.* J.C. Phillips. *J. Chem. Phys.*, 153:044130, 2020.

[94] Ping Jiang, Ying Liu, Hsin-Chieh Ma, Aniko V. Paul, and Eckard Wimmer. Picornavirus morphogenesis. 78(3):418–437. Publisher: American Society for Microbiology.

[95] Yuefei Jin, Tiantian Sun, Guangyuan Zhou, Dong Li, Shuaiyin Chen, Weiguo Zhang, Xueyuan Li, Rongguang Zhang, Haiyan Yang, and Guangcai Duan. Pathogenesis study of enterovirus 71 using a novel human SCARB2 knock-in mouse model. 6(2):e01048–20. Publisher: American Society for Microbiology.

[96] Richard T. Johnson. Pathogenesis of poliovirus infections. 753(1):361–365. _eprint: https://onlinelibrary.wiley.com/doi/pdf/10.1111/j.1749-6632.1995.tb27562.x.

[97] De Kai, Guy-Philippe Goldstein, Alexey Morgunov, Vishal Nangalia, and Anna Rotkirch. Universal masking is urgent in the COVID-19 pandemic: SEIR and agent based models, empirical validation, policy recommendations.

[98] De Kai, Guy-Philippe Goldstein, Alexey Morgunov, Vishal Nangalia, and Anna Rotkirch. Universal masking is urgent in the COVID-19 pandemic: SEIR and agent based models, empirical validation, policy recommendations.

[99] Jun Kang, Zheng Pang, Zhenwei Zhou, Xianhuang Li, Sihua Liu, Jinyan Cheng, Peiyuan Liu, Wenjie Tan, Zhiyun Wang, and Tao Wang. Enterovirus d68 protease 2apro targets TRAF3 to subvert host innate immune responses. 95(3):e01856–20. Publisher: American Society for Microbiology.

[100] Srinivasa Vittal Katikireddi, Thiago Cerqueira-Silva, Eleftheria Vasileiou, Chris Robertson, Sarah Amele, Jiafeng Pan, Bob Taylor, Viviane Boaventura, Guilherme Loureiro Werneck, Renzo Flores-Ortiz, Utkarsh Agrawal, Annemarie B Docherty, Colin McCowan, Jim McMenamin, Emily Moore, Lewis D Ritchie, Igor Rudan, Syed Ahmar Shah, Ting Shi, Colin R Simpson, Mauricio L Barreto, Vinicius de Araujo Oliveira, Manoel Barral-Netto, and Aziz Sheikh. Two-dose ChAdOx1 nCoV-

19 vaccine protection against COVID-19 hospital admissions and deaths over time: a retrospective, population-based cohort study in scotland and brazil. 399(10319):25–35.

[101] Young-Il Kim, Dokyun Kim, Kwang-Min Yu, Hogyu David Seo, Shin-Ae Lee, Mark Anthony B. Casel, Seung-Gyu Jang, Stephanie Kim, WooRam Jung, Chih-Jen Lai, Young Ki Choi, and Jae U. Jung. Development of spike receptor-binding domain nanoparticles as a vaccine candidate against SARS-CoV-2 infection in ferrets. 12(2):e00230–21. Publisher: American Society for Microbiology.

[102] Stephen M. Kissler, Joseph R. Fauver, Christina Mack, Caroline G. Tai, Mallery I. Breban, Anne E. Watkins, Radhika M. Samant, Deverick J. Anderson, Jessica Metti, Gaurav Khullar, Rachel Baits, Matthew MacKay, Daisy Salgado, Tim Baker, Joel T. Dudley, Christopher E. Mason, David D. Ho, Nathan D. Grubaugh, and Yonatan H. Grad. Viral dynamics of SARS-CoV-2 variants in vaccinated and unvaccinated persons. 385(26):2489–2491. Publisher: Massachusetts Medical Society.

[103] T. Kluyver, B. Ragan-Kelley, Fernando Pérez, B. Granger, Matthias Bussonnier, J. Frederic, Kyle Kelley, Jessica B. Hamrick, J. Grout, S. Corlay, Paul Ivanov, Damián Avila, Safia Abdalla, Carol Willing, and Jupyter Development Team. Jupyter notebooks - a publishing format for reproducible computational workflows. In *ELPUB*.

[104] Kyousuke Kobayashi and Satoshi Koike. Cellular receptors for enterovirus a71. 27(1):23.

[105] Abhiteja Konda, Abhinav Prakash, Gregory A. Moss, Michael Schmoldt, Gregory D. Grant, and Supratik Guha. Aerosol filtration efficiency of common fabrics used in respiratory cloth masks. 14(5):6339–6347. Publisher: American Chemical Society.

[106] Jennifer L. Konopka-Anstadt, Ray Campagnoli, Annelet Vincent, Jing Shaw, Ling Wei, Nhien T. Wynn, Shane E. Smithee, Erika Bujaki, Ming Te Yeh, Majid Laassri, Tatiana Zagorodnyaya, Amy J. Weiner, Konstantin Chumakov, Raul Andino, Andrew

Macadam, Olen Kew, and Cara C. Burns. Development of a new oral poliovirus vaccine for the eradication end game using codon deoptimization. 5(1):1–9. Number: 1 Publisher: Nature Publishing Group.

[107] Thomas G. Ksiazek, Dean Erdman, Cynthia S. Goldsmith, Sherif R. Zaki, Teresa Peret, Shannon Emery, Suxiang Tong, Carlo Urbani, James A. Comer, Wilina Lim, Pierre E. Rollin, Scott F. Dowell, Ai-Ee Ling, Charles D. Humphrey, Wun-Ju Shieh, Jeannette Guarner, Christopher D. Paddock, Paul Rota, Barry Fields, Joseph DeRisi, Jyh-Yuan Yang, Nancy Cox, James M. Hughes, James W. LeDuc, William J. Bellini, and Larry J. Anderson. A novel coronavirus associated with severe acute respiratory syndrome. 348(20):1953–1966. Publisher: Massachusetts Medical Society.

[108] S. Kuge, I. Saito, and A. Nomoto. Primary structure of poliovirus defective-interfering particle genomes and possible generation mechanisms of the particles. 192(3):473–487.

[109] Toshikazu Kuniya. Prediction of the epidemic peak of coronavirus disease in japan, 2020. 9(3):789. Number: 3 Publisher: Multidisciplinary Digital Publishing Institute.

[110] Barry J. Lamphear and Robert E. Rhoads. A single amino acid change in protein synthesis initiation factor 4g renders cap-dependent translation resistant to picornaviral 2a proteases. 35(49):15726–15733. Publisher: American Chemical Society.

[111] Orly Laufman, John Perrino, and Raul Andino. Viral generated inter-organelle contacts redirect lipid flux for genome replication. 178(2):275–289.e16.

[112] Ha Youn Lee, David J. Topham, Sung Yong Park, Joseph Hollenbaugh, John Treanor, Tim R. Mosmann, Xia Jin, Brian M. Ward, Hongyu Miao, Jeanne Holden-Wiltse, Alan S. Perelson, Martin Zand, and Hulin Wu. Simulation and prediction of the adaptive immune response to influenza a virus infection. 83(14):7151–7165.

[113] Nancy H. L. Leung, Daniel K. W. Chu, Eunice Y. C. Shiu, Kwok-Hung Chan, James J. McDevitt, Benien J. P. Hau, Hui-Ling Yen, Yuguo Li, Dennis K. M. Ip, J. S. Ma-

lik Peiris, Wing-Hong Seto, Gabriel M. Leung, Donald K. Milton, and Benjamin J. Cowling. Respiratory virus shedding in exhaled breath and efficacy of face masks. 26(5):676–680. Number: 5 Publisher: Nature Publishing Group.

[114] Matan Levine-Tiefenbrun, Idan Yelin, Hillel Alapi, Rachel Katz, Esma Herzel, Jacob Kuint, Gabriel Chodick, Sivan Gazit, Tal Patalon, and Roy Kishony. Viral loads of delta-variant SARS-CoV-2 breakthrough infections after vaccination and booster with BNT162b2. 27(12):2108–2110. Number: 12 Publisher: Nature Publishing Group.

[115] Mingming Liang, Liang Gao, Ce Cheng, Qin Zhou, John Patrick Uy, Kurt Heiner, and Chenyu Sun. Efficacy of face mask in preventing respiratory virus transmission: A systematic review and meta-analysis. page 101751.

[116] Dan-Yu Lin, Donglin Zeng, and Peter B Gilbert. Evaluating the long-term efficacy of coronavirus disease 2019 (COVID-19) vaccines. 73(10):1927–1939.

[117] Lin Liu. Fields virology, 6th edition. 59(4):613.

[118] Yue Liu, Ju Sheng, Andrei Fokine, Geng Meng, Woong-Hee Shin, Feng Long, Richard J. Kuhn, Daisuke Kihara, and Michael G. Rossmann. Structure and inhibition of EV-d68, a virus that causes respiratory illness in children. 347(6217):71–74. Publisher: American Association for the Advancement of Science.

[119] Yue Liu, Ju Sheng, Arno L. W. van Vliet, Geeta Buda, Frank J. M. van Kuppeveld, and Michael G. Rossmann. Molecular basis for the acid-initiated uncoating of human enterovirus d68. 115(52):E12209–E12217. Publisher: Proceedings of the National Academy of Sciences.

[120] M. Longson. Coxsackie virus heart diseases. 3(5617):555–556.

[121] Jamie Lopez Bernal, Nick Andrews, Charlotte Gower, Eileen Gallagher, Ruth Simmons, Simon Thelwall, Julia Stowe, Elise Tessier, Natalie Groves, Gavin Dabrera,

Richard Myers, Colin N.J. Campbell, Gayatri Amirthalingam, Matt Edmunds, Maria Zambon, Kevin E. Brown, Susan Hopkins, Meera Chand, and Mary Ramsay. Effectiveness of covid-19 vaccines against the b.1.617.2 (delta) variant. 385(7):585–594. Publisher: Massachusetts Medical Society.

[122] Honglin Luo. Interplay between the virus and the ubiquitin-proteasome system: molecular mechanism of viral pathogenesis. 17:1–10.

[123] S. Bianco R. Andino M.-T. Yehm S. Capponi, A. Catching. *Viruses*, 12:867, 2020.

[124] Navid Mahdizadeh Gharakhanlou and Navid Hooshangi. Spatio-temporal simulation of the novel coronavirus (COVID-19) outbreak using the agent-based modeling approach (case study: Urmia, iran). 20:100403.

[125] Laura L. Marcotte, Amanda B. Wass, David W. Gohara, Harsh B. Pathak, Jamie J. Arnold, David J. Filman, Craig E. Cameron, and James M. Hogle. Crystal structure of poliovirus 3cd protein: Virally encoded protease and precursor to the RNA-dependent RNA polymerase. 81(7):3583–3596. Publisher: American Society for Microbiology.

[126] Luis Martínez-Gil, Manuel Bañó-Polo, Natalia Redondo, Silvia Sánchez-Martínez, José Luis Nieva, Luis Carrasco, and Ismael Mingarro. Membrane integration of poliovirus 2b viroporin. 85(21):11315–11324. Publisher: American Society for Microbiology.

[127] Wes Mckinney. Data structures for statistical computing in python.

[128] Kevin Messacar, Emily Spence-Davizon, Christina Osborne, Craig Press, Teri L Schreiner, Jan Martin, Ricka Messer, John Maloney, Alexis Burakoff, Meghan Barnes, Shannon Rogers, Adriana S Lopez, Janell Routh, Susan I Gerber, M Steven Oberste, W Allan Nix, Mark J Abzug, Kenneth L Tyler, Rachel Herlihy, and Samuel R Dominguez. Clinical characteristics of enterovirus a71 neurological disease during

an outbreak in children in colorado, USA, in 2018: an observational cohort study. 20(2):230–239.

[129] Ian F. Miller, Alexander D. Becker, Bryan T. Grenfell, and C. Jessica E. Metcalf. Disease and healthcare burden of COVID-19 in the united states. pages 1–6. Publisher: Nature Publishing Group.

[130] Philip Minor. The polio endgame. 10(7):i–iii. Publisher: Taylor & Francis _eprint: https://doi.org/10.4161/21645515.2014.981115.

[131] Kenji Mizumoto, Katsushi Kagaya, Alexander Zarebski, and Gerardo Chowell. Estimating the asymptomatic proportion of coronavirus disease 2019 (COVID-19) cases on board the diamond princess cruise ship, yokohama, japan, 2020. 25(10).

[132] Leah F. Moriarty. Public health responses to COVID-19 outbreaks on cruise ships — worldwide, february–march 2020. 69.

[133] Olwen C Murphy, Kevin Messacar, Leslie Benson, Riley Bove, Jessica L Carpenter, Thomas Crawford, Janet Dean, Roberta DeBiasi, Jay Desai, Matthew J Elrick, Raquel Farias-Moeller, Grace Y Gombolay, Benjamin Greenberg, Matthew Harmelink, Sue Hong, Sarah E Hopkins, Joyce Oleszek, Catherine Otten, Cristina L Sadowsky, Teri L Schreiner, Kiran T Thakur, Keith Van Haren, Carolina M Carballo, Pin Fee Chong, Amary Fall, Vykuntaraju K Gowda, Jelte Helfferich, Ryutaro Kira, Ming Lim, Eduardo L Lopez, Elizabeth M Wells, E Ann Yeh, Carlos A Pardo, Andrea Salazar-Camelo, Divakar Mithal, Molly Wilson-Murphy, Andrea Bauer, Colyn Watkins, Mark Abzug, Samuel Dominguez, Craig Press, Michele Yang, Nusrat Ahsan, Leigh Ramos-Platt, Emmanuelle Tiongson, Mitchel Seruya, Ann Tilton, Elana Katz, Matthew Kirschen, Apurva Shah, Erlinda Ulloa, Sabrina Yum, Lileth Mondok, Megan Blaufuss, Amy Rosenfeld, Wendy Vargas, Jason Zucker, Anusha Yeshokumar, Allison Navis, Kristen Chao, Kaitlin Hagen, Michelle Melicosta, Courtney Porter, Margaret Tun-

ney, Richard Scheuermann, Priya Duggal, Andrew Pekosz, Amy Bayliss, Meghan Moore, Allan Belzberg, Melania Bembea, Caitlin O'Brien, Rebecca Riggs, Jessica Nance, Aaron Milstone, Jessica Rice, Maria A. Garcia-Dominguez, Eoin Flanagan, Jan-Mendelt Tillema, Glendaliz Bosques, Sonal Bhatia, Eliza Gordon-Lipkin, Dawn Deike, Gadi Revivo, Dan Zlotolow, Gabrielle deFiebre, Peggy Lazerow, Timothy Lotze, Ari Bitnun, Kristen Davidge, Jiri Vajsar, Amy Moore, Chamindra Konersman, Kendall Nash, Jonathan Strober, Nalin Gupta, Charles Chiu, Michael Sweeney, William Jackson, Dennis Simon, Kavita Thakkar, Jonathan Cheng, John Luce, Suman Das, Matthew Vogt, NgocHanh Vu, Jacqueline Gofshteyn, Naila Makhani, and Payal Patel. Acute flaccid myelitis: cause, diagnosis, and management. 397(10271):334–346.

[134] T. B. Woolf N. Michaud-Agrawal, E. J. Denning and O. Beckstein. *J. Comput. Chem.*, 32:2319–2327, 2011.

[135] Kangqi Ng, Beng Hoong Poon, Troy Hai Kiat Puar, Jessica Li Shan Quah, Wann Jia Loh, Yu Jun Wong, Thean Yen Tan, and Jagadesan Raghuram. COVID-19 and the risk to health care workers: A case report. Publisher: American College of Physicians.

[136] Calistus N. Ngonghala, Enahoro Iboi, Steffen Eikenberry, Matthew Scotch, Chandini Raina MacIntyre, Matthew H. Bonds, and Abba B. Gumel. Mathematical assessment of the impact of non-pharmaceutical interventions on curtailing the 2019 novel coronavirus. 325:108364.

[137] Vittoria Offeddu, Chee Fu Yung, Mabel Sheau Fong Low, and Clarence C. Tam. Effectiveness of masks and respirators against respiratory infections in healthcare workers: A systematic review and meta-analysis. 65(11):1934–1942. Publisher: Oxford Academic.

[138] Daniel P. Oran and Eric J. Topol. Prevalence of asymptomatic SARS-CoV-2 infection. Publisher: American College of Physicians.

[139] Lindsey J. Organtini, Alexander M. Makhov, James F. Conway, Susan Hafenstein, and Steven D. Carson. Kinetic and structural analysis of coxsackievirus b3 receptor interactions and formation of the a-particle. 88(10):5755–5765. Publisher: American Society for Microbiology.

[140] Daniel Owusu, Mary A Pomeroy, Nathaniel M Lewis, Ashutosh Wadhwa, Anna R Yousaf, Brett Whitaker, Elizabeth Dietrich, Aron J Hall, Victoria Chu, Natalie Thornburg, Kimberly Christensen, Tair Kiphibane, Sarah Willardson, Ryan Westergaard, Trivikram Dasu, Ian W Pray, Sanjib Bhattacharyya, Angela Dunn, Jacqueline E Tate, Hannah L Kirking, Almea Matanock, and Household Transmission Study Team. Persistent SARS-CoV-2 RNA shedding without evidence of infectiousness: A cohort study of individuals with COVID-19. 224(8):1362–1371.

[141] Thomas P. Peacock, Rebekah Penrice-Randal, Julian A. Hiscox, and Wendy S. Barclay. SARS-CoV-2 one year on: evidence for ongoing viral adaptation. 102(4).

[142] P. Plevka, R. Perera, J. Cardosa, R. J. Kuhn, and M. G. Rossmann. Structure determination of enterovirus 71. 68(9):1217–1222. Number: 9 Publisher: International Union of Crystallography.

[143] Fernando P. Polack, Stephen J. Thomas, Nicholas Kitchin, Judith Absalon, Alejandra Gurtman, Stephen Lockhart, John L. Perez, Gonzalo Pérez Marc, Edson D. Moreira, Cristiano Zerbini, Ruth Bailey, Kena A. Swanson, Satrajit Roychoudhury, Kenneth Koury, Ping Li, Warren V. Kalina, David Cooper, Robert W. Frenck, Laura L. Hammitt, Özlem Türeci, Haylene Nell, Axel Schaefer, Serhat Ünal, Dina B. Tresnan, Susan Mather, Philip R. Dormitzer, Uğur Şahin, Kathrin U. Jansen, and William C. Gruber. Safety and efficacy of the BNT162b2 mRNA covid-19 vaccine. 383(27):2603–2615. Publisher: Massachusetts Medical Society.

[144] Olha Puhach, Kenneth Adea, Nicolas Hulo, Pascale Sattonnet, Camille Genecand, Anne Iten, Frédérique Jacquérioz Bausch, Laurent Kaiser, Pauline Vetter, Isabella Eckerle, and Benjamin Meyer. Infectious viral load in unvaccinated and vaccinated individuals infected with ancestral, delta or omicron SARS-CoV-2. pages 1–1. Publisher: Nature Publishing Group.

[145] *et al.* R. J. Gowers. *Proceedings of the 15th Python in Science Conference*, pages 98–105, 2016.

[146] V. R. Racaniello. Virus-receptor interaction in poliovirus entry and pathogenesis. 87:1–16.

[147] Vincent R. Racaniello. One hundred years of poliovirus pathogenesis. 344(1):9–16.

[148] Vincent R. Racaniello and David Baltimore. Cloned poliovirus complementary dna is infectious in mammalian cells. *Science*, 214(4523):916–919, 1981.

[149] H. Rahmandad, K. Hu, R. J. Duintjer Tebbens, and K. M. Thompson. Development of an individual-based model for polioviruses: implications of the selection of network type and outcome metrics. 139(6):836–848.

[150] R. W. Pastor S. E. Feller, Y. Zhang and B. R. Brooks. *J. Chem. Phys.*, 103:4613–4621, 1993.

[151] A. B. Sabin. Properties and behavior of orally administered attenuated poliovirus vaccine. 164(11):1216–1223.

[152] Sugandha Saboo, Ebenezer Tumban, Julianne Peabody, Denis Wafula, David S. Peabody, Bryce Chackerian, and Pavan Muttil. Optimized formulation of a thermostable spray-dried virus-like particle vaccine against human papillomavirus. 13(5):1646–1655.

[153] Aki Sakurai, Toshiharu Sasaki, Shigeo Kato, Masamichi Hayashi, Sei-ichiro Tsuzuki, Takuma Ishihara, Mitsunaga Iwata, Zenichi Morise, and Yohei Doi. Natural history of asymptomatic SARS-CoV-2 infection. 0(0):null. Publisher: Massachusetts Medical Society _eprint: https://doi.org/10.1056/NEJMc2013020.

[154] J. E. Salk, J. S. Youngner, L. J. Lewis, and B. L. Bennett. Immunologic classification of poliomyelitis viruses. IV. results of typing by neutralization of prototype viruses with antiserum produced by vaccinating monkeys with unknown strain and an adjuvant. 54(2):255–267.

[155] Sjors H. W. Scheres. RELION: Implementation of a bayesian approach to cryo-EM structure determination. 180(3):519–530.

[156] Ira B. Schwartz, James Kaufman, Kun Hu, and Simone Bianco. Predicting the impact of asymptomatic transmission, non-pharmaceutical intervention and testing on the spread of COVID19.

[157] Skipper Seabold and Josef Perktold. Statsmodels: Econometric and statistical modeling with python. 2010.

[158] Mona Seifert, Pauline van Nies, Flávia S Papini, Jamie J Arnold, Minna M Poranen, Craig E Cameron, Martin Depken, and David Dulin. Temperature controlled high-throughput magnetic tweezers show striking difference in activation energies of replicating viral RNA-dependent RNA polymerases. 48(10):5591–5602.

[159] Adrian W. R. Serohijos, Zilvinas Rimas, and Eugene I. Shakhnovich. Protein biophysics explains why highly abundant proteins evolve slowly. 2(2):249–256.

[160] Kristin L. Shingler, Jennifer L. Yoder, Michael S. Carnegie, Robert E. Ashley, Alexander M. Makhov, James F. Conway, and Susan Hafenstein. The enterovirus 71 a-particle forms a gateway to allow genome release: A CryoEM study of picornavirus uncoating. 9(3):e1003240. Publisher: Public Library of Science.

[161] Yuta Shirogane, Elsa Rousseau, Jakub Voznica, Yinghong Xiao, Weiheng Su, Adam Catching, Zachary J. Whitfield, Igor M. Rouzine, Simone Bianco, and Raul Andino. Experimental and mathematical insights on the interactions between poliovirus and a defective interfering genome. 17(9):e1009277. Publisher: Public Library of Science.

[162] Sin Fun Sia, Li-Meng Yan, Alex W. H. Chin, Kevin Fung, Ka-Tim Choy, Alvina Y. L. Wong, Prathanporn Kaewpreedee, Ranawaka A. P. M. Perera, Leo L. M. Poon, John M. Nicholls, Malik Peiris, and Hui-Ling Yen. Pathogenesis and transmission of SARS-CoV-2 in golden hamsters. 583(7818):834–838. Number: 7818 Publisher: Nature Publishing Group.

[163] Petrônio C. L. Silva, Paulo V. C. Batista, Hélder S. Lima, Marcos A. Alves, Frederico G. Guimarães, and Rodrigo C. P. Silva. COVID-ABS: An agent-based model of COVID-19 epidemic to simulate health and economic effects of social distancing interventions. 139:110088.

[164] Anika Singanayagam, Seran Hakki, Jake Dunning, Kieran J Madon, Michael A Crone, Aleksandra Koycheva, Nieves Derqui-Fernandez, Jack L Barnett, Michael G Whitfield, Robert Varro, Andre Charlett, Rhia Kundu, Joe Fenn, Jessica Cutajar, Valerie Quinn, Emily Conibear, Wendy Barclay, Paul S Freemont, Graham P Taylor, Shazaad Ahmad, Maria Zambon, Neil M Ferguson, Ajit Lalvani, Anjna Badhan, Simon Dustan, Chitra Tejpal, Anjeli V Ketkar, Janakan Sam Narean, Sarah Hammett, Eimear McDermott, Timesh Pillay, Hamish Houston, Constanta Luca, Jada Samuel, Samuel Bremang, Samuel Evetts, John Poh, Charlotte Anderson, David Jackson, Shahjahan Miah, Joanna Ellis, and Angie Lackenby. Community transmission and viral load kinetics of the SARS-CoV-2 delta (b.1.617.2) variant in vaccinated and unvaccinated individuals in the UK: a prospective, longitudinal, cohort study. 22(2):183–195.

[165] Yutong Song, Oleksandr Gorbatsevych, Ying Liu, JoAnn Mugavero, Sam H. Shen, Charles B. Ward, Emmanuel Asare, Ping Jiang, Aniko V. Paul, Steffen Mueller, and

Eckard Wimmer. Limits of variation, specific infectivity, and genome packaging of massively recoded poliovirus genomes. 114(41):E8731–E8740. Publisher: Proceedings of the National Academy of Sciences.

[166] Jacqueline Staring, Eleonore von Castelmur, Vincent A. Blomen, Lisa G. van den Hengel, Markus Brockmann, Jim Baggen, Hendrik Jan Thibaut, Joppe Nieuwenhuis, Hans Janssen, Frank J. M. van Kuppeveld, Anastassis Perrakis, Jan E. Carette, and Thijn R. Brummelkamp. PLA2g16 represents a switch between entry and clearance of picornaviridae. 541(7637):412–416. Bandiera_abtest: a Cg_type: Nature Research Journals Number: 7637 Primary_atype: Research Publisher: Nature Publishing Group Subject_term: Genetic interaction;Membrane trafficking;Virus–host interactions Subject_term_id: genetic-interaction;membrane-trafficking;virus-host-interactions.

[167] Joan Stephenson. CDC tracking enterovirus d-68 outbreak causing severe respiratory illness in children in the midwest. 312(13):1290.

[168] Mike Strauss, David J. Filman, David M. Belnap, Naiqian Cheng, Roane T. Noel, and James M. Hogle. Nectin-like interactions between poliovirus and its receptor trigger conformational changes associated with cell entry. 89(8):4143–4157. Publisher: American Society for Microbiology.

[169] Thorsten Suess, Cornelius Remschmidt, Susanne B. Schink, Brunhilde Schweiger, Andreas Nitsche, Kati Schroeder, Joerg Doellinger, Jeanette Milde, Walter Haas, Irina Koehler, Gérard Krause, and Udo Buchholz. The role of facemasks and hand hygiene in the prevention of influenza transmission in households: results from a cluster randomised trial; berlin, germany, 2009-2011. 12(1):1–16. Number: 1 Publisher: BioMed Central.

[170] Yongjun Sui, Jianping Li, Roushu Zhang, Sunaina Kiran Prabhu, Hanne Andersen, David Venzon, Anthony Cook, Renita Brown, Elyse Teow, Jason Velasco, Jack

Greenhouse, Tammy Putman-Taylor, Tracey-Ann Campbell, Laurent Pessaint, Ian N. Moore, Laurel Lagenaur, Jim Talton, Matthew W. Breed, Josh Kramer, Kevin W. Bock, Mahnaz Minai, Bianca M. Nagata, Mark G. Lewis, Lai-Xi Wang, and Jay A. Berzofsky. Protection against SARS-CoV-2 infection by a mucosal vaccine in rhesus macaques. 6(10). Publisher: American Society for Clinical Investigation.

[171] Sneha Suresh, Sarah Forgie, and Joan Robinson. Non-polio enterovirus detection with acute flaccid paralysis: A systematic review. 90(1):3–7.

[172] D. York T. Darden and L. Pedersen. *J. Chem. Phys.*, 98:10089–10092, 1993.

[173] Chee Wah Tan, I-Ching Sam, Vannajan Sanghiran Lee, Hui Vern Wong, and Yoke Fun Chan. VP1 residues around the five-fold axis of enterovirus a71 mediate heparan sulfate interaction. 501:79–87.

[174] Jeffery K. Taubenberger and John C. Kash. Influenza virus evolution, host adaptation, and pandemic formation. 7(6):440–451.

[175] Kristen A. Stauffer Thompson and John Yin. Population dynamics of an RNA virus and its defective interfering particles in passage cultures. 7(1):257.

[176] Jing-Hui Tian, Nita Patel, Robert Haupt, Haixia Zhou, Stuart Weston, Holly Hammond, James Logue, Alyse D. Portnoff, James Norton, Mimi Guebre-Xabier, Bin Zhou, Kelsey Jacobson, Sonia Maciejewski, Rafia Khatoon, Malgorzata Wisniewska, Will Moffitt, Stefanie Kluepfel-Stahl, Betty Ekechukwu, James Papin, Sarathi Boddapati, C. Jason Wong, Pedro A. Piedra, Matthew B. Frieman, Michael J. Massare, Louis Fries, Karin Lövgren Bengtsson, Linda Stertman, Larry Ellingsworth, Gregory Glenn, and Gale Smith. SARS-CoV-2 spike glycoprotein vaccine candidate NVX-CoV2373 immunogenicity in baboons and protection in mice. 12(1):372. Number: 1 Publisher: Nature Publishing Group.

[177] Kelvin Kai-Wang To, Siddharth Sridhar, Kelvin Hei-Yeung Chiu, Derek Ling-Lung Hung, Xin Li, Ivan Fan-Ngai Hung, Anthony Raymond Tam, Tom Wai-Hin Chung, Jasper Fuk-Woo Chan, Anna Jian-Xia Zhang, Vincent Chi-Chung Cheng, and Kwok-Yung Yuen. Lessons learned 1 year after SARS-CoV-2 emergence leading to COVID-19 pandemic. 10(1):507–535. Publisher: Taylor & Francis _eprint: https://doi.org/10.1080/22221751.2021.1898291.

[178] Samantha M. Tracht, Sara Y. Del Valle, and James M. Hyman. Mathematical modeling of the effectiveness of facemasks in reducing the spread of novel influenza a (h1n1). 5(2):e9018. Publisher: Public Library of Science.

[179] John S. Tregoning, Katie E. Flight, Sophie L. Higham, Ziyin Wang, and Benjamin F. Pierce. Progress of the COVID-19 vaccine effort: viruses, vaccines and variants versus efficacy, effectiveness and escape. 21(10):626–636. Number: 10 Publisher: Nature Publishing Group.

[180] Simon K. Tsang, Brian M. McDermott, Vincent R. Racaniello, and James M. Hogle. Kinetic analysis of the effect of poliovirus receptor on viral uncoating: the receptor as a catalyst. 75(11):4984–4989. Publisher: American Society for Microbiology.

[181] Yueh-Liang Tsou, Yi-Wen Lin, Hsuen-Wen Chang, Hsiang-Yin Lin, Hsiao-Yun Shao, Shu-Ling Yu, Chia-Chyi Liu, Ebenezer Chitra, Charles Sia, and Yen-Hung Chow. Heat shock protein 90: Role in enterovirus 71 entry and assembly and potential target for therapy. 8(10):e77133. Publisher: Public Library of Science.

[182] François Téoulé, Cynthia Brisac, Isabelle Pelletier, Pierre-Olivier Vidalain, Sophie Jégouic, Carmen Mirabelli, Maël Bessaud, Nicolas Combelas, Arnaud Autret, Frédéric Tangy, Francis Delpeyroux, and Bruno Blondel. The golgi protein ACBD3, an interactor for poliovirus protein 3a, modulates poliovirus replication. 87(20):11031–11046. Publisher: American Society for Microbiology.

[183] M. L. Berkowitz T. Darden H. Lee U. Essmann, L. Perera and L. G. Pedersen. *J. Chem. Phys.*, 103:8577–8593, 1995.

[184] Stefan Van Der Walt, S. Chris Colbert, and Gaël Varoquaux. The NumPy array: a structure for efficient numerical computation. 13(2):22–30.

[185] H. E. Van Riper. The present status of the salk vaccine for the control of paralytic poliomyelitis. 56(14):2229–2237.

[186] Madeline Vara, Xue Wang, Jane Howe, Miaofang Chi, and Younan Xia. Understanding the stability of pt-based nanocages under thermal stress usingin situ electron microscopy. *ChemNanoMat*, 4(1):112–117, Nov 2017.

[187] I Ventoso and L Carrasco. A poliovirus 2a(pro) mutant unable to cleave 3cd shows inefficient viral protein synthesis and transactivation defects. 69(10):6280–6288. Publisher: American Society for Microbiology.

[188] Marco Vignuzzi and Carolina B. López. Defective viral genomes are key drivers of the virus–host interaction. 4(7):1075–1087. Number: 7 Publisher: Nature Publishing Group.

[189] Marco Vignuzzi, Jeffrey K. Stone, and Raul Andino. Ribavirin and lethal mutagenesis of poliovirus: molecular mechanisms, resistance and biological implications. 107(2):173–181.

[190] Pauli Virtanen, Ralf Gommers, Travis E. Oliphant, Matt Haberland, Tyler Reddy, David Cournapeau, Evgeni Burovski, Pearu Peterson, Warren Weckesser, Jonathan Bright, Stéfan J. van der Walt, Matthew Brett, Joshua Wilson, K. Jarrod Millman, Nikolay Mayorov, Andrew R. J. Nelson, Eric Jones, Robert Kern, Eric Larson, C. J. Carey, İlhan Polat, Yu Feng, Eric W. Moore, Jake VanderPlas, Denis Laxalde, Josef Perktold, Robert Cimrman, Ian Henriksen, E. A. Quintero, Charles R. Harris, Anne M.

Archibald, Antônio H. Ribeiro, Fabian Pedregosa, and Paul van Mulbregt. SciPy 1.0: fundamental algorithms for scientific computing in python. 17(3):261–272. Number: 3 Publisher: Nature Publishing Group.

[191] Merryn Voysey, Sue Ann Costa Clemens, Shabir A Madhi, Lily Y Weckx, Pedro M Folegatti, Parvinder K Aley, Brian Angus, Vicky L Baillie, Shaun L Barnabas, Qasim E Bhorat, Sagida Bibi, Carmen Briner, Paola Cicconi, Elizabeth A Clutterbuck, Andrea M Collins, Clare L Cutland, Thomas C Darton, Keertan Dheda, Christina Dold, Christopher J A Duncan, Katherine R W Emary, Katie J Ewer, Amy Flaxman, Lee Fairlie, Saul N Faust, Shuo Feng, Daniela M Ferreira, Adam Finn, Eva Galiza, Anna L Goodman, Catherine M Green, Christopher A Green, Melanie Greenland, Catherine Hill, Helen C Hill, Ian Hirsch, Alane Izu, Daniel Jenkin, Carina C D Joe, Simon Kerridge, Anthonet Koen, Gaurav Kwatra, Rajeka Lazarus, Vincenzo Libri, Patrick J Lillie, Natalie G Marchevsky, Richard P Marshall, Ana V A Mendes, Eveline P Milan, Angela M Minassian, Alastair McGregor, Yama F Mujadidi, Anusha Nana, Sherman D Padayachee, Daniel J Phillips, Ana Pittella, Emma Plested, Katrina M Pollock, Maheshi N Ramasamy, Adam J Ritchie, Hannah Robinson, Alexandre V Schwarzbold, Andrew Smith, Rinn Song, Matthew D Snape, Eduardo Sprinz, Rebecca K Sutherland, Emma C Thomson, M Estée Török, Mark Toshner, David P J Turner, Johan Vekemans, Tonya L Villafana, Thomas White, Christopher J Williams, Alexander D Douglas, Adrian V S Hill, Teresa Lambe, Sarah C Gilbert, Andrew J Pollard, Marites Aban, Kushala W. M. Abeyskera, Jeremy Aboagye, Matthew Adam, Kirsty Adams, James P. Adamson, Gbadebo Adewatan, Syed Adlou, Khatija Ahmed, Yasmeen Akhalwaya, Saajida Akhalwaya, Andrew Alcock, Aabidah Ali, Elizabeth R. Allen, Lauren Allen, Felipe B. Alvernaz, Fabio Santos Amorim, Claudia Sala Andrade, Foteini Andritsou, Rachel Anslow, Edward H. Arbe-Barnes, Mark P. Ariaans, Beatriz Arns, Laiana Arruda, Luiza Assad, Paula De Almeida Azi, Lorena De Almeida Azi, Gavin Babbage, Catherine Bailey, Kenneth F. Baker, Megan Baker, Natalie Baker, Philip Baker,

Ioana Baleanu, Danieli Bandeira, Anna Bara, Marcella A. S. Barbosa, Debbie Barker, Gavin D. Barlow, Eleanor Barnes, Andrew S. Barr, Jordan R. Barrett, Jessica Barrett, Kelly Barrett, Louise Bates, Alexander Batten, Kirsten Beadon, Emily Beales, Rebecca Beckley, Sandra Belij-Rammerstorfer, Jonathan Bell, Duncan Bellamy, Sue Belton, Adam Berg, Laura Bermejo, Eleanor Berrie, Lisa Berry, Daniella Berzenyi, Amy Beveridge, Kevin R. Bewley, Inderjeet Bharaj, Sutika Bhikha, Asad E. Bhorat, Zaheda E. Bhorat, Else Margreet Bijker, Sarah Birch, Gurpreet Birch, Kathryn Birchall, Adam Bird, Olivia Bird, Karen Bisnauthsing, Mustapha Bittaye, Luke Blackwell, Rachel Blacow, Heather Bletchly, Caitlin L. Blundell, Susannah R. Blundell, Pritesh Bodalia, Emma Bolam, Elena Boland, Daan Bormans, Nicola Borthwick, Francesca Bowring, Amy Boyd, Penny Bradley, Tanja Brenner, Alice Bridges-Webb, Phillip Brown, Claire Brown, Charlie Brown-O'Sullivan, Scott Bruce, Emily Brunt, William Budd, Yusuf A. Bulbulia, Melanie Bull, Jamie Burbage, Aileen Burn, Karen R. Buttigieg, Nicholas Byard, Ingrid Cabrera Puig, Anna Calvert, Susana Camara, Michelangelo Cao, Federica Cappuccini, Rita Cardona, João R. Cardoso, Melanie Carr, Miles W. Carroll, Andrew Carson-Stevens, Yasmin de M. Carvalho, Helen R. Casey, Paul Cashen, Thais R. Y. Castro, Lucia Carratala Castro, Katrina Cathie, Ana Cavey, José Cerbino-Neto, Luiz Fernando F. Cezar, Jim Chadwick, Chanice Chanice, David Chapman, Sue Charlton, Katerina S. Cheliotis, Irina Chelysheva, Oliver Chester, Emily Chiplin, Sunder Chita, Jee-Sun Cho, Liliana Cifuentes, Elizabeth Clark, Matthew Clark, Rachel Colin-Jones, Sarah L. K. Collins, Hayley Colton, Christopher P. Conlon, Sean Connarty, Naomi Coombes, Cushla Cooper, Rachel Cooper, Lynne Cornelissen, Tumena Corrah, Catherine A. Cosgrove, Fernanda Barroso Costa, Tony Cox, Wendy E. M. Crocker, Sarah Crosbie, Dan Cullen, Debora R. M. F. Cunha, Christina J. Cunningham, Fiona C. Cuthbertson, Daniel Marinho da Costa, Suzete N. Farias Da Guarda, Larissa P. da Silva, Antonio Carlos da Silva Moraes, Brad E. Damratoski, Zsofia Danos, Maria T. D. C. Dantas, Mehreen S. Datoo, Chandrabali Datta, Malika Davids,

Sarah L. Davies, Kelly Davies, Hannah Davies, Sophie Davies, Judith Davies, Elizabeth J. Davis, John Davis, José A. M. de Carvalho, Jeanne De Jager, Sergio de Jesus Jnr, Lis Moreno De Oliveira Kalid, David Dearlove, Tesfaye Demissie, Amisha Desai, Stefania Di Marco, Claudio Di Maso, Tanya Dinesh, Claire Docksey, Tao Dong, Francesca R. Donnellan, Tannyth Gomes Dos Santos, Thainá G. Dos Santos, Erika Pachecho Dos Santos, Naomi Douglas, Charlotte Downing, Jonathan Drake, Rachael Drake-Brockman, Ruth Drury, Joan Du Plessis, Susanna J. Dunachie, Andrew Duncan, Nicholas J. W. Easom, Mandy Edwards, Nick J. Edwards, Frances Edwards, Omar M. El Muhanna, Sean C. Elias, Branwen Ellison-Handley, Michael J. Elmore, Marcus Rex English, Alisgair Esmail, Yakub Moosa Essack, Mutjaba Farooq, Sofiya Fedosyuk, Sally Felle, Susie Ferguson, Carla Ferreira Da Silva, Samantha Field, Richard Fisher, James Fletcher, Hazel Fofie, Henry Fok, Karen J. Ford, Ross Fothergill, Jamie Fowler, Pedro H. A. Fraiman, Emma Francis, Marilia M. Franco, John Frater, Marilúcia S. M. Freire, Samantha H. Fry, Sabrina Fudge, Renato Furlan Filho, Julie Furze, Michelle Fuskova, Pablo Galian-Rubio, Harriet Garlant, Madita Gavrila, Karyna A. Gibbons, Ciaran Gilbride, Hardeep Gill, Kerry Godwin, Karishma Gokani, Maria Luisa Freire Gonçalves, Isabela G. S. Gonzalez, Jack Goodall, Jayne Goodwin, Amina Goondiwala, Katherine Gordon-Quayle, Giacomo Gorini, Alvaro Goyanna, Janet Grab, Lara Gracie, Justin Green, Nicola Greenwood, Johann Greffrath, Marisa M. Groenewald, Anishka Gunawardene, Gaurav Gupta, Mark Hackett, Bassam Hallis, Mainga Hamaluba, Elizabeth Hamilton, Joseph Hamlyn, Daniel Hammersley, Aidan T. Hanrath, Brama Hanumunthadu, Stephanie A. Harris, Clair Harris, Thomas D. Harrison, Daisy Harrison, Tara A. Harris-Wright, Thomas C. Hart, Birgit Hartnell, John Haughney, Sophia Hawkins, Laís Y. M. Hayano, Ian Head, Paul T. Heath, John Aaron Henry, Macarena Hermosin Herrera, David B. Hettle, Cristhiane Higa, Jennifer Hill, Gina Hodges, Susanne Hodgson, Elizea Horne, Mimi M. Hou, Catherine F. Houlihan, Elizabeth Howe, Nicola Howell, Jonathan Humphreys, Holly E.

Humphries, Katrina Hurley, Claire Huson, Catherine Hyams, Angela Hyder-Wright, Sabina Ikram, Alka Ishwarbhai, Poppy Iveson, Vidyashankara Iyer, Frederic Jackson, Susan Jackson, Shameem Jaumdally, Helen Jeffers, Natasha Jesudason, Carina Jones, Christopher Jones, Kathryn Jones, Elizabeth Jones, Marianna Rocha Jorge, Amar Joshi, Eduardo A. M. S. Júnior, Reshma Kailath, Faeeza Kana, Arnab Kar, Konstantinos Karampatsas, Mwila Kasanyinga, Linda Kay, Jade Keen, Johanna Kellett Wright, Elizabeth J. Kelly, Debbie Kelly, Dearbhla M. Kelly, Sarah Kelly, David Kerr, Liaquat Khan, Baktash Khozoee, Ankush Khurana, Sarah Kidd, Annabel Killen, Jasmin Kinch, Patrick Kinch, Lloyd D. W. King, Thomas B. King, Lucy Kingham, Paul Klenerman, Diana M. Kluczna, Francesca Knapper, Julian C. Knight, Daniel Knott, Stanislava Koleva, Pedro M. Lages, Matilda Lang, Gail Lang, Colin W. Larkworthy, Jessica P. J. Larwood, Rebecca Law, Alison M. Lawrie, Erica M. Lazarus, Amanda Leach, Emily A. Lees, Alice Lelliott, Nana-Marie Lemm, Alvaro Edson Ramos Lessa, Stephanie Leung, Yuanyuan Li, Amelia M. Lias, Konstantinos Liatsikos, Aline Linder, Samuel Lipworth, Shuchang Liu, Xinxue Liu, Adam Lloyd, Stephanie Lloyd, Lisa Loew, Raquel Lopez Ramon, Leandro Bonecker Lora, Kleber Giovanni Luz, Jonathan C. MacDonald, Gordon MacGregor, Meera Madhavan, David O. Mainwaring, Edson Makambwa, Rebecca Makinson, Mookho Malahleha, Ross Malamatsho, Garry Mallett, Nicola Manning, Kushal Mansatta, Takalani Maoko, Spyridoula Marinou, Emma Marlow, Gabriela N. Marques, Paula Marriott, Richard P. Marshall, Julia L. Marshall, Masebole Masenya, Mduduzi Masilela, Shauna K. Masters, Moncy Mathew, Hosea Matlebjane, Kedidimetse Matshidiso, Olga Mazur, Andrea Mazzella, Hugh McCaughan, Joanne McEwan, Joanna McGlashan, Lorna McInroy, Nicky McRobert, Steve McSwiggan, Clare Megson, Savviz Mehdipour, Wilma Meijs, Renata N. Õ. Mendonça, Alexander J. Mentzer, Ana Carolina F. Mesquita, Patricia Miralhes, Neginsadat Mirtorabi, Celia Mitton, Sibusiso Mnyakeni, Fiona Moghaddas, Kgaogelo Molapo, Mapule Moloi, Maria Moore, Marni Moran, Ella Morey, Róisín Morgans, Susan J. Morris, Sheila Morris,

Hazel Morrison, Franca Morselli, Gertraud Morshead, Richard Morter, Lynelle Mottay, Andrew Moultrie, Nathifa Moyo, Mushiya Mpelembue, Sibekezelo Msomi, Yvonne Mugodi, Ekta Mukhopadhyay, Jilly Muller, Alasdair Munro, Sarah Murphy, Philomena Mweu, Christopher Myerscough, Gurudutt Naik, Kush Naker, Eleni Nastouli, Bongani Ndlovu, Elissavet Nikolaou, Cecilia Njenga, Helena C. Noal, Andrés Noé, Gabrielle Novaes, Fay L. Nugent, Géssika Lanzillo A. Nunes, Katie O'Brien, Daniel O'Connor, Suzette Oelofse, Blanche Oguti, Victoria Olchawski, Neil J. Oldfield, Marianne G. Oliveira, Catarina Oliveira, Isabelle Silva Queiroz Oliveira, Aylin Oommen-Jose, Angela Oosthuizen, Paula O'Reilly, Peter J. O'Reilly, Piper Osborne, David R. J. Owen, Lydia Owen, Daniel Owens, Nelly Owino, Mihaela Pacurar, Brenda V. B. Paiva, Edna M. F. Palhares, Susan Palmer, Helena M. R. T. Parracho, Karen Parsons, Dipak Patel, Bhumika Patel, Faeezah Patel, Maia Patrick-Smith, Ruth O. Payne, Yanchun Peng, Elizabeth J. Penn, Anna Pennington, Marco Polo Peralta Alvarez, Bruno Pereira Pereira Stuchi, Ana Luiza Perez, Tanaraj Perinpanathan, James Perring, Rubeshan Perumal, Sahir Yusuf Petkar, Tricia Philip, Jennifer Phillips, Mary Kgomotso Phohu, Lorinda Pickup, Sonja Pieterse, Jessica Morgana Pinheiro, Jo Piper, Dimitra Pipini, Mary Plank, Sinéad Plant, Samuel Pollard, Jennifer Pooley, Anil Pooran, Ian Poulton, Claire Powers, Fernando B. Presa, David A. Price, Vivien Price, Marcelo R. Primeira, Pamela C. Proud, Samuel Provstgaard-Morys, Sophie Pueschel, David Pulido, Sheena Quaid, Ria Rabara, Kajal Radia, Durga Rajapaska, Thurkka Rajeswaran, Leonardo Ramos, Alberto San Francisco Ramos, Fernando Ramos Lopez, Tommy Rampling, Jade Rand, Helen Ratcliffe, Tom Rawlinson, David Rea, Byron Rees, Mila Resuello-Dauti, Emilia Reyes Pabon, Sarah Rhead, Tawassal Riaz, Marivic Ricamara, Alexander Richards, Alex Richter, Neil Ritchie, Adam J. Ritchie, Alexander J. Robbins, Hannah Roberts, Ryan E. Robinson, Sophie Roche, Christine Rollier, Louisa Rose, Amy L. Ross Russell, Lindie Rossouw, Simon Royal, Indra Rudiansyah, Kim Ryalls, Charlotte Sabine, Stephen Saich, Jessica C. Sale, Ahmed M. Salman, Natalia Salvador, Stephan-

nie Salvador, Milla Dias Sampaio, Annette D. Samson, Amada Sanchez-Gonzalez, Helen Sanders, Katherine Sanders, Erika Santos, Mayara F. S. Santos Guerra, Iman Satti, Jack E. Saunders, Caroline Saunders, Aakifah Bibi Arif Sayed, Ina Schim van der Loeff, Annina B. Schmid, Ella Schofield, Gavin R. Screaton, Samiullah Seddiqi, Rameswara R. Segireddy, Roberta Senger, Sonia Serrano, Imam Shaik, Hannah R. Sharpe, Katherine Sharrocks, Robert Shaw, Adam Shea, Emma Sheehan, Amy Shepherd, Farah Shiham, Sarah E. Silk, Laura Silva-Reyes, Lidiana B. T. D. Silveira, Mariana B. V. Silveira, Nisha Singh, Jaisi Sinha, Donal T. Skelly, Daniel C. Smith, Nick Smith, Holly E. Smith, David J. Smith, Catherine C. Smith, Airanuédida S. Soares, Carla Solórzano, Guilherme L. Sorio, Kim Sorley, Tiffany Sosa-Rodriguez, Cinthia M. C. D. L. Souza, Bruno S. D. F. Souza, Alessandra R. Souza, Thamyres Souza Lopez, Luciana Sowole, Alexandra J. Spencer, Louise Spoors, Lizzie Stafford, Imogen Stamford, Ricardo Stein, Lisa Stockdale, Lisa V. Stockwell, Louise H. Strickland, Arabella Stuart, Ann Sturdy, Natalina Sutton, Anna Szigeti, Abdessamad Tahiri-Alaoui, Rachel Tanner, Carol Taoushanis, Alexander W. Tarr, Richard Tarrant, Keja Taylor, Ursula Taylor, Iona Jennifer Taylor, Justin Taylor, Rebecca te Water Naude, Kate Templeton, Yrene Themistocleous, Andreas Themistocleous, Merin Thomas, Kelly Thomas, Tonia M. Thomas, Asha Thombrayil, Julia Thompson, Fawziyah Thompson, Ameeka Thompson, Amber Thompson, Kevin Thompson, Viv Thornton-Jones, Larissa H. S. Thotusi, Patrick J. Tighe, Lygia Accioly Tinoco, Gerlynn Ferreras Tiongson, Bonolo Tladinyane, Michele Tomasicchio, Adriana Tomic, Susan Tonks, James Towner, Nguyen Tran, Julia A. Tree, Gerry Trillana, Charlotte Trinham, Rose Trivett, Adam Truby, Betty Lebogang Tsheko, Philippa Tubb, Aadil Turabi, Richard Turner, Cheryl Turner, Nicola Turner, Bhavya Tyagi, Marta Ulaszewska, Benjamin R. Underwood, Samual van Eck, Rachel Varughese, Dennis Verbart, Marije K. Verheul, Iason Vichos, Taiane A. Vieira, Gemma Walker, Laura Walker, Matthew E. Wand, Theresa Wardell, George M. Warimwe, Sarah C. Warren, Bridget Watkins, Marion E. E. Wat-

174

son, Ekaterina Watson, Stewart Webb, Angela Webster, Jessica Welch, Zoe Wellbelove, Jeanette H. Wells, Alison J. West, Beth White, Caroline White, Rachel White, Paul Williams, Rachel L. Williams, Silvia Willingham, Rebecca Winslow, Danielle Woods, Mark Woodyer, Andrew T. Worth, Danny Wright, Marzena Wroblewska, Andy Yao, Yee Ting Nicole Yim, Marina Bauer Zambrano, Rafael Leal Zimmer, Dalila Zizi, and Peter Zuidewind. Single-dose administration and the influence of the timing of the booster dose on immunogenicity and efficacy of ChAdOx1 nCoV-19 (AZD1222) vaccine: a pooled analysis of four randomised trials. 397(10277):881–891.

[192] Philip V'kovski, Annika Kratzel, Silvio Steiner, Hanspeter Stalder, and Volker Thiel. Coronavirus biology and replication: implications for SARS-CoV-2. 19(3):155–170. Number: 3 Publisher: Nature Publishing Group.

[193] J. D. Madura R. W. Impey W. L. Jorgensen, J. Chandrasekhar and M. L. Klein. *J. Chem. Phys.*, 79:926, 1983.

[194] Rahnuma Wahid, Laina Mercer, Andrew Macadam, Sarah Carlyle, Laura Stephens, Javier Martin, Konstantin Chumakov, Majid Laassri, Svetlana Petrovskaya, Saskia L. Smits, Koert J. Stittelaar, Chris Gast, William C. Weldon, Jennifer L. Konopka-Anstadt, M. Steven Oberste, Pierre Van Damme, Ilse De Coster, Ricardo Rüttimann, Ananda Bandyopadhyay, and John Konz. Assessment of genetic changes and neurovirulence of shed sabin and novel type 2 oral polio vaccine viruses. 6(1):1–11. Number: 1 Publisher: Nature Publishing Group.

[195] Thomas S. Walter, Jingshan Ren, Tobias J. Tuthill, David J. Rowlands, David I. Stuart, and Elizabeth E. Fry. A plate-based high-throughput assay for virus stability and vaccine formulation. 185(1):166–170.

[196] Jing Wang, Jennifer B. Ptacek, Karla Kirkegaard, and Esther Bullitt. Double-membraned liposomes sculpted by poliovirus 3ab protein*. 288(38):27287–27298.

[197] Shih-Min Wang, Ching-Chuan Liu, Hui-Wan Tseng, Jen-Ren Wang, Chao-Ching Huang, Yung-Jung Chen, Yao-Jong Yang, Shio-Jean Lin, and Tsu-Fuh Yeh. Clinical spectrum of enterovirus 71 infection in children in southern taiwan, with an emphasis on neurological complications. 29(1):184–190.

[198] Xiangxi Wang, Wei Peng, Jingshan Ren, Zhongyu Hu, Jiwei Xu, Zhiyong Lou, Xumei Li, Weidong Yin, Xinliang Shen, Claudine Porta, Thomas S. Walter, Gwyndaf Evans, Danny Axford, Robin Owen, David J. Rowlands, Junzhi Wang, David I. Stuart, Elizabeth E. Fry, and Zihe Rao. A sensor-adaptor mechanism for enterovirus uncoating from structures of EV71. 19(4):424–429. Bandiera_abtest: a Cg_type: Nature Research Journals Number: 4 Primary_atype: Research Publisher: Nature Publishing Group Subject_term: Structural biology;Viral infection;Virus structures Subject_term_id: structural-biology;viral-infection;virus-structures.

[199] Xiaoli Wang, Zhiqiang Ku, Xiang Zhang, Xiaohua Ye, Jinhuan Chen, Qingwei Liu, Wei Zhang, Chao Zhang, Zhenglin Fu, Xia Jin, Yao Cong, and Zhong Huang. Structure, immunogenicity, and protective mechanism of an engineered enterovirus 71-like particle vaccine mimicking 80s empty capsid. 92(1):e01330–17. Publisher: American Society for Microbiology.

[200] Mary K. Weidman, Padmaja Yalamanchili, Bryant Ng, Weimin Tsai, and Asim Dasgupta. Poliovirus 3c protease-mediated degradation of transcriptional activator p53 requires a cellular activity. 291(2):260–271.

[201] Yiska Weisblum, Fabian Schmidt, Fengwen Zhang, Justin DaSilva, Daniel Poston, Julio Cc Lorenzi, Frauke Muecksch, Magdalena Rutkowska, Hans-Heinrich Hoffmann, Eleftherios Michailidis, Christian Gaebler, Marianna Agudelo, Alice Cho, Zijun Wang, Anna Gazumyan, Melissa Cipolla, Larry Luchsinger, Christopher D. Hillyer, Marina Caskey, Davide F. Robbiani, Charles M. Rice, Michel C. Nussenzweig, Theodora Hatzi-

ioannou, and Paul D. Bieniasz. Escape from neutralizing antibodies by SARS-CoV-2 spike protein variants. 9:e61312.

[202] Alexandra I Wells and Carolyn B Coyne. Enteroviruses: A gut-wrenching game of entry, detection, and evasion. *Viruses*, 11(5), May 2019.

[203] Klaus Wetz. Attachment of neutralizing antibodies stabilizes the capsid of poliovirus against uncoating. 192(2):465–472.

[204] Zachary J. Whitfield, Abhishek N. Prasad, Adam J. Ronk, Ivan V. Kuzmin, Philipp A. Ilinykh, Raul Andino, and Alexander Bukreyev. Species-specific evolution of ebola virus during replication in human and bat cells. 32(7):108028.

[205] Michael R. Wilson. Emerging viral infections. 26(3):301–306.

[206] Mark E. J. Woolhouse, Liam Brierley, Chris McCaffery, and Sam Lycett. Assessing the epidemic potential of RNA and DNA viruses - volume 22, number 12—december 2016 - emerging infectious diseases journal - CDC.

[207] Roman Wölfel, Victor M. Corman, Wolfgang Guggemos, Michael Seilmaier, Sabine Zange, Marcel A. Müller, Daniela Niemeyer, Terry C. Jones, Patrick Vollmar, Camilla Rothe, Michael Hoelscher, Tobias Bleicker, Sebastian Brünink, Julia Schneider, Rosina Ehmann, Katrin Zwirglmaier, Christian Drosten, and Clemens Wendtner. Virological assessment of hospitalized patients with COVID-2019. 581(7809):465–469. Number: 7809 Publisher: Nature Publishing Group.

[208] Yinghong Xiao, Peter V. Lidsky, Yuta Shirogane, Ranen Aviner, Chien-Ting Wu, Weiyi Li, Weihao Zheng, Dale Talbot, Adam Catching, Gilad Doitsh, Weiheng Su, Colby E. Gekko, Arabinda Nayak, Joel D. Ernst, Leonid Brodsky, Elia Brodsky, Elsa Rousseau, Sara Capponi, Simone Bianco, Robert Nakamura, Peter K. Jackson, Judith Frydman, and Raul Andino. A defective viral genome strategy elicits broad protective immunity against respiratory viruses. 184(25):6037–6051.e14. Publisher: Elsevier.

[209] Chen Xu, Yinqiao Dong, Xiaoyue Yu, Huwen Wang, Lhakpa Tsamlag, Shuxian Zhang, Ruijie Chang, Zezhou Wang, Yuelin Yu, Rusi Long, Ying Wang, Gang Xu, Tian Shen, Suping Wang, Xinxin Zhang, Hui Wang, and Yong Cai. Estimation of reproduction numbers of COVID-19 in typical countries and epidemic trends under different prevention and control scenarios.

[210] Longfa Xu, Qingbing Zheng, Rui Zhu, Zhichao Yin, Hai Yu, Yu Lin, Yuanyuan Wu, Maozhou He, Yang Huang, Yichao Jiang, Hui Sun, Zhenghui Zha, Hongwei Yang, Qiongzi Huang, Dongqing Zhang, Zhenqin Chen, Xiangzhong Ye, Jinle Han, Lisheng Yang, Che Liu, Yuqiong Que, Mujin Fang, Ying Gu, Jun Zhang, Wenxin Luo, Z. Hong Zhou, Shaowei Li, Tong Cheng, and Ningshao Xia. Cryo-EM structures reveal the molecular basis of receptor-initiated coxsackievirus uncoating. 29(3):448–462.e5.

[211] Seiya Yamayoshi, Seii Ohka, Ken Fujii, and Satoshi Koike. Functional comparison of SCARB2 and PSGL1 as receptors for enterovirus 71. 87(6):3335–3347. Publisher: American Society for Microbiology.

[212] Ming Te Yeh, Erika Bujaki, Patrick T. Dolan, Matthew Smith, Rahnuma Wahid, John Konz, Amy J. Weiner, Ananda S. Bandyopadhyay, Pierre Van Damme, Ilse De Coster, Hilde Revets, Andrew Macadam, and Raul Andino. Engineering the live-attenuated polio vaccine to prevent reversion to virulence. 27(5):736–751.e8.

[213] Ming-Te Yeh, Shainn-Wei Wang, Chun-Keung Yu, Kuei-Hsiang Lin, Huan-Yao Lei, Ih-Jen Su, and Jen-Ren Wang. A single nucleotide in stem loop II of 5'-untranslated region contributes to virulence of enterovirus 71 in mice. 6(11):e27082. Publisher: Public Library of Science.

[214] F. H. Yin. Involvement of viral procapsid in the RNA synthesis and maturation of poliovirus. 82(2):299–307.

[215] Cyril C. Y. Yip, Susanna K. P. Lau, Patrick C. Y. Woo, and Kwok-Yung Yuen. Human enterovirus 71 epidemics: what's next? 6(1):19780. Publisher: Taylor & Francis _eprint: https://doi.org/10.3402/ehtj.v6i0.19780.

[216] Ji-Won Yoon and Abner Louis Notkins. Virus-induced diabetes in mice. 32(7):37–40.

[217] Shilin Yuan, Guiming Li, Ying Wang, Qianqian Gao, Yizhuo Wang, Rui Cui, Ralf Altmeyer, and Gang Zou. Identification of positively charged residues in enterovirus 71 capsid protein VP1 essential for production of infectious particles. 90(2):741–752. Publisher: American Society for Microbiology.

[218] Juanjuan Zhang, Maria Litvinova, Wei Wang, Yan Wang, Xiaowei Deng, Xinghui Chen, Mei Li, Wen Zheng, Lan Yi, Xinhua Chen, Qianhui Wu, Yuxia Liang, Xiling Wang, Juan Yang, Kaiyuan Sun, Ira M. Longini, M. Elizabeth Halloran, Peng Wu, Benjamin J. Cowling, Stefano Merler, Cecile Viboud, Alessandro Vespignani, Marco Ajelli, and Hongjie Yu. Evolving epidemiology and transmission dynamics of coronavirus disease 2019 outside hubei province, china: a descriptive and modelling study. 20(7):793–802.

[219] Daming Zhou, Yuguang Zhao, Abhay Kotecha, Elizabeth E. Fry, James T. Kelly, Xiangxi Wang, Zihe Rao, David J. Rowlands, Jingshan Ren, and David I. Stuart. Unexpected mode of engagement between enterovirus 71 and its receptor SCARB2. 4(3):414–419. Number: 3 Publisher: Nature Publishing Group.

Publishing Agreement

It is the policy of the University to encourage open access and broad distribution of all theses, dissertations, and manuscripts. The Graduate Division will facilitate the distribution of UCSF theses, dissertations, and manuscripts to the UCSF Library for open access and distribution. UCSF will make such theses, dissertations, and manuscripts accessible to the public and will take reasonable steps to preserve these works in perpetuity.

I hereby grant the non-exclusive, perpetual right to The Regents of the University of California to reproduce, publicly display, distribute, preserve, and publish copies of my thesis, dissertation, or manuscript in any form or media, now existing or later derived, including access online for teaching, research, and public service purposes.

Author Signature

5/25/2022

Date